NMR STUDY OF WATER IN NANOSCOPIC CONFINEMENT AND AT THE INTERFACE OF BIOMOLECULES

Haijing Wang

A dissertation submitted to the faculty of the University of North Carolina at Chapel Hill in partial fulfillment of the requirements for the degree of Doctor of Philosophy in the Department of Physics and Astronomy.

Chapel Hill
2011

Approved by
Dr. Yue Wu, Advisor
Dr. Alfred Kleinhammes, Reader
Dr. Laurie E. McNeil, Reader
Dr. Edward T. Samulski, Reader
Dr. Sean Washburn, Reader

ABSTRACT

HAIJING WANG: NMR Study of Water in Nanoscopic Confinement and at the Interface of Biomolecules
(Under the direction of Prof. Yue Wu)

Water in nanoscopic confinement and at the interface of biomolecules plays critical roles in a wide range of biological processes including protein dynamics and functions. For the nanoconfined water, I report a hydrophobic-hydrophilic transition upon cooling from 22°C to 8°C via the observation of water adsorption isotherms in SWNTs measured by NMR. A considerable slowdown in molecular reorientation of such adsorbed water was also detected. Nanoconfined water in slit-shaped wettable pores has a spin-lattice relaxation time similar to that observed in bulk water, suggesting a similar molecular reorientation in both conditions. The dependence of the capillary condensation pressure on the nanoscopic pore size resembles that given by the Kelvin equation, despite the equation's questionable validity on nanoscale. For water at the interfaces of proteins, the most basic property of protein hydration—the water sorption isotherm—remains inadequately understood. Using NMR to measure the isotherms of lysozyme *in situ* between 18 and 2°C, the present work provides evidence that the part of water uptake above the hydration level at which protein starts to function is significantly reduced below 8°C. Quantitative analysis shows that such reduction is directly related to the reduction of protein flexibility and enhanced cost in elastic energy for accommodating the hydration water at lower temperature. The elastic property derived from the water isotherm agrees with direct mechanical measurements, providing independent support for the solution model, in which protein is treated as a polymer-like solute. The

hemoglobin hydration shows similar temperature dependence to that observed in lysozyme. NMR relaxation with paramagnetic centers that are present in those proteins could reveal the dynamics of hydration water within the protein. The role of interfacial water in the action of general anesthesia remains a topic of controversy. Using ^{1}H and ^{19}F NMR, I provide direct experimental evidence that interfacial water in the proximity to proteins is essential for the molecular interaction between anesthetics and proteins. The halothane adsorption isotherms can reveal the molecular nature of general anesthesia.

TO YANJUAN ZOU

ACKNOWLEDGEMENTS

The works discussed in this dissertation were made possible with the support of the National Science Foundation (DMR-0513915 and DMR-0906547) and the National Institute of Health (R37GM049202).

I want to express my sincere gratitude to my advisor, Prof. Yue Wu, for giving me the opportunity to meet him, to learn from him, and to work for him. I can still remember every words of our first conversation on August 14, 2006. At that moment, it was impossible for me to imagine how important a role he would play as the mentor of my life. During the past five years, he has taught me, hand by hand and step by step, how to do experiments, how to analyze and present results, how to write a manuscript, how to choose books to read, how to think creatively and deeply, and even how to be a better person. His influence on me was far beyond the academic training. It is his encouragements and guidance that led me through graduate study and shaped me to who I am today.

It would not have been possible to complete this dissertation without the training and help from Dr. Alfred Kleinhammes. His expertise in NMR saved me many times from the miserable moments when the hardware failed. I truly benefit from his training on how to handle new techniques and old equipment.

I feel very lucky to sit and work near the desk of Dr. Horst Kessemeier, a pioneer of NMR. It was a great surprise to me, during my first year here, when I found several works by Horst, a person I actually knew, were cited many times in a standard textbook of NMR. Even

now I am still intrigued by his findings from many years ago. I am also grateful to Horst because the majority part of my dissertation research was performed on his magnet and NMR probe.

I'd like to express my special gratitude to Dr. Pabitra Sen for his encouragements and discussions and for introducing me to a different type of research environment.

To all my advisors and mentors, please allow me to use the old Chinese saying to express my gratitude in a traditional way. "Even if someone is your teacher for only a day, you should regard him like your father for the rest of your life."

I am also very thankful to previous and current members of Wu Group for their help. These members are: Drs. Xuekui Xi, Qiang 'Charles' Chen, Shenghua Mao, Yuanyuan Jia, Harsha Kulkarni, Gregory Mogilevsky, B. J. Anderson, and Cassi Galt, Shaun Gidcumb, Jacob Forstater, Magdalena Sandor, Courtney Hadsell, Zhixiang Luo, Yunzhao Xing. I want to thank B. J. Anderson and Jacob Forstater for the initial proof reading of this dissertation, and Shaun Gidcumb for the many suggestions on my presentation.

I also want to thank Drs. William Mullins, Shubin Liu, Yan Xu and Pei Tang, for their training in and discussion of computer simulations. I am also grateful to Drs. Yi-Qiao Song, Ridvan Akkurt, Martin Hürlimann, Lukasz Zielinski, Ravinath Viswanathan, Jeffrey Paulsen, and Andre Souza, Xiang Xu, Stephen Hobson, for their hospitality and help during my internship.

I want to thank Prof. Warren S. Warren from Duke University and Prof. Keith Gubbins from NCSU for allowing me take their classes during my graduate study. The knowledge and techniques I learned from their classes are extremely helpful for my research.

I am grateful to my committee members, Profs. Yue Wu, Alfred Kleinhammes, Laurie E. McNeil, Edward Samulski, and Sean Washburn, for reading and offering helpful suggestions on my dissertation. Prof. Keith E. Gubbins gave me advices and critiques throughout my graduate study until the final oral defense, which he is unable to attend due to scheduling conflict. Prof. McNeil's critiques and corrections throughout the entire dissertation are greatly appreciated.

Thanks also go to friends I've been fortunate to meet over the course of graduate study: Liang He, Wei Luo, Zhaokang Hu, Letian Lin, Rudresh Ghosh, Adam Kelleher, Nathan Hudson, Zhongqiao Ren, Rui Peng, Yingchi Liu, Taoran Cui and many others.

I also very much appreciate the support of my parents. I dedicated this dissertation to my beloved wife, Yanjuan Zou.

TABLE OF CONTENTS

LIST OF TABLES xiii

LIST OF FIGURES xiv

LIST OF ABBREVIATIONS xviii

CHAPTER 1 INTRODUCTION 1

1.1 Water: Matrix of Life 1

1.1.1 Bulk water 1

1.1.2 Nanoconfined and interfacial water 3

1.1.3 Dissertation outlines 5

1.2 Adsorption 6

1.2.1 Basic quantities 7

1.2.2 Langmuir isotherm 8

1.2.3 Multimolecular adsorption and Brunauer-Emmett-Teller isotherm 9

1.2.4 Classification of isotherms 10

1.2.5 Uniqueness of water adsorption 11

1.3 Nuclear Magnetic Resonance 12

1.3.1 Magnetization 13

1.3.2 Interactions 14

1.3.3 Relaxation 15

1.4 Experimental Setup 17

1.5 References 20

CHAPTER 2 TEMPERATURE-INDUCED HYDROPHOBIC-HYDROPHILIC TRANSITION OBSERVED BY WATER ADSORPTION 22

2.1 Introduction 22

2.2 Experiments 23

2.3 Results and Discussion 26

2.3.1 Water adsorption isotherms in SWNTs 26

2.3.2 Dubinin-Radushkevitch-Kaganer equation 27

2.3.3 Local excess chemical potential 28

2.3.4 NMR relaxation and molecular reorientation 29

2.4 Conclusion 31

2.5 Acknowledgements 32

2.6 References 33

CHAPTER 3 BULK-LIKE PROPERTIES OF WATER IN NANOSCOPIC CONFINEMENT 35

3.1 Introduction 35

3.2 Experiments 38

3.3 Results and Discussion 39

3.3.1 Binary adsorption isotherms of H_2 and D_2O 39

3.3.2 Water adsorption in activated carbons 41

3.3.3 Mahle's isotherm 42

3.3.4 Pore size distribution 43

3.4 Conclusion 46

3.5 References 48

CHAPTER 4 TEMPERATURE DEPENDENCE OF LYSOZYME HYDRATION AND THE ROLE OF ELASTIC ENERGY 50

4.1 Introduction 50

4.2 Experiments 53

4.3 Results and Discussion 55

4.3.1 Surface adsorption picture 57

4.3.2 Modified Flory-Huggins theory 58

4.3.3 The elastic constant and its temperature dependence 60

4.3.4 Protein properties with hydration above $h = 0.2$ 63

4.3.5 The nature of the upswing in water uptake 63

4.3.6 Molecular dynamics simulations 64

4.4 Conclusion 67

4.5 Acknowledgements 68

4.6 References 71

CHAPTER 5 TEMPERATURE DEPENDENCE OF HEMOGLOBIN HYDRATION AND THE DYNAMICS OF HYDRATION WATER 73

5.1 Introduction 73

5.2 Experiments 76

5.3 Results and Discussion 77

5.3.1 Water sorption isotherms and elastic modulus 77

5.3.2 Line broadening and the diffusion barrier 80

5.3.3 Spin-lattice relaxation of proteins 83

5.3.4 Spin-lattice relaxation of hydration water 86

5.4 Conclusion 88

5.5 References 89

CHAPTER 6 ROLE OF INTERFACIAL WATER IN MEDIATING THE INTERACTION BETWEEN HALOTHANE AND PROTEINS 91

6.1 Introduction 91

6.2 Experiments 99

6.3 Results and discussion 101

6.4 Conclusion 103

6.5 References 104

CHAPTER 7 CONCLUSION 106

LIST OF TABLES

Table 1.1 Gyromagnetic ratio of nuclei used in NMR and electron used in EPR. 13

Table 3.1 Parameters characterizing three activated carbons derived from PEEK**.** *A*, *B*, and n_s/D are used to fit the water adsorption isotherms to Eq. (3.1). The pore size and BET surface area are determined in ref [16, 17]. 43

Table 4.1 Fitting parameters (χ and *K*) and standard errors following Eq. (2), when η=1, 0.5 and 0.25, and the maximum number of water per protein associated with the elastic free energy $N^0_{(el)}$, and the total number of hydration water per protein $N^0_{hydration}$, at P/P_0=1. 62

LIST OF FIGURES

Figure 1.1 A four-coordinated water molecule showing the classic tetrahedral arrangement of the first-neighbor environment of a water molecule hydrogen-binding to four neighbors. The hydrogen atom attached to a relatively electronegative atom is a hydrogen bond donor. The electronegative atom, such as the oxygen atom, is a hydrogen bond acceptor. Based on the transfer of electron density, the central molecule 'donates' two hydrogen bonds to its two lower neighbors and 'accepts' a hydrogen bond from each of its two upper neighbors [6]..... 2

Figure 1.2 The phase diagram of ice [6]. 3

Figure 1.3 How water behaves at different hydrophobic elements: extended surfaces, biomolecules, and SWNTs [29]. 5

Figure 1.4 Illustration of water adsorption in SWNTs, in microporous activated carbons derived from PEEK, and on the surface of biomolecules. 6

Figure 1.5 The IUPAC classification of adsorption isotherms for gas-solid equilibria [33]..... 11

Figure 1.6 *In situ* water loading system for NMR spectrometer at 34 MHz. 18

Figure 1.7 *In situ* gas and vapor loading system for NMR spectrometer at 300 MHz. 19

Figure 2.1 The TEM image of SWNTs. It shows that the samples in the current experiment are relatively long (>1μm) and devoid of magnetic particles. 24

Figure 2.2 ^{1}H NMR spectrum of ethane adsorbed in SWNTs. The spectrum is taken at 108 kPa and at room temperature. The dashed lines are Lorentzian fits. The sharp peak (blue) and the broad peak (red) are assigned to the ethane outside and inside the SWNTs, respectively. This shows that the SWCNTs are open for adsorption..... 25

Figure 2.3 Water adsorption isotherms in SWNTs. (A) Three isotherms at 8.0°C (squares), 18.4°C (triangles), and 22.1°C (circles) are shown (The uncertainty of T is ±0.3°C). The lines are guides to the eye. The vertical error bars are shown when they are larger than the size of the symbols and the pressure uncertainty is less than 1% of P_0. (B) An illustration of monolayer water in SWNTs with a diameter of 1.36 nm. Monolayer adsorption forms a tube-like structure at 8.0°C under the constraint of the SWNTs. (C) A logarithmic plot of water content versus $[\log_{10}(P_0/P)]^2$ for the isotherm at 8.0°C, following the Dubbin-Radushkevitch-Kaganer equation. 27

Figure 2.4 Relaxation time of confined water. The measured T_1 (A) and T_2 (B) values versus relative pressure at 8.0°C (squares) and 18.4°C (triangles) are shown. The theoretical values of T_1 and T_2 based on the intramolecular dipolar interaction are shown in (C). Based on the measured T_1 values at P/P_0=0.75, 7 ms at 18.4°C and 3 ms at 8.0°C, the corresponding correlation times of 132 and 46 ns, respectively, are

identified. The corresponding T_2 values are shorter than the theoretically expected values for reasons explained in the text. The correlation times at these two temperatures become the same at P/P_0=1 (26 ns). 31

Figure 3.1 Illustrations of (a) capillary phenomena at macroscopic scale and (b) capillary condensation at microscopic scale. 37

Figure 3.2 Water adsorption isotherms in three microporous activated carbons derived from PEEK with different amount of burn-offs at room temperature. Isotherms are fitted to Eq. (3.1), with fitting parameters shown in Table I. The inset shows the water spin-lattice relaxation time at different relative pressure. 38

Figure 3.3 (a) ^{1}H NMR spectra of H_2 at the pressure of 100 atm with different amounts of preadsorbed D_2O in the sample with 35 wt% burn-off. (b) The binary isotherms with H2 and D_2O based on the peak intensity of upfield peak in H_2 spectra. Water adsorption in the same sample is duplicated on the plane of H_2 pressure of 100 atm. 40

Figure 3.4 Pore size distribution determined from water adsorption isotherms and from the differential pore volume determined from N_2 adsorption at 77k in Ref [17]. The data are converted from the isotherms shown in Figure 3.2. The dashed lines are fitted to Eq. (3.2). The inset shows the correlation of pore size d with the condensation pressure characterized by A. The data obtained from three samples give a straight line. 47

Figure 4.1 (a) A van der Waals representation of a lysozyme molecule colored with a hydrophobic scale: white = hydrophobic, red (dark gray) = hydrophilic, orange (gray) = positive or negative charge. (b) A lattice model of protein hydration. The white chain represents a lysozyme molecule occupying x lattice cells. The blue (gray) spheres are hydration water, each of which occupies one lattice cell. Their locations are obtained from hydration water of less than 0.34 nm away from the protein in molecular dynamics simulations shown in Section 4.3.6. 51

Figure 4.2 (a) NMR spectra of lysozyme powder before (open circle) and after pumping (filled circle). (b) The sharp NMR peak corresponding to the hydration water of protein as the temperature decreases from 4°C to -34°C. The initial hydration level is h~0.21 at 4°C. The inset shows the hydration levels estimated from the integrated intensities of such sharp peaks. 55

Figure 4.3 Water sorption isotherms in lysozyme powder from 18°C to 2°C. The isotherms at high relative pressure are fitted as the implicit form of Eq. (4.2) with parameters shown in Table 4.1. The inset plots $N_{(el)}^0$ versus temperature. 56

Figure 4.4 Plots of $[\ln(P/P_0)-\ln v_1-v_2]/v_2^2$ versus $[(v_2^{-1/3}-1)(5/3v_2^{-1/3}-1)/v_2^2]$ for the isotherms data following Eq. (4.2). The plots show a linear portion when $[\ln(P/P_0)-\ln v_1-v_2]/v_2^2>0.6$. The fitting parameters are shown in Table 4.1 for η=1. The inset shows the comparison of the temperature dependence of the elastic modulus (red square) derived from isotherms in this study, with the Young's modulus of hydrated lysozyme (red circle) measured in [31]. 60

Figure 4.5 A ribbon representation of lysozyme structure from an averaged structure from the last 5 ns of 11 ns *NPT* simulations at 18°C and $P/P_0 = 1$. The residues with elevated fluctuations and correlated motions by hydration water are highlighted in red (dark gray, residues 44-53) and in yellow (light gray, residues 59-81). The residues with low fluctuations in the β-domain are shown in orange (gray, residues 54-58). Residues that are essential for the completion of the enzymatic reaction (Glu35 and Asp52) are shown in an atomic representation. The rest of the residues are shown in a narrow ribbon representation. 69

Figure 4.6 All-mode correlation plots of hen egg white lysozyme from normal mode analysis using the Gaussian network model. The *NPT* simulations are under comparable conditions to the experiments at relative vapor pressure of P/P_0=0.6 ($N_{hydration}$ =124) (a) and P/P_0=1 ($N_{hydration}$ =360) (b), and the temperature of 18°C. Averaged structures from the last 5 ns of 11-ns MD simulations were used for the GNM analyses. Cross correlation of motion is color-coded using the color (gray) scale to the right. The most profound increases in diagonal intensities are from residues 44-53 (upper-left dashed squares and the red region in Figure 4.5) and residues 59-81 (lower-right dashed squares and the yellow region in Figure 4.5). The corresponding increases in off-diagonal intensities between these two residue groups are labeled by rectangles. 70

Figure 5.1 (a) Structure of the heme group with an iron in the center. (b) Secondary structures and oxygen binding sites of hemoglobin (PDB: 1GZX) in a ribbon representation. The heme groups are highlighted with a CPK representation. 74

Figure 5.2 Different oxidization states of hemoglobin. 75

Figure 5.3 Temperature-dependent water sorption isotherms in hemoglobin. The dashed lines are fitted to D'Arcy-Watt isotherms at low relative pressure region. At high relative pressure, the isotherm is fitted into the implicit form of Rowen-Simha equation [16]. 78

Figure 5.4 Plots of $[\ln(P/P_0)-0.5\ln v_1-0.5v_2]/v_2^2$ versus $[(v_2^{-1/3}-1)(5/3v_2^{-1/3}-1)/v_2^2]$ for the isotherms data following the Rowen-Simha equation [16]..... 79

Figure 5.5 The spin-spin relaxation time for hemoglobin and its hydration water..... 81

Figure 5.6 The number of protons within a radius from the relaxation centers based on the structure of hemoglobin (1GZX). 83

Figure 5.7 The value of long and short components of the spin-lattice relaxation time of proteins..... 86

Figure 5.8 The value of long and short components of the spin-lattice relaxation time of water..... 87

Figure 6.1 The Meyer-Overton correlation for anesthetics. 92

Figure 6.2 Structure of general anesthetics widely used in medicine [7]. 92

Figure 6.3 A diagram showing the logarithm of the anesthetizing partial pressure of non-hydrogen-bonding anesthetic agents plotted against the equilibrium partial pressure of their hydrate crystals [18]..... 94

Figure 6.4 The structure of the hydrate crystals of small molecules, such as xenon..... 95

Figure 6.5 Gas chromatographic partition analysis of isoflurane equilibrium binding to BSA at 22°C, pH 7.2, and a concentration of 28 mg/mL. 96

Figure 6.6 Most voltage-gated ion channels are relatively insensitive to general anesthetics. general anesthesia in humans (●), as measured by the lack of a purposeful response to a surgical incision, occurs at concentrations of halothane 4 to 30 times lower than the EC_{50} concentrations needed to half-inhibit peak currents through L-type Ca^{2+} channels (○) from clonal pituitary cells, Na^{+} channels (□) from the squid giant axon, or delayed rectifier K^{+} channels (Δ) from the squid giant axon [5]. 97

Figure 6.7 (a) Identity of general anesthetic concentrations needed to anesthetize whole animals and to inhibit luciferase activity by 50%, for a diverse range of simple anesthetics over a 100,000-fold range of potencies. The line is the line of identity [24]. (b) Clinically relevant concentrations of halothane potentiate responses to low levels of GABA (3 μM) in dissociated rat brain neurons, with 50% potentiation occurring at 0.23 mM halothane, close to the EC_{50} for general anesthesia (arrow) [5]..... 98

Figure 6.8 ^{19}F NMR spectra of halothane in an empty NMR tube, in dry lysozyme and BSA. 99

Figure 6.9 Adsorption isotherms of methane (117.2 K), n-butane (0.0°C), neopentane (10.0°C) and SF_6 (-64°C) in egg albumin (2% spray frozen) shown in order of low to high curve [25]..... 100

Figure 6.10 ^{19}F NMR spectra of halothane in wet lysozyme..... 101

Figure 6.11 ^{19}F NMR spectra of halothane in wet BSA. 102

LIST OF ABBREVIATIONS

NMR	Nuclear Magnetic Resonance
SWNTs	Single Wall Nanotubes
TGA	Thermogravimetric Analyzer
PEEK	Polyether Ether Ketone
BET	Brunauer, Emmett, and Teller
IUPAC	International Union of Pure and Applied Chemistry
EPR	Electron Paramagnetic Resonance
PAS	Primary Adsorption Sites
TEM	Transmission Electron Microscope
VWD	van der Waals
BO	Burn Off
DFT	Density Function Theory
HEWL	Hen Egg White Lysozyme
BSA	Bovine Serum Albumin
MD	Molecular Dynamics
PDB	Protein Data Bank
GNM	Gaussian Network Model
RF	Radio Frequency
FID	Free Induction Decay
MAC	Minimum Alveolar Concentration
FWHM	Full Width at Half Maximum

CHAPTER 1

INTRODUCTION

1.1 Water: Matrix of Life

1.1.1 Bulk water

Water is the most abundant compound on Earth's surface and the principal constituent of all living organisms [1, 2]. It is the most essential solvent to biological processes and thus often called the "molecule of life" or "matrix of life" [3, 4]. Water is also one of the most mysterious chemical compounds, known for its anomalies such as shrinking on melting [5, 6]. The water molecule consists of an oxygen atom and two hydrogen atoms, with an average O-H bond length of 0.9572 Å and H-O-H bond angle of 104.52° [1]. Water molecules interact with each other through hydrogen bonding with a strength of 20 kJ/mol [7]. The directionality of the hydrogen bond and the maximum number of neighbors a water molecule can interact with determine most of the structural and thermodynamical properties of water.

Figure 1.1 shows the four-coordinated water structure motif connected through hydrogen bonds [6]. Based on this motif and a variation in both the hydrogen bond length and the OOO bond angles, solid water may assume a variety of structures known as about 16 crystalline phases and three amorphous phases of ice [5]. Figure 1.2 shows the phase diagram of ice [6]. Most of the anomalous behaviors of liquid water are related to the four-

coordinated local geometry. For instance, liquid water contains a range of ring structures including five- and fourfold ones, which are less space demanding than the sixfold ring in ice Ih as shown in Figure 1.2. The removal of the crystal constraints allows the molecules to assume a large variety of local structures, many of which occupy less volume than the crystal. As temperature increases, the hydrogen bond length increases and the variation of OOO angles also increases. This allows water to explore a denser packing than ice. From 273 K to 277 K, the increase in the OOO angle variation dominates the volume change, leading to a contraction of water volume. As temperature increases above 277 K, the normal thermal expansion mechanism takes over as the increase of hydrogen bond length dominates the volume change.

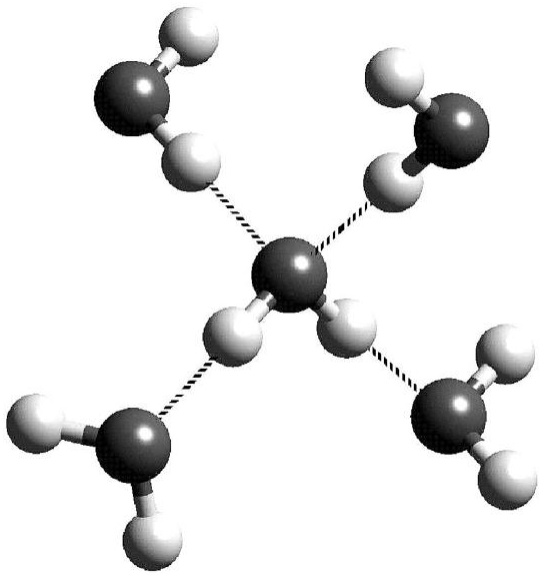

Figure 1.1 A four-coordinated water molecule showing the classic tetrahedral arrangement of the first-neighbor environment of a water molecule hydrogen-binding to four neighbors. The hydrogen atom attached to a relatively electronegative atom is a hydrogen bond donor. The electronegative atom, such as the oxygen atom, is a hydrogen bond acceptor. Based on the transfer of electron density, the central molecule ‘donates’ two hydrogen bonds to its two lower neighbors and ‘accepts’ a hydrogen bond from each of its two upper neighbors [6].

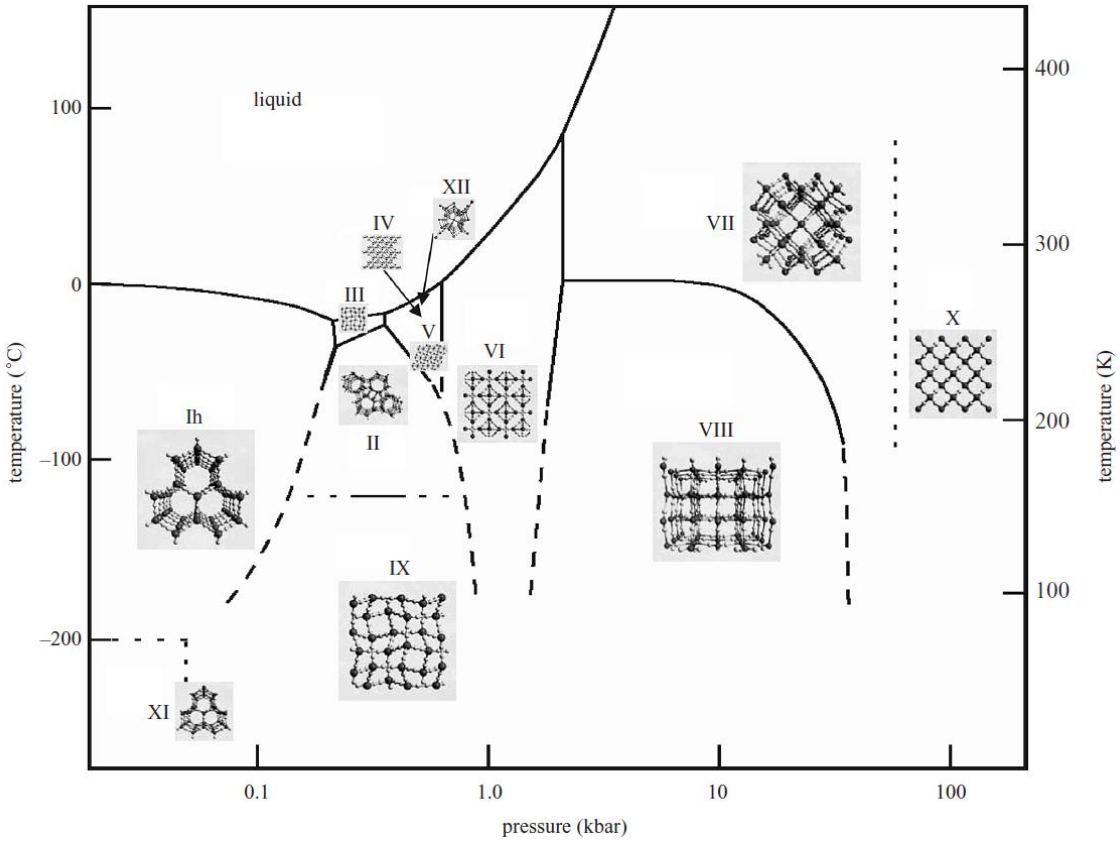

Figure 1.2 The phase diagram of ice [6].

1.1.2 Nanoconfined and interfacial water

The role of water in protein stability and folding was first proposed by Kauzmann [8]. He pointed out that an interaction mediated by water, the hydrophobic interaction, causes the clustering of hydrophobic units [9]. The facts that oil and water don't mix and tend to segregate is the consequence of the hydrophobicity, where polar and charged components 'like' water (hydrophilic, from Greek '*hydros*' (water) and '*philia*' (love)) and apolar components 'hate' water (hydrophobic, from Greek '*hydros*' (water) and '*phobos*' (fear)) [10]. Similar effects could influence more complicated assemblies such as biological structures that consists of both hydrophobic and hydrophilic components [9]. The driving

force for the biomolecule to fold into its native structure comes from the different interactions of its hydrophobic and hydrophilic components with the interfacial water.

Water certainly plays an essential role in Kauzmann's picture. The details of its role in protein folding, structure stability, dynamics and function remain unclear [11-15]. As the power of molecular dynamics increases, such elucidation of details becomes possible with an explicit description of each solvent molecule [16]. For instance, how could an amino acid chain find its native structure from an astronomical number of possible configurations [17, 18]? How does the water-protein interaction affect the structure and dynamics of interfacial water and proteins [15, 19-21]?

It is even more interesting to notice that water could be present in many biomolecular cavities and channels at nanometer scale, such as those in Chaperone and ion channels [22-25]. Ion channels are pore-forming membrane proteins that help establish and control the voltage gradient across the plasma membrane of cells. The behavior of water at this dimension could differ significantly from that in the bulk [24, 26]. The hydrophobic effect could also depend on the length scale [9, 27, 28]. Due to its importance for both fundamental understanding in thermodynamics and its application in biological processes, the study of water in nanoconfinement and at the interface of biomolecules has become a topic of current interest [29]. Figure 1.3 shows three examples of topics in this area: water at extended surfaces for the determination of hydrophobicity at the nanometer scale [30], at the interface of a biomolecule and its ligand, and confined and transported through a single-walled carbon nanotube [24, 26]. The majority of the above studies are based on molecular dynamics simulations. The number of available experimental results is much less due to the difficulty in obtaining the necessary experimental conditions or the lack of details in the experimental

results at a molecular level. It is the topic of this dissertation to provide and interpret experimental results on water in nanoscopic confinement and at the interface of biomolecules.

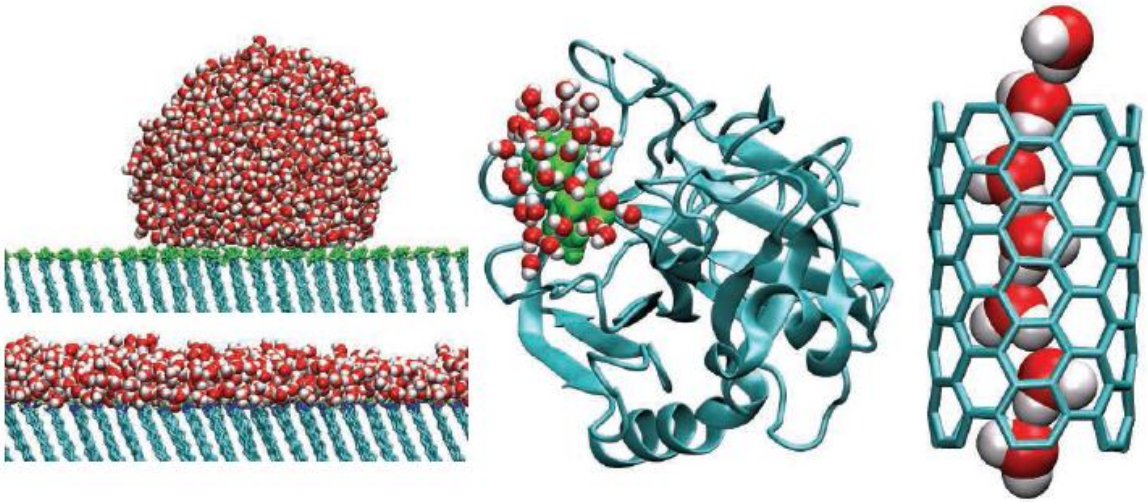

Figure 1.3 How water behaves at different hydrophobic elements: extended surfaces, biomolecules, and SWNTs [29].

1.1.3 Dissertation outlines

This dissertation consists of water adsorption results in several nanoporous materials and biomolecules. I use adsorption isotherms measured by NMR to study the interactions between the probe molecules (water/gas) with a variety of surfaces as illustrated in Figure 1.4. The first topic of this dissertation is the water in nanoscopic confinement. In CHAPTER 2, I discuss a temperature-induced hydrophobic-hydrophilic transition observed by water adsorption in SWNTs. This suggests the hydrophobicity could change in response to the structure of interfacial and nanoconfined water. In CHAPTER 3, I describe the observation that water adsorption demonstrates signatures of capillary condensation. The condensation pressure correlates with the pore size in a way similar to the Kelvin equation. The question is

raised whether the water at nanometer scale obeys the macroscopic Kelvin equation. In the following chapters, I start to discuss the study on the water at the interface of proteins. In CHAPTER 4, I discuss a significant decrease of hydration water in the proximity of lysozyme at temperatures below 8°C. I explain this by the reduced protein flexibility and enhanced cost in elastic energy for accommodating the hydration water at lower temperature based on the modified Flory-Huggins theory. Similar effects were also observed in hemoglobin and myoglobin as shown in CHAPTER 5. The dynamics of hydration water was studied based on the NMR spin-lattice relaxation in the presence of paramagnetic centers. Based on all the above understanding of protein hydration, in CHAPTER 6 I extend our study to the role of interfacial water in mediating the protein-anesthetic interaction. I provide evidences that the apolar molecule halothane, an inhaled general anesthetic, can be adsorbed on proteins only in the presence of interfacial water.

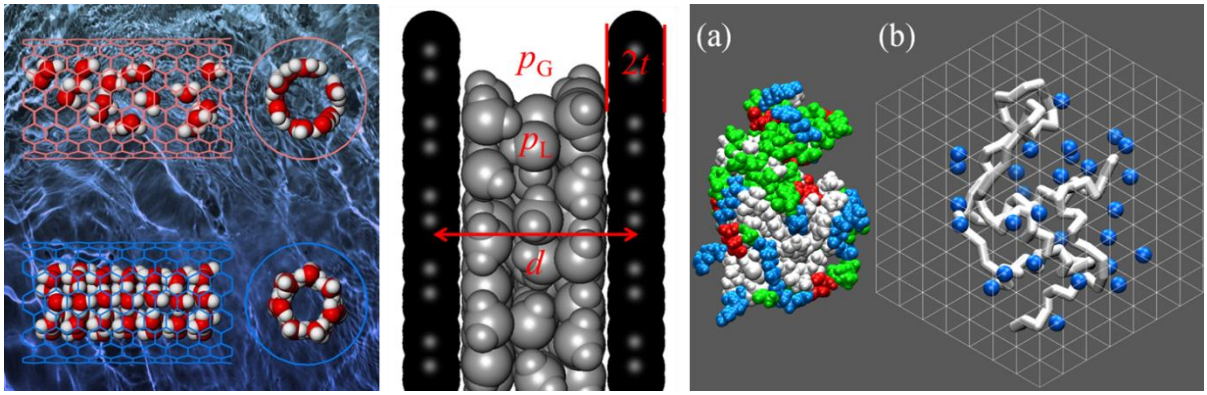

Figure 1.4 Illustration of water adsorption in SWNTs, in microporous activated carbons derived from PEEK, and on the surface of biomolecules.

1.2 Adsorption

A gas molecule can move along straight paths until it collides with other gas molecules or a surface. Collisions between two gas molecules exchange energy and momentum. Upon

hitting a surface, the gas molecule may lose most of its kinetic energy and momentum and stay on the surface for a certain length of time before regaining enough energy to re-evaporate. This phenomenon is called adsorption. Adsorption is a fundamental process that could reveal important surface properties such as the interaction between the gas (adsorbate) and the surface (adsorbent). The existing theories of adsorption were established to relate the measured quantities with surface properties based on fundamental physical principles [31, 32].

1.2.1 Basic quantities

If n gas molecules strike a unit area of a surface per unit time and remain there for an average time of τ, the adsorbed number of molecules per unit area of surface is $\sigma = n\tau$. Base on the kinetic theory of gasses, the number n can be expressed as

$$n = \frac{N_A p}{\sqrt{2\pi MRT}} = 3.52 \times 10^{22} \times \frac{p \text{ (torr)}}{\sqrt{MT}} \qquad (1.1)$$

where N_A is the Avogadro constant, R the gas constant, M the molecular weight, T the temperature, and p the pressure in unit of torr or millimeters of mercury. n is a very large number. For instance, at a temperature of 20°C and nitrogen pressure of 760 torr, there are more than two moles of nitrogen molecules colliding with a surface within an area of 1 cm^2. Such a large number generally suggests that the adsorption establishes equilibrium with surface molecules practically instantaneously [31]. In a real experiment, it always requires some time to reach adsorption equilibrium. Such a delay is caused by the transportation of molecules that are bought from distant locations to the adsorption surface.

The time of adsorption, τ, is given by $\tau = \tau_0 \exp(Q/RT)$, where τ_0 is the time of oscillation of the molecules in the adsorbed state, referring especially to vibrations

perpendicular to the surface, and Q is the heat of adsorption. τ_0 doesn't depend on the time of vibration of the constituent molecules or atoms of the adsorbing surface, but is often of the same order of magnitude, namely, $10^{-12} \sim 10^{-14}$ s.

1.2.2 Langmuir isotherm

Langmuir developed a simple picture of adsorption, namely a unimolecular layer of adsorbed molecules. He assumed that the heat of adsorption is identical for every molecule that collides with a bare surface and there is no interaction between gas molecules, and that every molecule colliding with a molecule already adsorbed on the surface returns to the gas phase. This simple assumption establishes an expression for the number of adsorbed molecules:

$$\sigma = n\left(1 - \frac{\sigma}{\sigma_0}\right)\tau \tag{1.2}$$

where σ_0 is the number of molecules in a completely filled unimolecular layer on the surface. This is equivalent to

$$\sigma = \frac{\sigma_0 n\tau}{\sigma_0 + n\tau} \tag{1.3}$$

or

$$\theta = \frac{\sigma}{\sigma_0} = \frac{n\tau / \sigma_0}{1 + n\tau / \sigma_0} = \frac{kp}{1 + kp} \tag{1.4}$$

where I have already used Eq. (1.1) with

$$k = \frac{n\tau}{p\sigma_0} = \frac{N_A \tau}{\sigma_0 \sqrt{2\pi MRT}} \tag{1.5}$$

The Langmuir isotherm could also be derived from a pure statistical mechanics point of view. Unimolecular layer adsorption is equivalent to finding the number of molecules that occupy sites with energy of $-\varepsilon$ on the surface, where the free gas has an energy of 0. The partition function of one particle is

$$Q(\sigma,\sigma_0,T)=\frac{\sigma_0!}{\sigma!(\sigma_0-\sigma)!}\left[\lambda\exp(\beta\varepsilon)\right] \tag{1.6}$$

where $\lambda=\dfrac{p}{kT\left(MkT/2\pi\hbar^2\right)^{3/2}}$. The partition function becomes

$$\mathbb{Z}=\sum_{\sigma=0}^{\sigma_0}\binom{\sigma_0}{\sigma}\left[\lambda\exp(\beta\varepsilon)\right]=\left[1+\lambda\exp(\beta\varepsilon)\right]^{\sigma_0} \tag{1.7}$$

The number of molecules adsorbed on the surface is given by

$$\theta=\frac{\langle\sigma\rangle}{\sigma_0}=\frac{1}{\sigma_0}\cdot\frac{\partial\ln\mathbb{Z}}{\partial\beta\varepsilon}=\frac{\lambda\exp(\beta\varepsilon)}{1+\lambda\exp(\beta\varepsilon)} \tag{1.8}$$

This is identical to Eq. (1.4).

1.2.3 Multimolecular adsorption and Brunauer-Emmett-Teller isotherm

There are scenarios that suggest the interaction between gas molecules can not be negligible. When a gas molecule collides with an adsorbed molecule on the surface, there is possibility that the gas molecule is adsorbed on top of an already adsorbed molecule. This is called multimolecular adsorption. I denote the fraction of the surface covered with unimolecular thickness as θ_1, the fraction with thickness of two molecules is θ_2, etc. The total number of molecules is

$$\sigma=\sigma_0\theta_1+2\sigma_0\theta_2+3\sigma_0\theta_3+\cdots+i\sigma_0\theta_i+\cdots=\sigma_0\sum_{i=1}^{i=\infty}i\theta_i \tag{1.9}$$

The number of molecules striking the bare surface, $n\theta_0 = n\left(1-\sum_{i=1}^{i=\infty}\theta_i\right)$, must equal to the number of molecules that evaporate from fraction θ_1, which is $\sigma_0\theta_1/\tau$. For the rest of the layers above, the time of adsorption, τ_1, is different from that for the first layer, τ. Here I assumed τ_1 is identical for all layers. Continuing the argument for all thickness, I get

$$\begin{aligned} \sigma_0\theta_1 &= n\theta_0\tau \qquad \text{i=1} \\ \sigma_0\theta_i &= n\theta_{i-1}\tau_1 \qquad \text{i>1} \end{aligned} \tag{1.10}$$

The total number of molecules adsorbed on the surface is

$$\sigma = \sigma_0\sum_{i=1}^{i=\infty} i\theta_i = \sigma_0\frac{\tau}{\tau_1}\theta_0\sum_{i=1}^{i=\infty} i\left(\frac{n\tau_1}{\sigma_0}\right)^i = \frac{k\sigma_0 x}{(1-x)(1-x+kx)} \tag{1.11}$$

where $x = \frac{n\tau_1}{\sigma_0} = \frac{N\tau_1}{\sigma_0\sqrt{2\pi MRT}}\,p = p/q$, and $k = \tau/\tau_1$, or

$$\sigma/\sigma_0 = \frac{kp}{(q-p)\left[1+(k-1)\,p/q\right]} \tag{1.12}$$

This is the basic form of the Brunauer-Emmett-Teller (BET) isotherm.

1.2.4 Classification of isotherms

Langmuir and BET isotherms are two simple but important examples of adsorption. In general, due to the complexity of the attraction force between the gas and the solid, the isotherms show a variety of patterns. International Union of Pure and Applied Chemistry (IUPAC) recommends the following classification for the characterization of porous solids as shown in Figure 1.5. Type I is a typical Langmuir isotherm. The physical adsorption of gases by microporous solids shows the signature of a Type I isotherm. Type II corresponds to the physical adsorption of gases by nonporous solids, while Type IV is typical for gas adsorption by mesoporous solids. Type III and V appear for the special adsorption behavior of water [32].

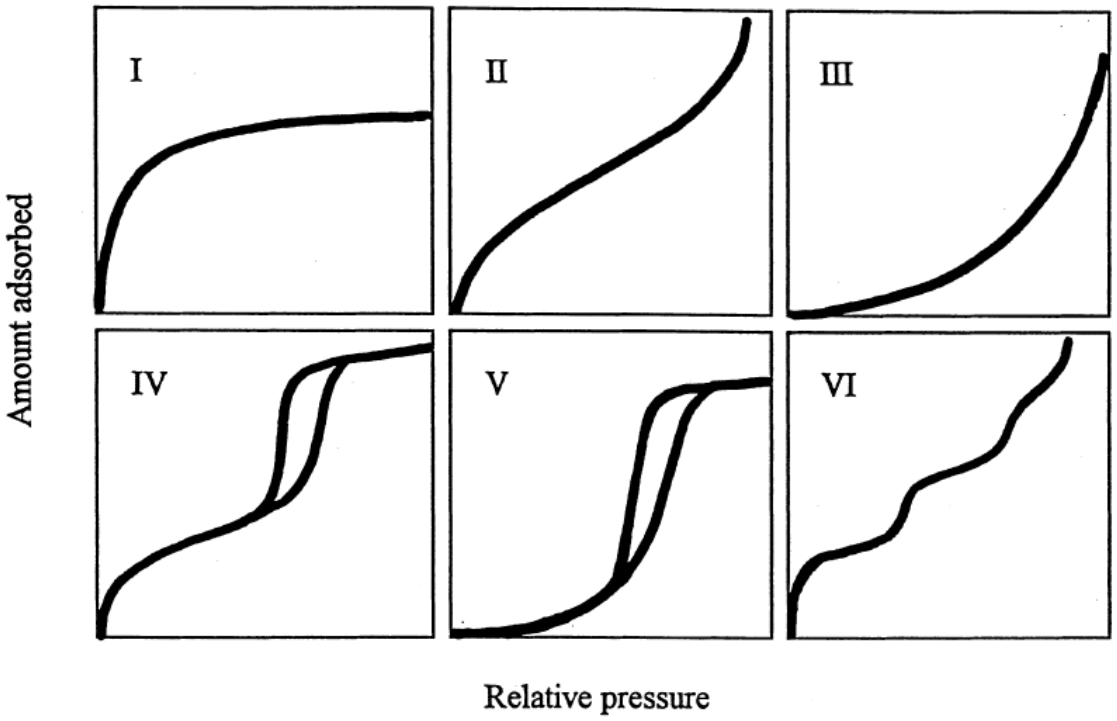

Figure 1.5 The IUPAC classification of adsorption isotherms for gas-solid equilibria [33].

1.2.5 Uniqueness of water adsorption

In this dissertation, I focus primarily on the adsorption behavior of water in several materials, including SWNTs, microporous activated carbon, and biomolecules. The fundamental assumption of the surface adsorption model does not apply to these systems with either the confined space or complicated surface properties. For instance, in CHAPTER 2, I identified the signature of water inside SWNTs, a tubular structure formed by rolling a single sheet of carbon atoms. As the temperature changes from 18°C to 8°C, the isotherm changes dramatically from Type III to Type I, indicating a significant change of hydrophobicity. Such a change can be explained by a change in the local excess chemical potential. In CHAPTER 3, capillary condensation dominates the adsorption process and shows a signature of a Type V isotherm. The condensation pressure correlates well with the

pore size, similar to what the Kelvin equation describes. This raises the question whether theories for the bulk phase, like the Kelvin equation, remain valid at the nanoscale. From CHAPTER 4 to CHAPTER 6, I will discuss results for water adsorption in biomolecules. At low temperature, there is a significant decrease of hydration water at high relative vapor pressure. This can not be explained by the surface adsorption picture. A solution picture based on the Flory-Huggins theory and a term originating from the elastic energy has to be introduced to account for the observed temperature dependence. The adsorption of anesthetic gas in dry and wet proteins also demonstrates behaviors beyond the surface adsorption model.

1.3 Nuclear Magnetic Resonance

Adsorption isotherms are generally measured by the volumetric or gravimetric method [32]. Both methods can only measure the adsorption isotherms for one kind of adsorbate at a time. They can only tell the amount, either mass or volume, of adsorbate. NMR has been used to measure isotherms for adsorbates containing nuclear spins. Many common important adsorbates, such as H_2 for hydrogen storage [34], CH_4 for natural gas exploration and storage [35], H_2O for nanoconfined and biological systems [36], contain the ^1H nucleus. These molecules could be used as molecular probes for the characterization of micropores [34, 37, 38]. Many inhaled general anesthetics contain ^1H, ^{19}F or ^{129}Xe. Both ^1H and ^{19}F are perfect choices from the point view of NMR. NMR has no difficulty in separating two or more nuclear species through their different resonating frequencies. Even for the same nucleus from different molecules, or even from different local environments of the same molecule, NMR shows the possibility to separate them through chemical shift, spectral line shape, and relaxation time. The relaxation time could also reveal the dynamical characters of adsorbates

and the interaction between adsorbates and adsorbents. It is therefore useful to review some of the basic concepts of NMR prior to its application in measuring adsorption isotherms.

Table 1.1 Gyromagnetic ratio of nuclei used in NMR and electron used in EPR.

Nucleus	Spin	Natural Abundance (%)	$\gamma\ \left(10^6\ \text{rad}\cdot\text{s}^{-1}\cdot\text{T}^{-1}\right)$	$\gamma/2\pi\ \left(\text{MHz}\cdot\text{T}^{-1}\right)$
^{1}H	1/2	99.9885	267.513	42.576
^{3}He	1/2	0.00014	41.065	6.536
^{7}Li	3/2	92.410	103.962	16.546
^{13}C	1/2	1.07	67.262	10.705
^{19}F	1/2	100	251.662	40.053
^{129}Xe	3/2	21.180	-73.997	-11.777
electron	1/2	100	-1.76×10^{5}	-2.8×10^{4}

1.3.1 Magnetization

Many atomic nuclei have non-zero spin angular momentum $I\hbar$ and a dipolar magnetic moment $\mu=\gamma\hbar I$ collinear with it, where γ is gyromagnetic ratio. When placed in a magnetic field H_0 in z direction, nuclear spins in the ensemble quantize along the magnetic field with a quantum number of $I_z=m$, leading to different magnetic energy $E_m=-\vec{\mu}\cdot\vec{H}_0=-\gamma\hbar mH_0$. The populations P_m of the energy levels are proportional to $\exp\left(-E_m/kT\right)=\exp\left(\gamma\hbar mH_0/kT\right)$. The net magnetization of N spins become [39]

$$M = N\gamma\hbar \frac{\sum_{m=-I}^{I} m \exp\left(\gamma\hbar m H_0 / kT\right)}{\sum_{m=-I}^{I} \exp\left(\gamma\hbar m H_0 / kT\right)} \tag{1.13}$$

With high temperature approximation, $\gamma\hbar H_0 / kT \ll 1$, the net magnetization reduces to

$$M = \frac{N\gamma^2\hbar^2 I\left(I+1\right)}{3kT} H_0 \tag{1.14}$$

Table 1.1 shows the gyromagnetic ratio of several important nuclei that are commonly used in NMR. The gyromagnetic ratio of the electron is much larger than that of nuclei. The basic principles used in NMR are also applied in EPR [40]. When subject to external perturbation, such as an oscillating magnetic field at the Larmor frequency, γH_0, perpendicular to the static field, the net magnetization will start processing like a single spin. The change of magnetization will be determined by its Hamiltonian.

1.3.2 Interactions

The Hamiltonian of a single spin in an alternating magnetic field in terms of the amplitude H_x^0 is

$$\mathcal{H} = -\gamma\hbar H_o I_z - \gamma\hbar H_x^0 I_x \cos\omega t \tag{1.15}$$

For an ensemble of nuclear spins, there are many other interactions need to be included in the Hamiltonian. The interaction between two magnetic moments $\boldsymbol{\mu}_1 = \gamma_1\hbar\boldsymbol{I}_1$ and $\boldsymbol{\mu}_2 = \gamma_2\hbar\boldsymbol{I}_2$ in classical electrodynamics gives the expression of the quantum mechanical Hamiltonian for dipolar interaction [40]

$$\mathcal{H}_d = \frac{\boldsymbol{\mu}_1 \cdot \boldsymbol{\mu}_2}{r^3} - \frac{3\left(\boldsymbol{\mu}_1 \cdot \boldsymbol{r}\right)\left(\boldsymbol{\mu}_2 \cdot \boldsymbol{r}\right)}{r^5} \tag{1.16}$$

Dipolar interaction is the dominant interaction in the majority of this dissertation.

Nuclear spins could also interact with electrons through magnetic interactions. For instance, the chemical shift originates from the orbital motion of electrons. The orbital motion of electrons changes in response to the external field, and thus alters the magnetic field at the nuclear spin. Such a change in local magnetic field is expressed in terms of resonance frequency

$$\omega = \gamma\left(H_0 + \Delta H\right) = \gamma H_0\left(1-\sigma\right) \tag{1.17}$$

where σ is independent of H_0. When the nucleus and electron are far apart, they could interact through the dipolar interaction

$$\mathcal{H}_{en} = \frac{\boldsymbol{\mu}_e \cdot \boldsymbol{\mu}_n}{r^3} - \frac{3\left(\boldsymbol{\mu}_e \cdot \boldsymbol{r}\right)\left(\boldsymbol{\mu}_n \cdot \boldsymbol{r}\right)}{r^5} \tag{1.18}$$

For the s-state of electrons, the electron wave function is nonzero at the nucleus. This hyperfine interaction has Hamiltonian

$$\mathcal{H}_{hf} = \frac{8\pi}{3}\gamma_e\gamma_n\hbar^2\boldsymbol{I}\cdot\boldsymbol{S}\delta\left(\boldsymbol{r}\right) \tag{1.19}$$

where $\boldsymbol{I}$ and $\boldsymbol{S}$ are the nuclear and electron spin respectively, and $\delta\left(\boldsymbol{r}\right)$ is the electron density at the nucleus. The nuclear-electron interaction is essential in the understanding of the relaxation mechanism in myoglobin and hemoglobin, where unpaired electrons are present in the molecule.

1.3.3 Relaxation

The Bloch equations describe the time evolution of the net magnetization in a classical picture.

$$\begin{aligned}
\frac{dM_x}{dt} &= \gamma\left(\boldsymbol{M}\times\boldsymbol{H}\right)_x - \frac{M_x}{T_2} \\
\frac{dM_y}{dt} &= \gamma\left(\boldsymbol{M}\times\boldsymbol{H}\right)_y - \frac{M_y}{T_2} \\
\frac{dM_z}{dt} &= \frac{M_0 - M_z}{T_1} + \gamma\left(\boldsymbol{M}\times\boldsymbol{H}\right)_z
\end{aligned} \tag{1.20}$$

After a perturbation such as a RF pulse at the resonant frequency, $\boldsymbol{M}$ has been moved away from its thermal equilibrium value $\boldsymbol{M}_0$. In the absence of external perturbation, the net magnetization tends to move towards M_0. In the longitudinal direction, any change of M_z is associated with energy transfer from the nuclear spin to its surroundings, therefore the time constant T_1 is called the spin-lattice relaxation time. On the other hand, in the transverse plane, T_2 characterizes the time needed for spins lose their coherence. No energy is transferred during the spin-spin relaxation process.

In liquids and gases, molecules are experiencing constant rotational tumbling and relative translational motion. Migrations of atoms or groups of atoms from one molecule to another are common in the chemical exchange process. If the interaction between nuclear spins depends on their relative distance and direction, such as the dipolar interaction, these motions provide one of the relaxation mechanisms. The relaxation times for like spins are given by [39]

$$\begin{aligned}
\frac{1}{T_1} &= \frac{3}{2}\gamma^4\hbar^2 I\left(I+1\right)\left[J^{(1)}\left(\omega_I\right) + J^{(2)}\left(2\omega_I\right)\right] \\
\frac{1}{T_2} &= \gamma^4\hbar^2 I\left(I+1\right)\left[\frac{3}{8}J^{(0)}\left(0\right) + \frac{15}{4}J^{(1)}\left(\omega_I\right) + \frac{3}{8}J^{(2)}\left(2\omega_I\right)\right]
\end{aligned} \tag{1.21}$$

where the second-rank tensor J is the Fourier transformation of the spectral density of the dipolar interaction. If the rotational motion of two spins is considered, then

$$J^{(0)} = \frac{1}{b^6}\frac{24}{15}\frac{\tau}{1+\omega^2\tau^2}$$
$$J^{(1)} = \frac{1}{b^6}\frac{4}{15}\frac{\tau}{1+\omega^2\tau^2} \qquad (1.22)$$
$$J^{(2)} = \frac{1}{b^6}\frac{16}{15}\frac{\tau}{1+\omega^2\tau^2}$$

where b is the distance between two spins, ω is the Larmor period, and τ is the correlation time. These lead to these expressions for relaxation times:

$$\frac{1}{T_1} = \frac{3\gamma^4\hbar^2}{10b^6}\left(\frac{\tau}{1+\omega_0^2\tau^2} + \frac{4\tau}{1+4\omega_0^2\tau^2}\right)$$
$$\frac{1}{T_2} = \frac{3\gamma^4\hbar^2}{20b^6}\left(3\tau + \frac{5\tau}{1+\omega_0^2\tau^2} + \frac{2\tau}{1+4\omega_0^2\tau^2}\right) \qquad (1.23)$$

1.4 Experimental Setup

Several NMR spectrometers, at ^{1}H NMR frequency of 34 MHz, 200 MHz, and 300 MHz, are available for *in situ* gas and water loading experiments in our lab. The schematics of such adsorption apparatus are shown in Figure 1.6 and Figure 1.7. The basic components are a vacuum chamber connected to a mechanical pump, a pressure gauge, the NMR sample tube, and the source of water vapor or gas. Such a vacuum chamber can be made from glass for pressure lower than 1 atm, or from stainless steel for high pressure experiments.

A high-pressure *in situ* gas/liquid loading system is also commercially available from Daedalus Innovations. The core design of such system is described in details in reference [41]. The material used to fabricate the high-pressure NMR tube is alumina-toughened zirconia (AZO). The stainless steel tubing with i.d. = 1/8" was used for connections to reduce the total volume in the system.

With such an *in situ* gas loading system attached to the NMR spectrometer, adsorption could be studied with isotherms measured by NMR on a serious of adsorbates such as water, hydrogen gas, methane and natural gas, and many other gases containing nuclear spins, such as inhaled general anesthetics.

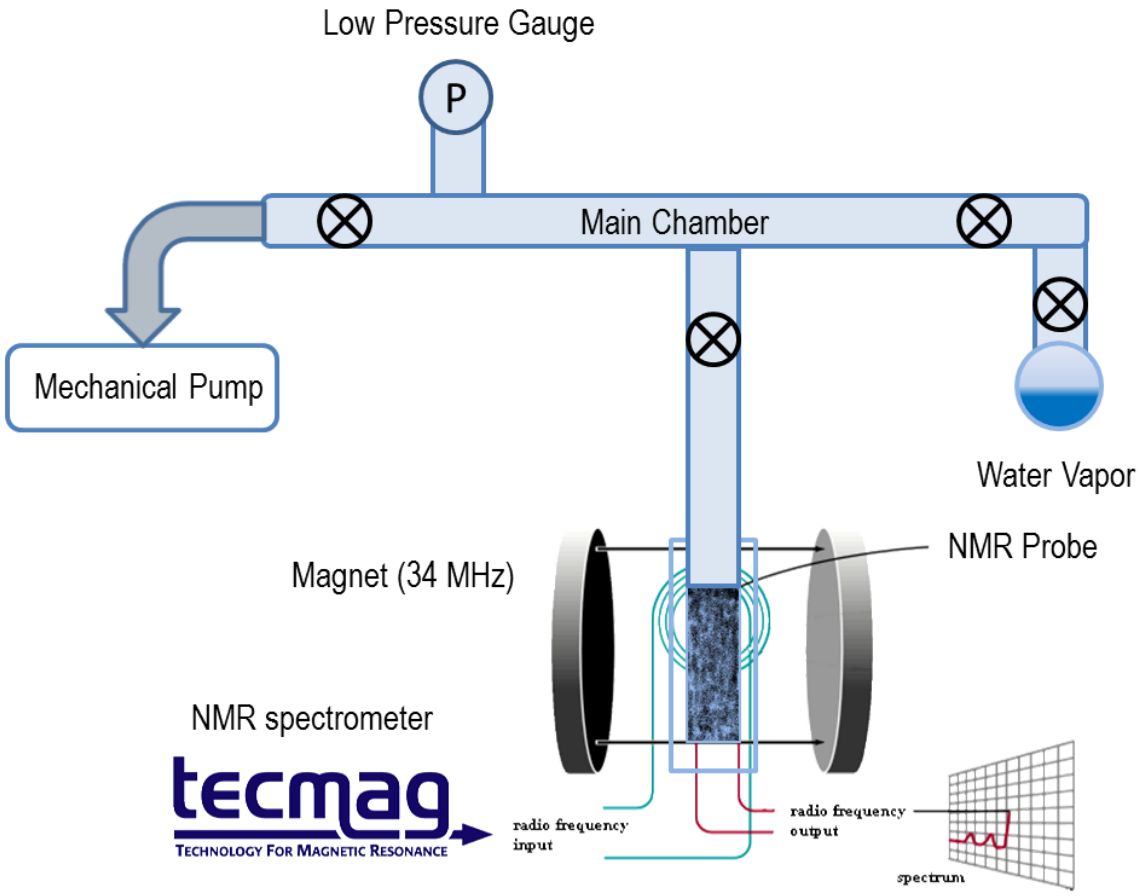

Figure 1.6 *In situ* water loading system for NMR spectrometer at 34 MHz.

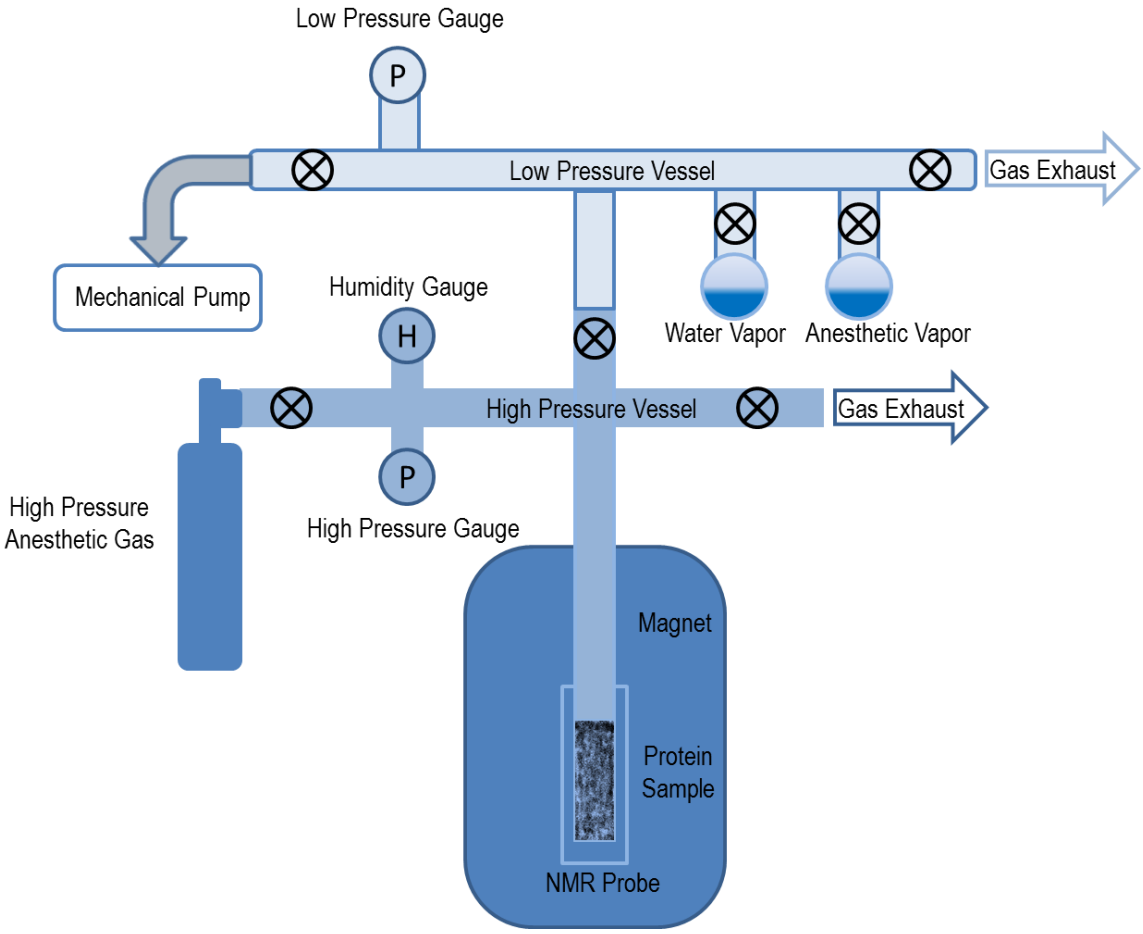

Figure 1.7 *In situ* gas and vapor loading system for NMR spectrometer at 300 MHz.

1.5 References

[1] D. S. Eisenberg, and W. Kauzmann, *The structure and properties of water* (Clarendon Press; Oxford University Press, New York; Oxford 2005).

[2] F. Franks, *Water, a comprehensive treatise* (Plenum Press, New York, 1972).

[3] F. Franks, *Water: a matrix of life* (Royal Society of Chemistry, Cambridge, 2000).

[4] P. Ball, *Life's matrix : a biography of water* (Farrar, Straus, and Giroux, New York, 2000).

[5] M. Chaplin, http://www.lsbu.ac.uk/water/index.html

[6] J. L. Finney, Philos. Trans. R. Soc. Lond., B, Biol. Sci. **359**, 1145 (2004).

[7] K. A. Dill, *Molecular driving forces : statistical thermodynamics in chemistry and biology* (Garland Science, New York, 2003).

[8] W. Kauzmann, Adv. Protein. Chem. **14**, 1 (1959).

[9] D. Chandler, Nature **437**, 640 (2005).

[10] D. Chandler, Nature **417**, 491 (2002).

[11] H. Frauenfelder, *Physics of proteins: an introduction to biological physics and molecular biophysics* (Springer, New York ;London, 2010).

[12] H. Frauenfelder *et al.*, Proc. Natl. Acad. Sci. USA **106**, 5129 (2009).

[13] H. Frauenfelder *et al.*, Proc. Natl. Acad. Sci. USA **103**, 15469 (2006).

[14] H. Frauenfelder, P. W. Fenimore, and B. H. McMahon, Biophys. Chem. **98**, 35 (2002).

[15] R. M. Daniel *et al.*, Annu. Rev. Biophys. Biomol. Struct. **32**, 69 (2003).

[16] G. A. Papoian *et al.*, Proc. Natl. Acad. Sci. USA **101**, 3352 (2004).

[17] K. A. Dill, and H. S. Chan, Nat. Struct. Biol. **4**, 10 (1997).

[18] Y. Levy, and J. N. Onuchic, Annu. Rev. Biophys. Biomol. Struct. **35**, 389 (2006).

[19] R. G. Bryant, Annu. Rev. Biophys. Biomol. Struct. **25**, 29 (1996).

[20] I. D. Kuntz, and W. Kauzmann, Adv. Protein. Chem. **28**, 239 (1974).

[21] J. A. Rupley, and G. Careri, Adv. Protein. Chem. **41**, 37 (1991).

[22] D. A. Doyle *et al.*, Science **280**, 69 (1998).

[23] J. L. England, D. Lucent, and V. S. Pande, J. Am. Chem. Soc. **130**, 11838 (2008).

[24] J. C. Rasaiah, S. Garde, and G. Hummer, Annu. Rev. Phys. Chem. **59**, 713 (2008).

[25] S. Vaitheeswaran *et al.*, Proc. Natl. Acad. Sci. USA **101**, 17002 (2004).

[26] G. Hummer, J. C. Rasaiah, and J. P. Noworyta, Nature **414**, 188 (2001).

[27] D. M. Huang, and D. Chandler, Proc. Natl. Acad. Sci. USA **97**, 8324 (2000).

[28] K. Lum, D. Chandler, and J. D. Weeks, J. Phys. Chem. B **103**, 4570 (1999).

[29] S. Granick, and S. C. Bae, Science **322**, 1477 (2008).

[30] H. Acharya *et al.*, Faraday Discuss. **146**, 353 (2010).

[31] J. H. de Boer, *The dynamical character of adsorption* (Clarendon, Oxford, 1968).

[32] S. J. Gregg, and K. S. W. Sing, *Adsorption, Surface Area, and Porosity* (Academic Press, London, New York, 1982), pp. 228.

[33] J. Rouquerol *et al.*, Pure Appl. Chem. **66**, 1739 (1994).

[34] R. J. Anderson *et al.*, J. Am. Chem. Soc. **132**, 8618 (2010).

[35] A. Kleinhammes *et al.*, Phys. Rev. B **68**, 075418 (2003).

[36] H. J. Wang *et al.*, Science **322**, 80 (2008).

[37] H. J. Wang, A. Kleinhammes, and Y. Wu, (in preparation).

[38] H. J. Wang *et al.*, Phys. Rev. E **83**, 031924 (2011).

[39] A. Abragam, *The Principles of Nuclear Magnetism* (Clarendon Press, Oxford, 1961).

[40] C. P. Slichter, *Principles of magnetic resonance* (Springer-Verlag, Berlin ;New York, 1990).

[41] R. W. Peterson, and A. J. Wand, Rev. Sci. Instrum. **76** (2005).

CHAPTER 2

TEMPERATURE-INDUCED HYDROPHOBIC-HYDROPHILIC TRANSITION OBSERVED BY WATER ADSORPTION

2.1 Introduction

Water in the immediate vicinity of hydrophobic surfaces plays a crucial role in various important phenomena such as the folding and activity of proteins [1, 2], but experimental signatures of these water layers have been proven difficult to obtain. One possibility is that the structures and dynamics of nanoconfined interfacial water could possess distinctive temperature dependences (analogous perhaps to the anomalous density maximum manifested by bulk water at 4°C). A temperature dependence in the properties of interfacial water could be important for various processes, such as the cold denaturation of proteins [2].

Single-walled carbon nanotubes (SWNTs) provide a model system for investigating the properties of nanoconfined interfacial water [3-9]. Because each nanotube with diameter of 1.4 nm can only accommodate one layer of water molecules on its inside surface [5], the behavior of adsorbed water inside such SWNTs could provide important insight into the properties of nanoconfined interfacial water. A previous theoretical study showed that water could fill the interior of carbon nanotubes through favorable structural effects on the local excess chemical potential [3]. This result implies that water could be adsorbed inside SWNTs below the saturated vapor pressure, as demonstrated by previous studies [10, 11]. However, in those studies, the defect density and principal adsorption sites (PAS), known to alter water

adsorption isotherms in activated carbon [12], were likely too high to reveal the intrinsic adsorption properties of SWNTs. Water adsorption isotherms in SWNTs depend on both the interaction with the surface and the structure of the adsorbed water, which could depend on temperature. Here I report a hydrophobic-hydrophilic transition upon cooling from 22.1°C to 8.0°C, revealed by water adsorption isotherms on the inside surfaces of low-defect SWNTs. Strong evidence is provided for the formation of monolayer water inside SWNTs at 8.0°C. Nuclear magnetic resonance (NMR) studies show the dynamics of the reorientation of nanoconfined water molecules to be much slower than in bulk water. In addition to various important biological processes, this new phenomenon could also shed light on the intrinsic adsorption mechanism of water in nanoporous carbon [12, 13].

2.2 Experiments

The SWNTs were synthesized by laser ablation using 0.6 weight percent (each) Ni/Co as catalysts. The raw material was purified by refluxing in 20% H_2O_2 solution at 100°C for 12 hours and rinsing in CS_2 and then in methanol. The purified SWNTs were then annealed at 800°C. The tube diameter of 1.4 nm was determined from the Raman spectrum. Details of the sample preparation were described previously [14]. The transmission electron microscope (TEM) image of the SWNTs is shown in Figure 2.1. SWNTs after annealing usually have end caps that prevent the guest molecules from being adsorbed inside. Several techniques can be used to open the ends of SWNTs. In our previous study, etching by strong acids was used to cut the tubes into short segments [10, 15, 16]. Although this method is effective for opening tubes, it introduces a considerable number of defect sites and functional groups acting as PAS that could have a strong influence on the water adsorption behavior. The high defect density in cut SWNTs could obscure the intrinsic adsorption behavior of SWNTs [10].

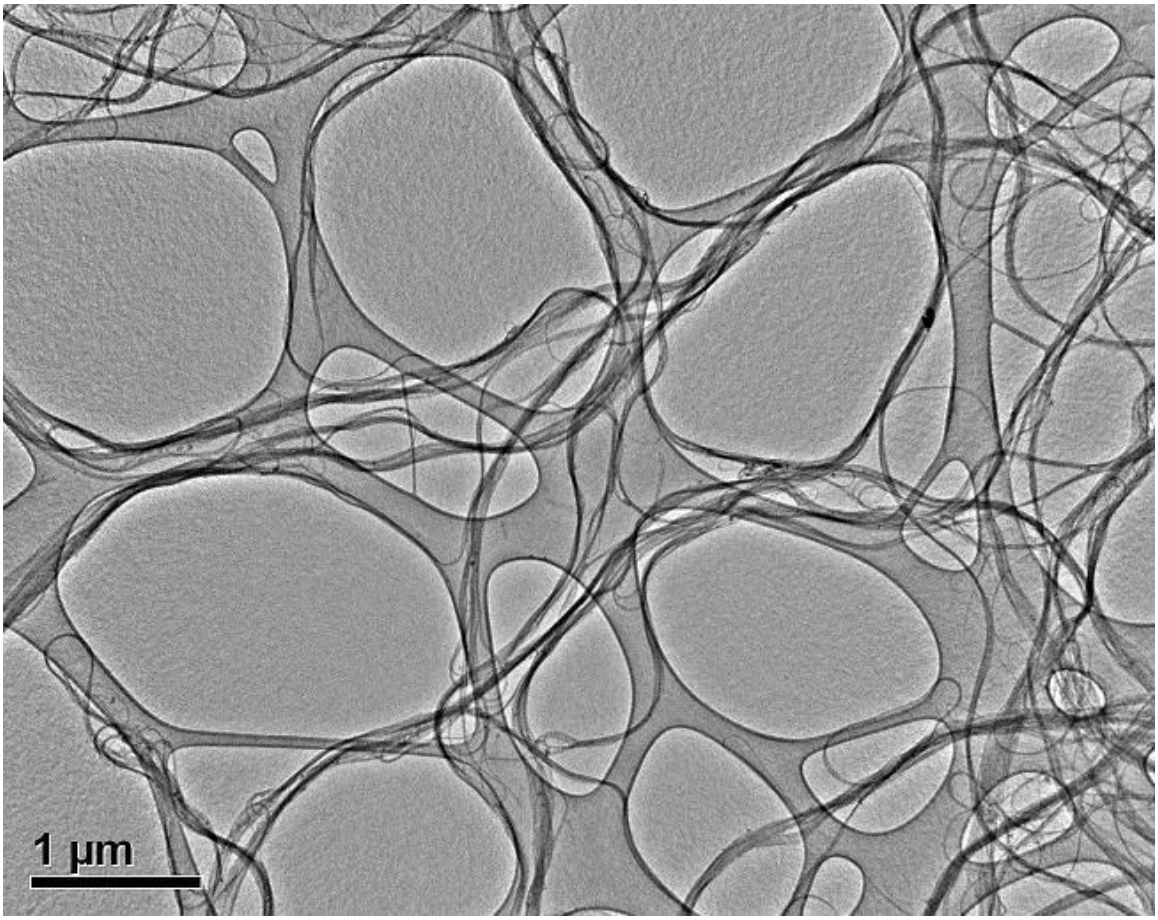

Figure 2.1 The TEM image of SWNTs. It shows that the samples in the current experiment are relatively long (>1µm) and devoid of magnetic particles.

To reduce the influence of PAS and to reveal the intrinsic adsorption behavior, a much gentler method was adopted here to remove the end caps [17]. The SWNTs were heated at around 350°C in a thermogravimetric analyzer under air flow for more than 20 min until a weight loss of about 3% was reached. ^{1}H NMR spectrum of ethane (Figure 2.2) adsorbed in such treated SWNTs shows clear signatures of opened SWNTs [15, 16]. Water adsorption isotherms were measured by ^{1}H NMR at 0.8 T (34 MHz ^{1}H NMR frequency) in apparatus equipped with an *in situ* water loading system with controlled vapor pressure and temperature. The ^{1}H NMR signal of the vapor is negligible because of its low pressure (~2

kPa); no bulk water is condensed outside the SWNTs below the saturated vapor pressure (P_0). Furthermore, water molecules are too large to access the interstitial sites of 1.4 nm diameter SWNTs bundles [15]. Thus, the ^{1}H NMR signal is associated predominantly with the water adsorbed inside the SWNTs [11]. The water content is calibrated by the ethane ^{1}H NMR spectra as described in details elsewhere [10, 15].

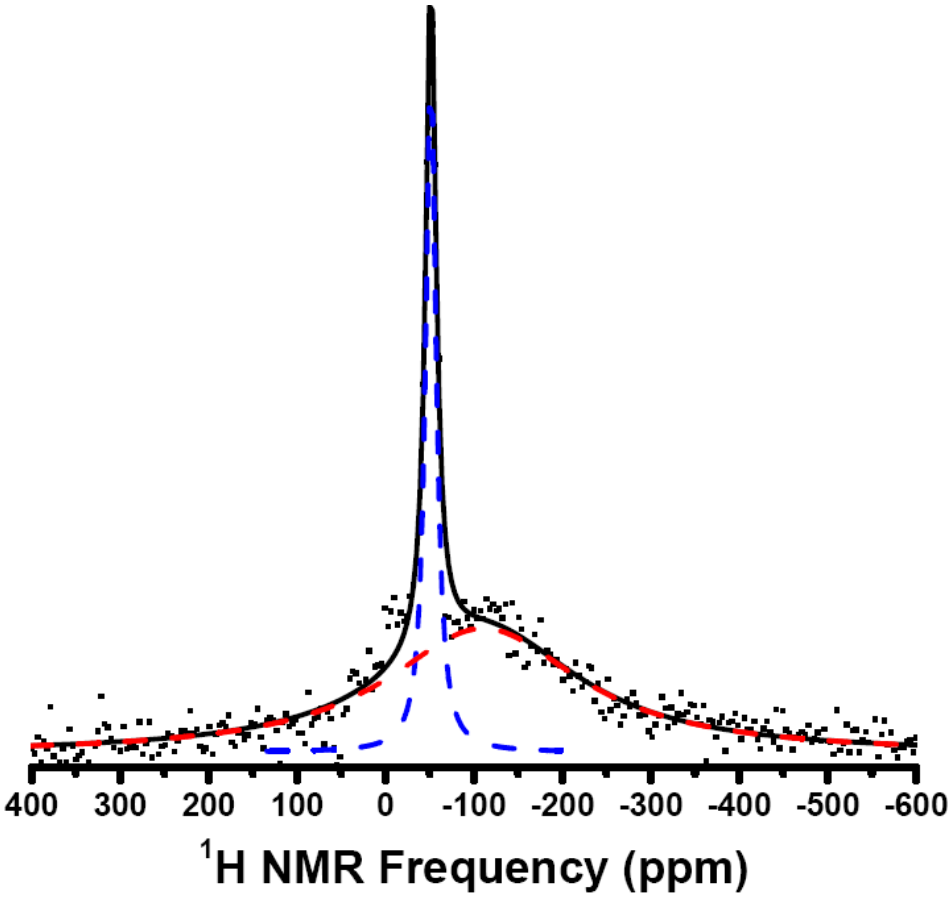

Figure 2.2 ^{1}H NMR spectrum of ethane adsorbed in SWNTs. The spectrum is taken at 108 kPa and at room temperature. The dashed lines are Lorentzian fits. The sharp peak (blue) and the broad peak (red) are assigned to the ethane outside and inside the SWNTs, respectively. This shows that the SWCNTs are open for adsorption.

2.3 Results and Discussion

2.3.1 Water adsorption isotherms in SWNTs

The amount of adsorbed water measured by ^{1}H NMR versus the relative pressure P/P_0 at 8.0°C, 18.4°C, and 22.1°C is shown in Figure 2.3A. All three isotherms differ substantially from the S-shaped type V isotherm as observed in activated carbon and defective cut SWNTs, where adsorption increases slowly at low relative pressure but increases sharply above P/P_0=0.5, quickly reaching the level of saturation [10]. Such an S-shaped adsorption isotherm in activated carbon is often attributed to PAS [12]. Figure 2.3A shows that this ubiquitous sharp increase in the isotherms of activated carbon near P/P_0=0.5 is absent in low-defect SWNTs. The isotherm at 22.1°C exhibits the concave pattern of a type III isotherm, typical for clean hydrophobic surfaces with surface-water interactions weaker than water-water interactions [18]. Interestingly, the isotherm at 8.0°C exhibits a convex pattern, a type II isotherm such as that observed on hydrophilic surfaces [19]. The isotherm at 18.4°C shows a linear pattern, which is a transitional pattern between the hydrophilic isotherm at 8.0°C and the hydrophobic isotherm at 22.1°C.

The water content was about 15 mmol/g when the relative pressure first reached the saturated pressure of P/P_0=1. This value is in good agreement with the calculated adsorption capacity of 13 mmol/g when SWNTs are supposed to be completely filled with water. This estimate is made by assuming that the van der Waals diameter of (10, 10) SWNTs is 0.99 nm [5] and the density of water is comparable to that at the hydrophobic interface, about 0.9 g/cm^3 [20]. Further exposure at P/P_0=1 will lead to further increase of adsorption caused by condensation outside the SWNTs.

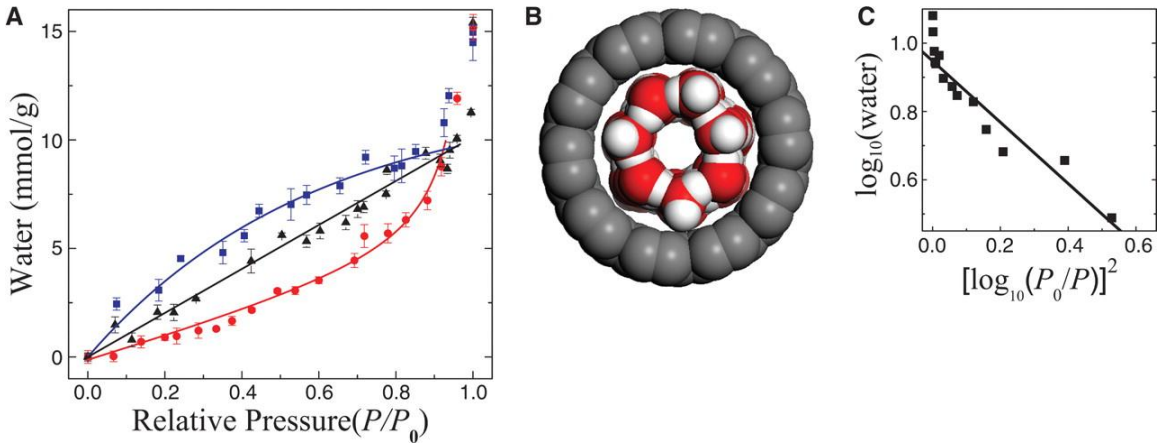

Figure 2.3 Water adsorption isotherms in SWNTs. (A) Three isotherms at 8.0°C (squares), 18.4°C (triangles), and 22.1°C (circles) are shown (The uncertainty of T is ±0.3°C). The lines are guides to the eye. The vertical error bars are shown when they are larger than the size of the symbols and the pressure uncertainty is less than 1% of P_0. (B) An illustration of monolayer water in SWNTs with a diameter of 1.36 nm. Monolayer adsorption forms a tube-like structure at 8.0°C under the constraint of the SWNTs. (C) A logarithmic plot of water content versus $[\log_{10}(P_0/P)]^2$ for the isotherm at 8.0°C, following the Dubbin-Radushkevitch-Kaganer equation.

2.3.2 Dubinin-Radushkevitch-Kaganer equation

More insight can be gained by analyzing the isotherm at 8.0°C with the Dubinin-Radushkevitch-Kaganer equation [18]. It describes monolayer adsorption, given by:

$$\log_{10} x = \log_{10} x_m - D\left[\log_{10}\left(P_0 / P\right)\right]^2 \qquad (2.1)$$

where x is the adsorbed water content, x_m is the monolayer capacity, and D is a constant related to the temperature. A logarithmic plot of the adsorbed water versus $[\log_{10}(P_0/P)]^2$ is shown in Figure 2.3C. Using a linear fit to the data below the pressure of condensation and extrapolating to $[\log_{10}(P_0/P)]^2=0$, the monolayer capacity x_m is evaluated to be 8.7±0.4 mmol/g. This value agrees well with the calculated value of 9.5 mmol/g for monolayer coverage of the inner surface of SWNTs. The monolayer water forms a tubular structure under the confinement of nanotubes as illustrated in Figure 2.3B [21]. The convex shape of

the water adsorption isotherm at 8.0°C and its upward turn at $P/P_0 \approx 0.8$ are also evidences of molecular layering on the adsorbed surface [22]. This layering effect is commonly seen in liquid films (above the triple-point temperature of the bulk liquid) of simple hydrocarbons and inert gases on graphite.

2.3.3 Local excess chemical potential

Water adsorption is a process of balancing the chemical potential of the confined water and the vapor. When water is confined in SWNTs, the energy loss from the breaking of hydrogen bonding (~20 kJ/mol) will not be completely compensated by the van der Waals interaction (<15 kJ/mol) [23]. However, the local excess chemical potential is dominated not by the average binding energy, but by the low binding energy part, as determined by:

$$\exp(\beta\mu^{ex}) = \langle \exp(\beta u) \rangle = \int p_{bind}(u) \exp(\beta u) du \qquad (2.2)$$

where $\beta = 1/k_B T$, $p_{bind}(u)$ is the probability distribution of binding energy u ($u < 0$), and μ^{ex} is the local excess chemical potential defined by the difference of chemical potential of water and that of an ideal gas under the same conditions [3].

At 8.0°C, water adsorption proceeds so as to form a monolayer. The binding energy for adsorbed water with an ordered water nanotube structure, as predicted theoretically [24, 25], is expected to be distributed within a narrower energy range than in bulk water. States of low binding energy are less frequently occupied. The chemical potential could be lower than that of the saturated vapor. Thus, substantial adsorption could happen even at low relative pressure at 8.0°C as shown in Figure 2.3A. At 22.1°C, the adsorbed water in SWNTs could possess a variety of local structures and a broader distribution in binding energy. More states could be located in the low binding energy region, leading to higher chemical potential and

an unfavorable condition for adsorption. Thus, much less water was adsorbed in SWNTs at 22.1°C than at 8.0°C.

2.3.4 NMR relaxation and molecular reorientation

To investigate the dynamics of adsorbed water molecules, the correlation time of molecular motion was estimated with ^{1}H spin-lattice relaxation time (T_1) and the transverse relaxation time (T_2). The ^{1}H T_1 in water is determined by interaction fluctuations induced by molecular motions characterized by a correlation time τ. Assuming that the intramolecular proton-proton dipolar interaction of water molecules dominates the relaxation process , T_1 is given by [26]:

$$\left(\frac{1}{T_1}\right)=\frac{3\gamma^4\hbar^2}{10r^6}\left(\frac{\tau}{1+\omega_0^2\tau^2}+\frac{4\tau}{1+4\omega_0^2\tau^2}\right) \tag{2.3}$$

where γ is the gyromagnetic ratio of the proton, $2\pi\hbar$ is the Planck constant, r is the distance between the two hydrogen atoms in a water molecule, and $\omega_0/2\pi$ is the Larmor frequency (34 MHz at 0.8 T). A quantitative relation between T_2 and τ can also be established [27]:

$$\left(\frac{1}{T_2}\right)=\frac{3\gamma^4\hbar^2}{20r^6}\left(3\tau+\frac{5\tau}{1+\omega_0^2\tau^2}+\frac{2\tau}{1+4\omega_0^2\tau^2}\right) \tag{2.4}$$

Figure 2.4C plots the theoretical values of T_1 and T_2 versus τ. The measured T_1 values versus pressure at 8.0°C and 18.4°C are shown in Figure 2.4A. The T_1 at 8.0°C is shorter than that at 18.4°C at the same relative pressure until the saturated pressure is reached, where T_1 values at both temperatures converge to the same value. At 8.0°C, T_1 decreases slowly with increasing pressure up to P/P_0=1.0. At 18.4°C, however, T_1 decreases slowly with increasing pressure below P/P_0=0.8 but decreases rapidly with pressure above P/P_0=0.8.

Similarly, at 8.0°C, T_2 (Figure 2.4B) increases slowly with pressure up to P/P_0=1.0 whereas at 18.4°C, T_2 increases very slowly below P/P_0=0.8 but increases sharply above P/P_0=0.8. T_2 is longer at 8.0°C than at 18.4°C at low relative pressure and becomes comparable at saturated pressure. This measurement reveals that T_2 is much shorter than T_1. Also, T_2 increases while T_1 decreases with either increasing relative pressure or decreasing temperature. Thus, the measured T_1 values are situated to the right of the T_1 minimum (slow-motion limit) as illustrated in Figure 2.4C by the data at P/P_0=0.75. The measured T_2 values at P/P_0=0.75 are shorter than theoretical predictions, as plotted in Figure 2.4C. The theoretical prediction of T_2 considers only the intramolecular dipolar interaction and underestimates the relaxation rate $1/T_2$, which also depends on the intermolecular dipolar interactions. The molecular motions under confinement are anisotropic and the intermolecular dipolar interaction cannot be easily be averaged to zero [28, 29].

The correlation time changes from 132 ns when T_1 is 7 ms (18.4°C, P/P_0=0.75), to 46 ns when T_1 is 3 ms (8.0°C, P/P_0=0.75). These values are several orders of magnitude longer than the 3.5 ps of bulk water at 20°C (on the left edge of Figure 2.4C). The correlation time at 8.0°C is shorter than that at 18.4°C at low relative pressure, and the amount of adsorbed water at a given relative pressure below P/P_0=0.9 is different at these two temperatures. The structure and density of adsorbed water are also expected to be different and could lead to the observed difference in the correlation time. The correlation times at these two temperatures did become the same at P/P_0=1.0 (26 ns) where the amount of water became comparable. This suggests that the structure is similar at these two temperatures when the SWNTs are filled with water.

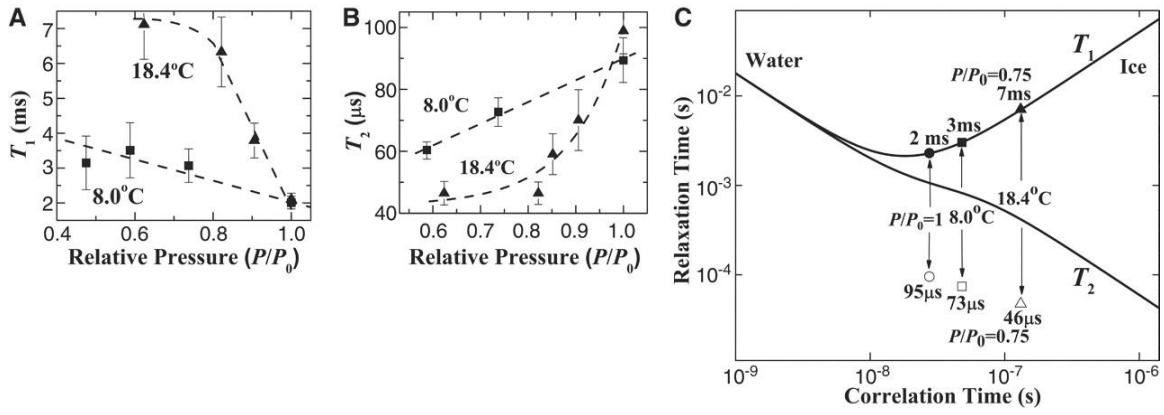

Figure 2.4 Relaxation time of confined water. The measured T_1 (A) and T_2 (B) values versus relative pressure at 8.0°C (squares) and 18.4°C (triangles) are shown. The theoretical values of T_1 and T_2 based on the intramolecular dipolar interaction are shown in (C). Based on the measured T_1 values at P/P_0=0.75, 7 ms at 18.4°C and 3 ms at 8.0°C, the corresponding correlation times of 132 and 46 ns, respectively, are identified. The corresponding T_2 values are shorter than the theoretically expected values for reasons explained in the text. The correlation times at these two temperatures become the same at P/P_0=1 (26 ns).

Because the intramolecular dipolar interaction dominates the spin-lattice relaxation, the long correlation time τ suggests there is a substantial slowdown in molecular reorientation. The slowdown of certain dynamics of water in proximity to small hydrophobic groups has been shown previously [30]. Here I show a similar slowdown of water reorientation in proximity to an extended nonpolar surface.

2.4 Conclusion

Although the hydrophobic effect is widely known to be temperature dependent, our observation demonstrates that such temperature dependence could cause a qualitative change, as manifested by the hydrophobic-hydrophilic transition. At lower temperature, a well-defined layered structure of nanoconfined water on hydrophobic surfaces leads to a narrower probability distribution of the binding energy, making adsorption favorable in terms of the

free energy. When such an ordered structure is weakened at higher temperature, the distribution of the binding energy broadens, making adsorption unfavorable.

The hydrophobicity should not be considered as an absolute property of a surface under nanoconfinement without considering the structure of interfacial water. The correlation time of water reorientation in SWNTs is determined to be on the order of 10 to 100 nanoseconds. This result shows that the dynamics of water reorientation is hindered compared to bulk water, consistent with the dynamics of water molecules in proximity to small hydrophobic groups [30]. Confined and interfacial water are prevalent in biological systems, such as the water in ion channels and in proximity to proteins. The affinity change due to the temperature-induced structural change of water could be relevant to various phenomena including in biological systems, such as the cold denaturation of proteins [2].

2.5 Acknowledgements

This work was supported by NSF under contract DMR 0513915. I thank O. Zhou for help in SWNTs synthesis.

2.6 References

[1] D. Chandler, Nature **437**, 640 (2005).

[2] C. J. Tsai, J. V. Maizel, and R. Nussinov, Crit. Rev. Biochem. Mol. Biol. **37**, 55 (2002).

[3] G. Hummer, J. C. Rasaiah, and J. P. Noworyta, Nature **414**, 188 (2001).

[4] K. Koga *et al.*, Physica A **314**, 462 (2002).

[5] R. J. Mashl *et al.*, Nano Lett. **3**, 589 (2003).

[6] A. I. Kolesnikov *et al.*, Phys. Rev. Lett. **93**, 035503 (2004).

[7] Y. Maniwa *et al.*, Chem. Phys. Lett. **401**, 534 (2005).

[8] A. Striolo *et al.*, Adsorption **11**, 397 (2005).

[9] J. K. Holt *et al.*, Science **312**, 1034 (2006).

[10] S. H. Mao, A. Kleinhammes, and Y. Wu, Chem. Phys. Lett. **421**, 513 (2006).

[11] M. Lagi *et al.*, J. Phys. Chem. B **112**, 1571 (2008).

[12] R. S. Vartapetyan, and A. M. Voloshchuk, Usp. Khim. **64**, 1055 (1995).

[13] T. Ohba, H. Kanoh, and K. Kaneko, J. Am. Chem. Soc. **126**, 1560 (2004).

[14] X. P. Tang *et al.*, Science **288**, 492 (2000).

[15] A. Kleinhammes *et al.*, Phys. Rev. B **68**, 075418 (2003).

[16] H. Z. Geng *et al.*, Chem. Phys. Lett. **399**, 109 (2004).

[17] Y. Maniwa *et al.*, Nat. Mater. **6**, 135 (2007).

[18] S. J. Gregg, and K. S. W. Sing, *Adsorption, Surface Area, and Porosity* (Academic Press, London, New York, 1982), pp. 228.

[19] J. Pires *et al.*, Adsorption **9**, 303 (2003).

[20] T. R. Jensen *et al.*, Phys. Rev. Lett. **90**, 086101 (2003).

[21] O. Byl *et al.*, J. Am. Chem. Soc. **128**, 12090 (2006).

[22] D. Beaglehole, and H. K. Christenson, J. Phys. Chem. **96**, 3395 (1992).

[23] G. R. Birkett, and D. D. Do, J Phys. Chem. C **111**, 5735 (2007).

[24] T. Kurita, S. Okada, and A. Oshiyama, Phys. Rev. B **75**, 205424 (2007).

[25] D. Takaiwa *et al.*, Proc. Natl. Acad. Sci. USA **105**, 39 (2008).

[26] A. Abragam, *The Principles of Nuclear Magnetism* (Clarendon Press, Oxford, 1961).

[27] R. Kubo, and K. Tomita, J. Physical Soc. Japan **9**, 888 (1954).

[28] J. P. Korb, S. Xu, and J. Jonas, J. Chem. Phys. **98**, 2411 (1993).

[29] J. Baugh *et al.*, Science **294**, 1505 (2001).

[30] Y. L. A. Rezus, and H. J. Bakker, Phys. Rev. Lett. **99**, 148301 (2007).

CHAPTER 3

BULK-LIKE PROPERTIES OF WATER IN NANOSCOPIC CONFINEMENT

3.1 Introduction

In CHAPTER 2, I discussed the unique properties of water confined in SWNTs of 1.4 nm in diameter [1]. SWNTs represent one kind of nanoscopic tubular structures for nanoconfined water [2, 3]. Both the geometrical constraints imposed by SWNTs and the surface chemistry of the confining surfaces may affect the structure, dynamics, and thermodynamics of the nanoconfined water [4-7]. For instance, at room temperature, water can assume a layered structure between extended hydrophobic plates with a separation of ~1 nm [8]. It is an obvious question to ask how nanoconfined water behaves in different geometries and different surface chemistry. In this chapter, I will discuss the properties of water confined in slit-shaped pores at the nanoscale.

The interfacial water on a hydrophobic surface experiences a large interaction difference between the water-water interaction and the water-surface interaction. Due to this interaction difference, water confined between two hydrophobic surfaces differs more significantly from the bulk than when confined between two hydrophilic surfaces [8]. As the confining dimensions approach the molecular level, confinement can alter the local molecular arrangement of the water [3]. This local effect can extend to macroscopic phenomena due to the cooperativity of confined molecules. For instance, narrow carbon

nanotubes can align the dipoles of the water molecule chains to a length of ~0.1 mm with a persistence time of ~0.1s [9]. Another example includes the capillary phenomenon, in which the height of water between two parallel hydrophilic plates dipped into water raises to a greater height than the water outside (see Figure 3.1A) [10]. The stronger solid-liquid interaction creates a curved liquid-vapor interface between the two plates. Such a curvature reduces the liquid pressure in the proximity of the liquid-vapor interface and pushes the interface higher than the water outside, with the height inversely proportional to the separation of two plates ($h \propto d^{-1}$). It remains an open question whether such phenomena and theory will persist as the separation decreases from a macroscopic length to a molecular level, up to the point just before they make contact and the water is squeezed out. The key for such phenomena is that the liquid pressure (p_L) is reduced at the solid-liquid-vapor interface. Such liquid pressure (p_L) is equivalent to the vapor pressure (p_V) at which the liquid-vapor equilibrium appears in wettable nanopores through the capillary condensation. In this chapter, I provide experimental evidence that water confined in wettable micropores demonstrates properties similar to those of bulk water, including molecular reorientation and capillary condensation.

Water in different phases is characterized by different molecular dynamics and thermodynamics. The former can be evaluated by nuclear magnetic resonance (NMR) through the spin-lattice relaxation time (T_1), a characteristic time which indicates how fast the Zeeman energy of the nuclear spins can be transferred into the thermal energy. In water, T_1 is largely determined by the reorientational fluctuation of its intramolecular protons [11]. Water adsorption isotherms can reveal the distribution of the chemical potential of adsorbed water in equilibrium with its vapor. It is therefore convenient to measure water adsorption

isotherms by NMR to obtain molecular dynamics and thermodynamics at the same time. Here, I measured water adsorption isotherms in a series of microporous activated carbons with pore sizes ranging from 1.2 to 2.4 nm using an NMR probe connected to an *in situ* water and gas loading system at room temperature [1, 12, 13]. During such adsorption, the T_1 of water increases from ~100 ms to ~1 s, the latter of which is close to that of bulk water (~3 s). These isotherms showed signatures of capillary condensation [14]. The condensation occurs at higher vapor pressure in larger pores, following a similar relation to that described by the Kelvin equation. These results suggest that water starts behaving like bulk water when confined in pores as narrow as 1.2 nm, in terms of molecular dynamics and thermodynamics. Such a method could be extended for characterization of pore size distribution in a series of microporous materials [15].

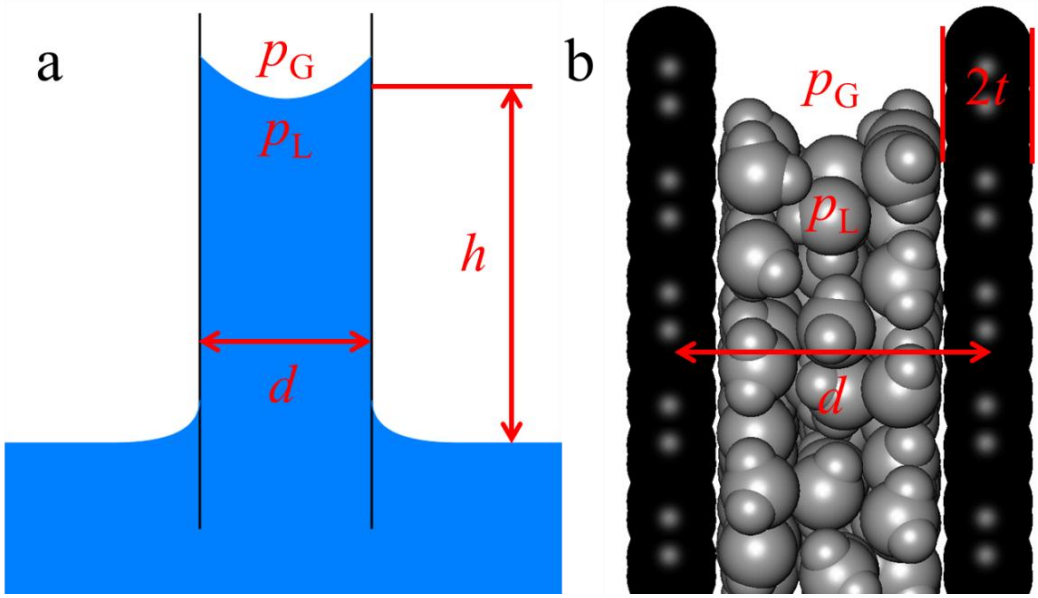

Figure 3.1 Illustrations of (a) capillary phenomena at macroscopic scale and (b) capillary condensation at microscopic scale.

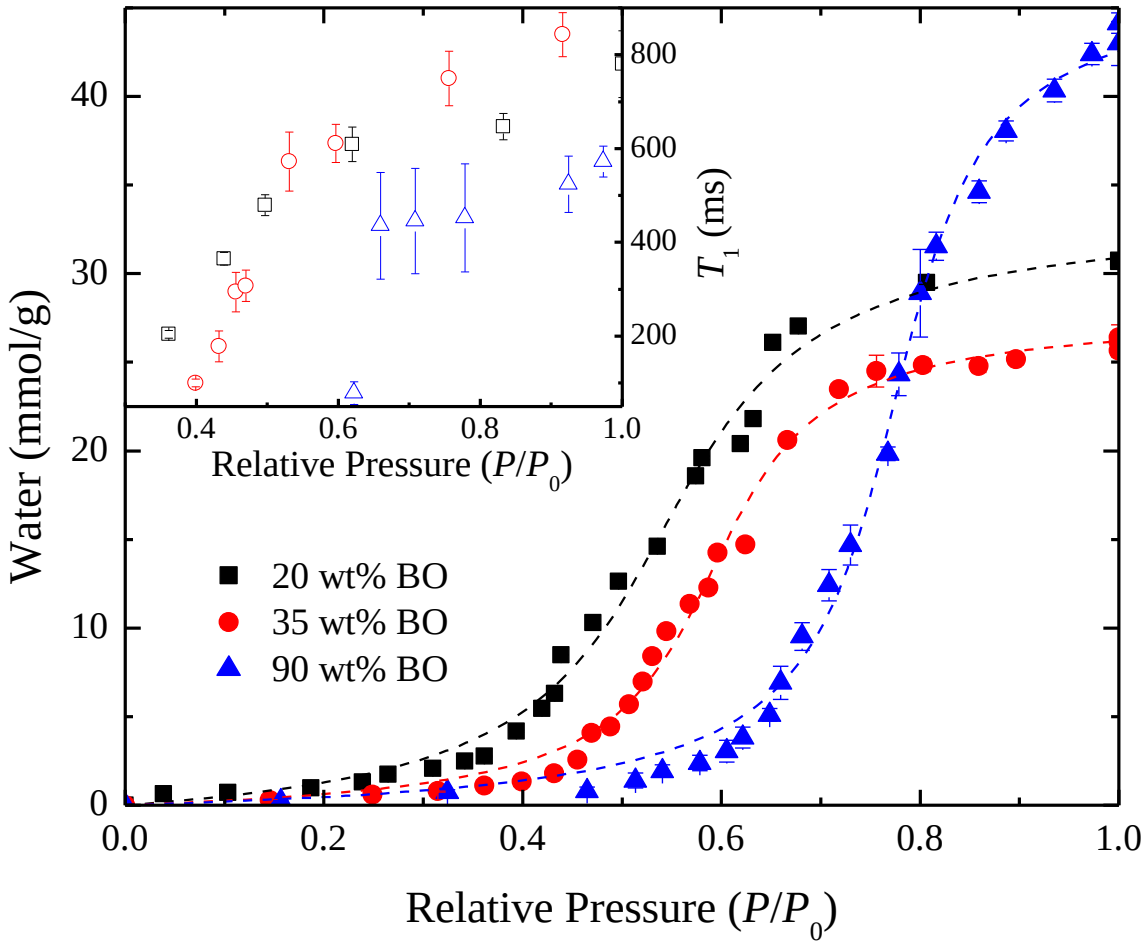

Figure 3.2 Water adsorption isotherms in three microporous activated carbons derived from PEEK with different amount of burn-offs at room temperature. Isotherms are fitted to Eq. (3.1), with fitting parameters shown in Table I. The inset shows the water spin-lattice relaxation time at different relative pressure.

3.2 Experiments

Three activated carbons are derived from a Poly(etheretherketone), or PEEK, precursor by first carbonization in Ar and then activated in steam at 900°C with the amounts of burn-offs (BO) of 20, 35, 90 wt%. Such samples contain slit-shaped micropores of 1.2, 1.4, and 2.4 nm in size, respectively, as characterized in detail elsewhere [16, 17]. Water adsorption isotherms in three samples were measured by ^{1}H NMR at ~0.8 T (^{1}H NMR frequency of 34 MHz) at room temperature (~291 K). The free induction decay was excited

by a solid echo with a π/2 pulse of ~4 μs. The spin-relaxation time was measured by the standard saturation recovery methods. The intensities of the ^{1}H NMR signals were calibrated with a test tube of bulk water of known volume (0.11 cm^3) with corrections for Gaussian decay [11].

3.3 Results and Discussion

Figure 2 shows water adsorption isotherms in three samples, plotted as the amount of water uptake (mmol of water per gram of activated PEEK) versus the relative water vapor pressure (P/P_0, where P_0 is the saturation vapor pressure) at room temperature. The isotherms exhibit a similar S shape as characterized by the Type V isotherm: a small amount of water is adsorbed on the surface functional groups as the primary adsorption sites (PAS) at $P/P_0<0.5$ followed by a steep increase at $0.5<P/P_0<0.7$ and a saturation in water uptake at $P/P_0>0.7$ as a clear signature of capillary condensation [18, 19].

3.3.1 Binary adsorption isotherms of H_2 and D_2O

Water and high-pressure H_2 adsorption isotherms suggest that the capillary condensation of water occurs in the same micropores as that of H_2 does. The binary adsorption isotherms of H_2 and D_2O (Cambridge Isotope, purity 99.9%) in the 35 wt% burn-off sample at room temperature were measured by ^{1}H NMR at ~4.7T (^{1}H NMR frequency of 200 MHz). A single pulse of ~10 μs (a π/2 pulse) was used for excitation. The *in situ* gas loading system is capable of H_2 pressure up to 100 atm [16]. The sample with 35 wt% burn-off was allowed to reach equilibrium with a certain vapor pressure of D_2O before measuring the adsorption isotherm of H_2 up to ~100 atm at room temperature. Figure 3.3(a) shows the ^{1}H NMR spectra of H_2 with various amounts of preadsorbed D_2O. The upfield peaks have been assigned to H_2 in narrow pores (d~1.4 nm) [16]. The intensity of this peak decreases

with increasing amounts of preadsorbed D_2O. Figure 3.3(b) plots the fractional intensity of the upfield peaks, θ_{H_2}, relative to the intensity of the peak at 100 atm with no preadsorbed D_2O, versus the pressure of H_2 and the relative pressure of D_2O. For comparison, the reversed water adsorption isotherm ($1-\theta_{H_2O}$ versus P/P_0) in the same sample is plotted on the plane corresponding to the H_2 pressure of 100 atm. A good correlation between the increase of D_2O and the decrease of H_2 suggests D_2O residues in the same pores as H_2 does. The small error here could be due to error in measuring the water vapor pressure in a much larger stainless steel system.

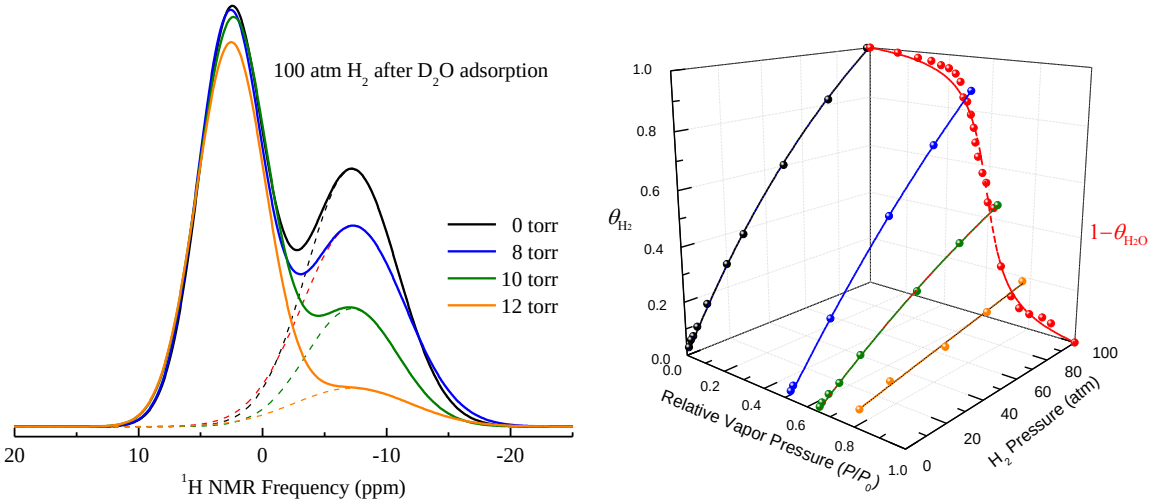

Figure 3.3 (a) ^1H NMR spectra of H_2 at the pressure of 100 atm with different amounts of preadsorbed D_2O in the sample with 35 wt% burn-off. (b) The binary isotherms with H2 and D_2O based on the peak intensity of upfield peak in H_2 spectra. Water adsorption in the same sample is duplicated on the plane of H_2 pressure of 100 atm.

The inset of Figure 3.2 shows T_1 changing from ~100 ms before capillary condensation to ~1s after saturation in all three samples. Such a dramatic change is consistent with the capillary condensation and low density of PAS: T_1 of water is dominated by PAS at low relative pressure; after capillary condensation, water shows a similar T_1 to that of bulk

water (~3s). These are very different from the case of water in SWNTs of 1.4 nm in diameter where the T_1 are much shorter and depends little on the change of relative pressure [1, 12, 13]. Such long T_1 has not been observed by previous NMR measurements of adsorbed water in activated carbons, where surface relaxation centers of PAS dominate the T_1 [20]. This suggests the water, even confined in nanoscopic pores, could have similar molecular reorientation as bulk water, reflected by the spin lattice relaxation mechanism [11].

3.3.2 Water adsorption in activated carbons

The mechanism of water adsorption in activated carbons is a current issue of debate [21-23]. It is generally accepted that the amount and adsorption energy of PAS and the pore size distribution are two primary factors [15, 18, 24]. Water is primarily adsorbed on PAS at low relative pressure (P/P_0<0.5). If the surface density of PAS is high, water is able to cover the surface and fill the pores continuously through the adsorption on PAS as the relative pressure increases. If the surface density of PAS is low, the collapse of water clusters near neighboring PAS leads to capillary condensation. Capillary condensation is indicated by a steep increase of water uptake around P/P_0=0.5 in the isotherm. The pore size then starts playing an important role in determining the relative pressure when capillary condensation occurs [15]. Previous studies of water adsorption in various forms of activated carbons suggest that different carbonization and activation processes will lead to different amounts of PAS and different pore size distributions [18, 19]. Larger pore sizes are usually associated with a higher density of PAS. Continuous adsorption on PAS will obscure the steep increase in water uptake and the effect of pore size on capillary condensation [18]. The uniqueness of activated carbons derived from PEEK is that as the activation time increases, the pore size

increases but the PAS remains at low density. Such a low density of PAS is crucial to explore the effect of pore size on capillary condensation.

3.3.3 Mahle's isotherm

Low water uptake at P/P_0<0.5 suggests a small amount of PAS. As the vapor pressure increases, the isotherm increases within a narrow range of pressure and then bend towards high relative pressure. This is the signature of capillary condensation. It suggests that the pores are filled with water and activated carbons are wettable due to the cooperativity of water [25]. The capillary condensation occurs at a higher relative pressure in the sample with higher burn-off. Characterizations of the pore size by N_2 and H_2 adsorption have shown that a higher burn-off corresponds to a larger pore size of a few nanometers as listed in Table 3.1 [16, 17]. This indicates that the pore size (d) is the dominating factor in capillary condensation. The measured symmetric S-shaped isotherm represents a distribution of condensation pressures with a Lorentzian distribution. It can be fitted into the isotherms provided by Mahle as expressed in the amount of adsorbed water versus relative pressure (P/P_0) via [15]:

$$n = \frac{n_s}{D} \cdot \left[\tan^{-1}\left(\frac{P/P_0 - A}{B} \right) - \tan^{-1}\left(\frac{-A}{B} \right) \right] \qquad (3.1)$$

where n and n_s are the number of adsorbed water molecules at P and P_0, respectively, A and B , expressed in units of P/P_0, are related to the center and the distribution of the condensation pressures respectively, and the normalization coefficient D is given by $D = \tan^{-1}\left[(1-A)/B \right] - \tan^{-1}\left(-A/B \right)$. The fitting parameters are listed in Table 3.1.

Table 3.1 Parameters characterizing three activated carbons derived from PEEK. *A*, *B*, and n_s/D are used to fit the water adsorption isotherms to Eq. (3.1). The pore size and BET surface area are determined in ref [16, 17].

Burn-off (wt %)	*A* (P/P_0)	*B* (P/P_0)	n_s/D (mmol/g)	$n_s \cdot V_L$ (cm^3/g)	*d* (nm)	Surface Area (m^2/g)
20	0.543±0.006	0.112±0.008	11.4±0.2	0.55	1.2	1294
35	0.592±0.005	0.080±0.006	9.3±0.2	0.47	1.4	981
90	0.775±0.003	0.067±0.004	15.3±0.3	0.79	2.4	2802

3.3.4 Pore size distribution

The relation between the center value of the condensation pressure (*A*) and the pore size (*d*) is shown in Figure 3.4 by plotting *d* (nm) vs. $-1/\ln(P/P_0)$. A simple linear fitting gives

$$d = -0.52/\ln(P/P_0) + 0.38 \tag{3.2}$$

Such a relationship allows us to convert the water adsorption isotherms into pore size distributions via [15]

$$\frac{\Delta V}{\Delta d} = -\left\{ BD\left[\left(\frac{P/P_0 - A}{B}\right)^2 + 1\right]\right\}^{-1} \cdot \frac{n_s \cdot V_L}{d - 0.38} \cdot (P/P_0) \cdot \ln(P/P_0) \tag{3.3}$$

where V_L is the molar volume of the liquid water. Despite the fact that the molar volume of water within nanoconfinement may be different from its bulk value, it should remain as a constant close to $18\ cm^3/mol$ as I have used here [8]. Such pore size distributions are shown by solid symbols in the inset of Figure 3.4. They demonstrate the major characteristics of differential pore volume determined from N_2 adsorption of the same materials, as shown by

open symbols in the inset of Figure 3.4 [15-17]. The difference in details could be due to the different adsorption mechanism of water at room temperature and that of N_2 at 77K [19]. In the micropores region, the description of adsorbate density becomes a discontinuous function. This introduces the defects in the density functional theory analysis of N_2 adsorption isotherms [26]. The limitation of the current method is that only a single Lorentzian distribution is assumed for the condensation pressure [15]. Thus only the major component of pore volume could be extracted from the adsorption isotherm. Nevertheless, this result validates Eq.(3.2) by several individual samples and independent measurements.

Equation (3.2) reveals the relation between the relative vapor pressure and the pore size. It follows a similar form to the Kelvin equation [15, 19]:

$$r_m = -2\gamma V_L / RT \ln\left(P / P_0\right) = -2\gamma_\infty V_L / RT \ln\left(P / P_0\right) + 2\delta = -1.07 / \ln\left(P / P_0\right) + 2\delta \quad (3.4)$$

where r_m is the mean radius of curvature of the meniscus (nm), R the gas constant, T the temperature, and γ the surface tension [15, 19]. The variation of the surface tension with the curvature is given by the approximation $\gamma = \gamma_\infty / \left(1 - 2\delta / r_m\right)$, where $\gamma_\infty = 71.97$ mJ/m^2 is the planar limit at 25 °C, δ is the separation between the surface of tension and the equimolar surface [10]. For N_2 adsorption in mesopores where the Kelvin equation is known to be valid, the pore size is related to the radius of the equimolar surface by $d = \cos\theta \cdot r_m + 2t$, where θ is an effective contact angle and t is the thickness of the adsorbed film. [18, 19]. For water, the Kelvin equation is believed to be valid down to 9 nm [27]. The reason why the macroscopic theory of Kelvin equation fails in micropores is that extremely small areas make the surface tension and local density deviate from the bulk and planar values [19]. Water confined between two surfaces with a separation of nanometer scale also lacks a sharp interface

separating the liquid and vapor at molecular scale, making even the definition of the surface difficult [10]. Despite the questionable validity of the Kelvin equation on the nanoscale, it is still intriguing to obtain a coefficient that seems to be the cosine of the contact angle, $0.52/1.07=\cos(61°)$, by comparing Eq.(3.2) and (3.4). Since the Kelvin equation considers only the liquid-vapor interface, a correction from the center of the surface atoms to the contact line should be added as shown in Figure 3.1(b) [28]. This can be approximated by the Lennard-Jones potential parameter $\sigma_{ss}=2t=0.36$ nm of the carbon-carbon interaction [18]. This agrees well with the intercept of Eq.(3.2), $2\delta\cos\theta+2t=0.38$ nm. δ is a small value suggesting the surface of tension and the equimolar surface are very close to each other [10].

The similarity of Eq.(3.2) and (3.4) suggests that at least the underlying principle of the Kelvin equation remains valid for water confined in pores of 1.2~2.4 nm. The solid-liquid and solid-vapor interactions determine the boundary conditions of the liquid-vapor interface. In macroscopic scales, this leads to the curvature of the liquid-vapor interface and a contact angle. Such definitions may be difficult on the nanoscale. The physical meaning of $\cos\theta$ resides no longer in a geometrical factor such as the contact angle. Instead, such a coefficient should be intended to characterize the solid-liquid-vapor interaction and the magnitude of the reduced liquid pressure. The reduced liquid pressure is estimated to be $p_{\mathrm{L}}=p_{\mathrm{V}}-2\gamma\cos\theta/(d-0.38)\approx -0.085$ GPa, from the parameters obtained in the 20 wt% burn-off sample.

The reduced liquid pressure p_{L} represents the ability of corresponding pores to absorb water. Such phenomena could have a wide range of application in engineering and biology. For instance, the capillary phenomenon is among several mechanisms used by the

tree to deliver water from the ground to the tree tops. The limit of the tree height is found to be ~120 m tall on the earth [29]. If assuming the capillary phenomenon is the only limit for the tree height, the corresponding biological capillary is ~0.1 μm in diameter. The reduced pressure $p_{\mathrm{L}} \approx -0.085\,\mathrm{GPa}$ obtained in the 20 wt% burn-off sample could hold a water column with a height of 8.7 km. This shows the significant effect of the capillary phenomenon at the nanoscale.

3.4 Conclusion

In conclusion, the water adsorbed within nanoscopic pores of microporous activated carbons shows properties that are similar to those of water in its bulk phase, including molecular reorientation and capillary condensation. The dynamics of water as indicated by T_1 change dramatically upon the capillary condensation and reach a value that is close to that of bulk water [11, 30]. The capillary condensation occurs at a vapor pressure that can be accurately estimated by the Kelvin equation. This result suggests that water starts to exhibit bulk properties with thickness as thin as three molecular layers in a pore size 1.2 nm. Therefore, water adsorption measurements could be used effectively as a tool for characterizing pore size distribution on the nanometer scale.

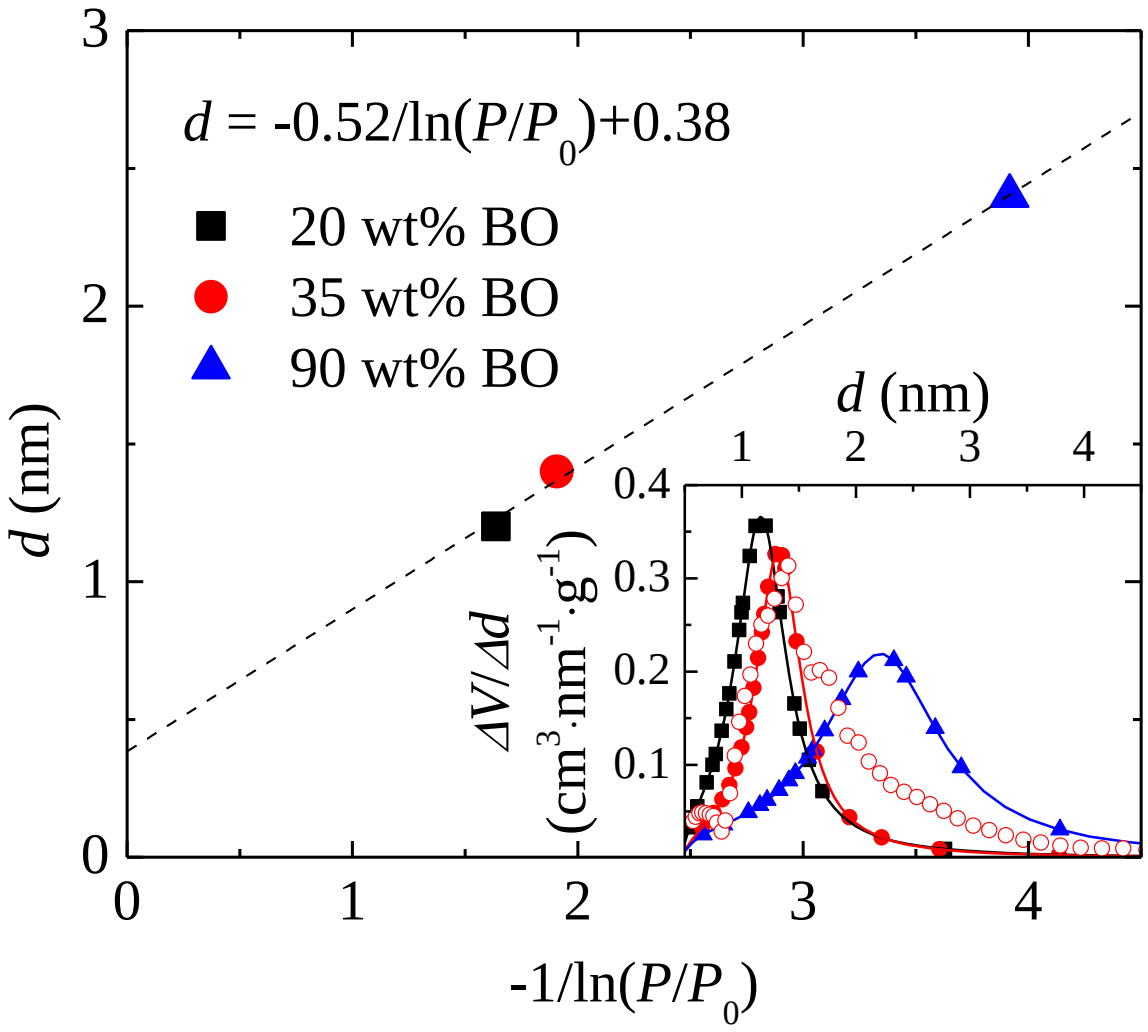

Figure 3.4 Pore size distribution determined from water adsorption isotherms and from the differential pore volume determined from N_2 adsorption at 77k in Ref [17]. The data are converted from the isotherms shown in Figure 3.2. The dashed lines are fitted to Eq. (3.2). The inset shows the correlation of pore size *d* with the condensation pressure characterized by *A*. The data obtained from three samples give a straight line.

3.5 References

[1] H. J. Wang *et al.*, Science **322**, 80 (2008).

[2] K. Koga *et al.*, Nature **412**, 802 (2001).

[3] R. J. Mashl *et al.*, Nano Lett. **3**, 589 (2003).

[4] L. D. Gelb, and et al., Rep. Prog. Phys. **62**, 1573 (1999).

[5] J. K. Holt *et al.*, Science **312**, 1034 (2006).

[6] D. Takaiwa *et al.*, Proc. Natl. Acad. Sci. USA **105**, 39 (2008).

[7] F. Mallamace *et al.*, Proc. Natl. Acad. Sci. USA **105**, 12725 (2008).

[8] N. Giovambattista, P. J. Rossky, and P. G. Debenedetti, Phys. Rev. E **73**, 041604 (2006).

[9] J. Kofinger, G. Hummer, and C. Dellago, Proc. Natl. Acad. Sci. USA **105**, 13218 (2008).

[10] J. S. Rowlinson, and B. Widom, *Molecular theory of capillarity* (Clarendon Press, Oxford, 1982).

[11] A. Abragam, *The Principles of Nuclear Magnetism* (Clarendon Press, Oxford, 1961).

[12] A. Kleinhammes *et al.*, Phys. Rev. B **68**, 075418 (2003).

[13] S. H. Mao, A. Kleinhammes, and Y. Wu, Chem. Phys. Lett. **421**, 513 (2006).

[14] M. E. Schrader, Langmuir **12**, 3728 (1996).

[15] J. J. Mahle, Carbon **40**, 2753 (2002).

[16] R. J. Anderson *et al.*, J. Am. Chem. Soc. **132**, 8618 (2010).

[17] T. P. McNicholas *et al.*, J. Phys. Chem. C **114**, 13902 (2010).

[18] E. A. Muller *et al.*, J. Phys. Chem. **100**, 1189 (1996).

[19] S. J. Gregg, and K. S. W. Sing, *Adsorption, Surface Area, and Porosity* (Academic Press, London, New York, 1982), pp. 228.

[20] G. S. Gogelashvili *et al.*, Colloid Journal **66**, 271 (2004).

[21] R. S. Vartapetyan, and A. M. Voloshchuk, Usp. Khim. **64**, 1055 (1995).

[22] D. Mowla, D. D. Do, and K. Kaneko, in *Chemistry and Physics of Carbon* (Marcel Dekker, New York, 2003), pp. 229.

[23] S. Furmaniak *et al.*, Adv. Colloid Interface Sci. **137**, 82 (2008).

[24] D. D. Do, S. Junpirom, and H. D. Do, Carbon **47**, 1466 (2009).

[25] T. Ohba, H. Kanoh, and K. Kaneko, J. Am. Chem. Soc. **126**, 1560 (2004).

[26] C. M. Lastoskie, and K. E. Gubbins, in *Characterization of Porous Solids V*, edited by K. K. Unger, G. Kreysa, and J. P. Baselt (Elsevier, Amsterdam, 2000), pp. 41.

[27] L. R. Fisher, R. A. Gamble, and J. Middlehurst, Nature **290**, 575 (1981).

[28] M. Kruk, M. Jaroniec, and A. Sayari, Langmuir **13**, 6267 (1997).

[29] G. W. Koch *et al.*, Nature **428**, 851 (2004).

[30] N. Bloembergen, E. M. Purcell, and R. V. Pound, Phys. Rev. **73**, 679 (1948).

CHAPTER 4

TEMPERATURE DEPENDENCE OF LYSOZYME HYDRATION AND THE ROLE OF ELASTIC ENERGY

4.1 Introduction

In CHAPTER 2 and CHAPTER 3, I discussed nanoconfined water in different geometries and surface chemistry. The original motivation to study such water is the important role water plays in the folding, dynamics and functions of proteins. Equipped with my understanding of water developed in previous chapters, I continue to study water at the interface of biomolecules in the following chapters.

The most basic property of hydration—the water sorption isotherm—remains inadequately understood. Surface adsorption is the commonly adopted picture of hydration. However, surface adsorption does not account for changes in the conformational entropy of proteins, with this picture it is difficult to explain why protein dynamics and activity change upon hydration. The solution picture of hydration provides an alternative description of the thermodynamics of hydration. In this model the flexibility of proteins can influence the hydration level as the elastic energy of the protein changes upon hydration. Using nuclear magnetic resonance to measure the isotherms of lysozyme *in situ* between 18 and 2°C, I provides evidence that the part of water uptake associated with the onset of protein function is significantly reduced below 8°C. Quantitative analysis shows that this reduction is directly related to the decrease of protein flexibility and enhanced cost in elastic energy for

accommodating the hydration water at lower temperatures. The elastic property derived from the water isotherm agrees with direct mechanical measurements, providing independent support for the solution model. This result also implies that water adsorption at charged and polar groups occurring at low vapor pressure, which is known to soften the protein, is crucial for the later stage of water uptake. This water uptake leads to the activation of protein dynamics. These results also shed light on the mutual influence of protein flexibility and hydration, providing the basis for understanding the role of hydration in protein dynamics.

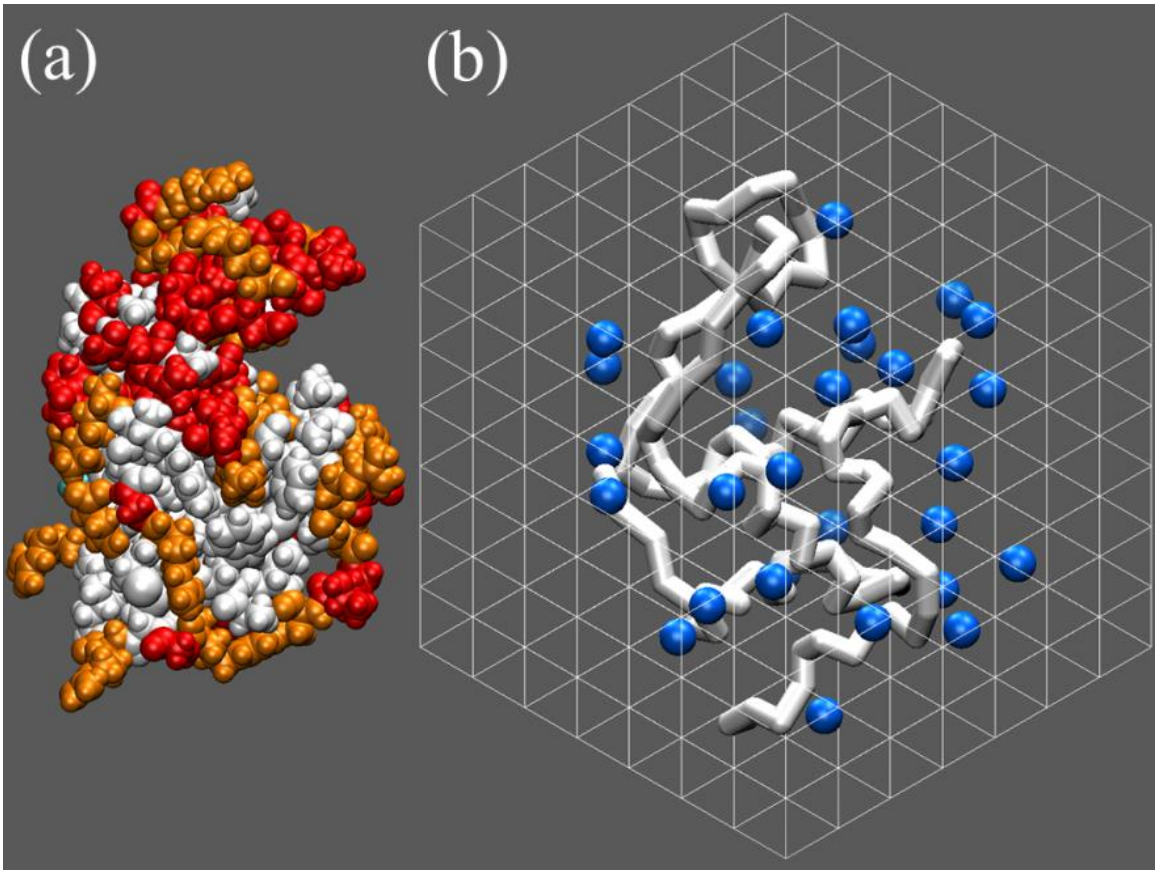

Figure 4.1 (a) A van der Waals representation of a lysozyme molecule colored with a hydrophobic scale: white = hydrophobic, red (dark gray) = hydrophilic, orange (gray) = positive or negative charge. (b) A lattice model of protein hydration. The white chain represents a lysozyme molecule occupying x lattice cells. The blue (gray) spheres are hydration water, each of which occupies one lattice cell. Their locations are obtained from hydration water of less than 0.34 nm away from the protein in molecular dynamics simulations shown in Section 4.3.6.

Hydration plays an important role in protein folding, dynamics, and functions [1-4]. For instance, the enzymatic activity of lysozyme increases significantly above a hydration level of h = 0.2 (in grams of water per gram of dry proteins) [2, 5]. Water-protein interaction has also been a central theme of protein folding ever since Kauzmann introduced the concept of hydrophobic interaction in 1959 [1]. One of the direct ways to probe the characteristics of protein hydration is the water sorption isotherm. Surprisingly, the mechanism governing water sorption isotherms in proteins still remains an issue of debate [2, 6]. The prevailing picture of surface adsorption does not take into account structural and dynamical changes of proteins associated with hydration. The present work provides new experimental evidence indicating that the understanding of water sorption isotherms in the globular protein lysozyme also requires a treatment beyond surface adsorption theory. A deeper understanding of water sorption isotherms in proteins could shed light on the structure, dynamics, and functions of protein [2-10].

The characteristics of water sorption isotherms of globular protein powders are quite universal near room temperature [2, 6, 11, 12]. From dry condition to a relative water vapor pressure P/P_0~0.7 (P_0 is the saturated water vapor pressure at a given temperature), the amount of absorbed water increases gradually with P/P_0, reaching a certain hydration level (h ~0.2 in lysozyme). This initial stage of hydration is identified with water adsorption at ionizable groups, and charged and polar sites, as illustrated in Figure 4.1(a) [2, 11, 13, 14]. Above this pressure, an upswing in water uptake occurs. It has been suggested that this upswing in water uptake correlates with the onset of key protein functions [2, 13]. So far there is no consensus with regard to the mechanism of this upswing in water uptake [2, 6]. The understanding of the nature of this upswing in water uptake is the focus of this work. In

particular, the temperature dependence of this upswing is clearly established at temperatures below 8°C. Although hydration near physiological temperature is of primary concern in biology, the temperature dependence of the isotherm below room temperature provides important clues to the mechanisms of hydration. To our best knowledge, water sorption isotherms over the entire pressure range of P/P_0=0 to 1 have not been reported for protein crystallites down to temperatures near 0°C. This could be due to the inconvenience of using the traditional gravimetric technique for *in situ* hydration measurements over a wide range of vapor pressure and temperature. In this work, water sorption isotherms were measured with an alternative approach based on ^{1}H nuclear magnetic resonance (NMR) [15, 16].

4.2 Experiments

The hen egg white lysozyme (HEWL, catalog no. L-7561, 3× crystallized, dialyzed, and lyophilized) was purchased from Sigma Aldrich and used without further purification. The enzymatic function of lysozyme is strongly affected by the hydration level and the temperature: it increases significantly above a hydration level of h = 0.2 [5]; the activity at 10°C is only about 20% of that at 35°C [17]. The lysozyme was loaded into the quartz NMR sample tube connected to an *in situ* water loading system with controlled vapor pressure and temperature [16]. A single pulse (~5 μs) was used to excite the ^{1}H NMR signals at 0.8 T (34 MHz ^{1}H NMR frequency). The spectrum of as-received lysozyme powder contains two major components: a sharp peak with the FWHM of ~2.4 kHz on top of a broad peak with FWHM of ~40 kHz, as shown in Figure 4.2(a). The sharp peak can be gradually removed by pumping the sample chamber to 10^{-3} torr for 24 hours at room temperature. The broad peak remains unchanged during the pumping procedure and was assigned to proton background solely from lysozyme molecules [12]. After the initial pumping, a constant water vapor

pressure was kept in the sample chamber at each step to rehydrate the lysozyme. The intensity of the NMR signal reaches equilibrium within 2~3 hours, much faster than the isopiestic method that is slowed down by the air environment [18]. No further change in NMR signal was observed after 3 hours as verified by continued monitoring over a time period of 2 days. The sharp peak reappears in the rehydration process and is assigned to water sorption in the protein [12]. Since the protons account for about 6.8% weight of a lysozyme molecule [19], the hydration level *h* can be calculated from the intensity ratio of the sharp and broad peaks of the NMR spectra at equilibrium. Since the NMR signal is very stable and accurate, the major systematic error comes from the conversion from the intensity ratio of broad and narrow peak into the hydration level. The effect of the detection delay (~8 μs) on the fast decay component of the free-induction-decay, corresponding to the broad peak in the spectra, has to be considered. Based on a Gaussian decay, I can extrapolate it back to the end of the excitation pulse [20]. The extrapolation leads to a systematic error of ~5% to the conversion coefficient. The similarity of the sorption isotherms at 18°C measured by NMR and by other methods confirms that this error is not significant [21]. Such an error only affects the absolute hydration level. Its net effect is similar to stretching or shrinking the hydration axis of the isotherms by ~5%. It has no effect on the relative value for measurements at different temperatures and at different vapor pressures. Thus the shape of the sorption isotherms remains unaffected and the systematic error in the absolute value of the hydration level is insignificant. The isotherms measured by the ^{1}H NMR method were shown to be consistent with those obtained by the traditional gravimetric technique [12].

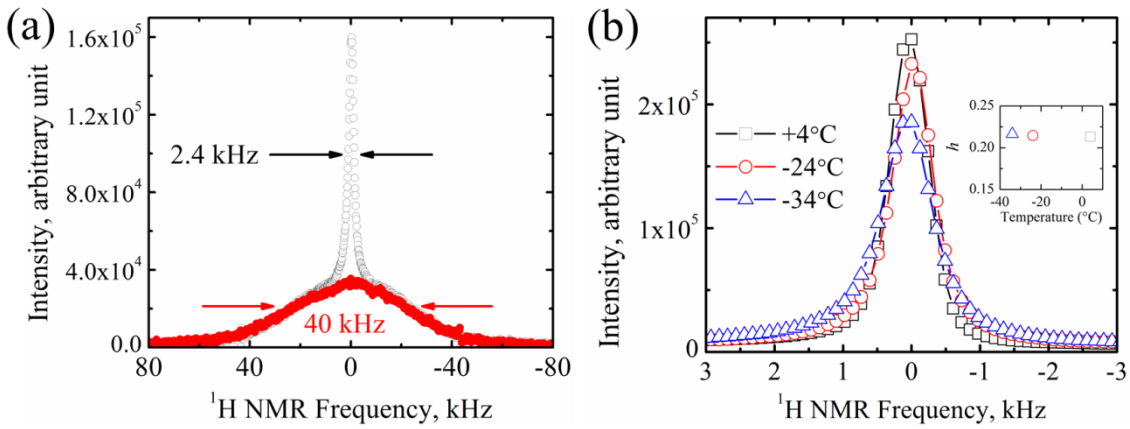

Figure 4.2 (a) NMR spectra of lysozyme powder before (open circle) and after pumping (filled circle). (b) The sharp NMR peak corresponding to the hydration water of protein as the temperature decreases from 4°C to -34°C. The initial hydration level is h~0.21 at 4°C. The inset shows the hydration levels estimated from the integrated intensities of such sharp peaks.

4.3 Results and Discussion

Figure 4.3 shows measured hydration level h versus relative vapor pressure P/P_0 in lysozyme at temperatures of 18°C, 8°C, 4°C, and 2°C. These isotherms share a common sigmoidal feature as type II isotherms [22]. The isotherms at low relative pressure (P/P_0 < 0.7) depend linearly on P/P_0 with small changes in slope below 8°C. The adsorbed water in this part of the isotherm has been correlated with the charged and polar groups in proteins based on *in situ* IR measurements [11, 13]. Above P/P_0 = 0.7, the measured isotherms depend strongly on temperatures over a small range of temperature from 18°C to 2°C. This dependence has not been established by earlier studies [2, 6].

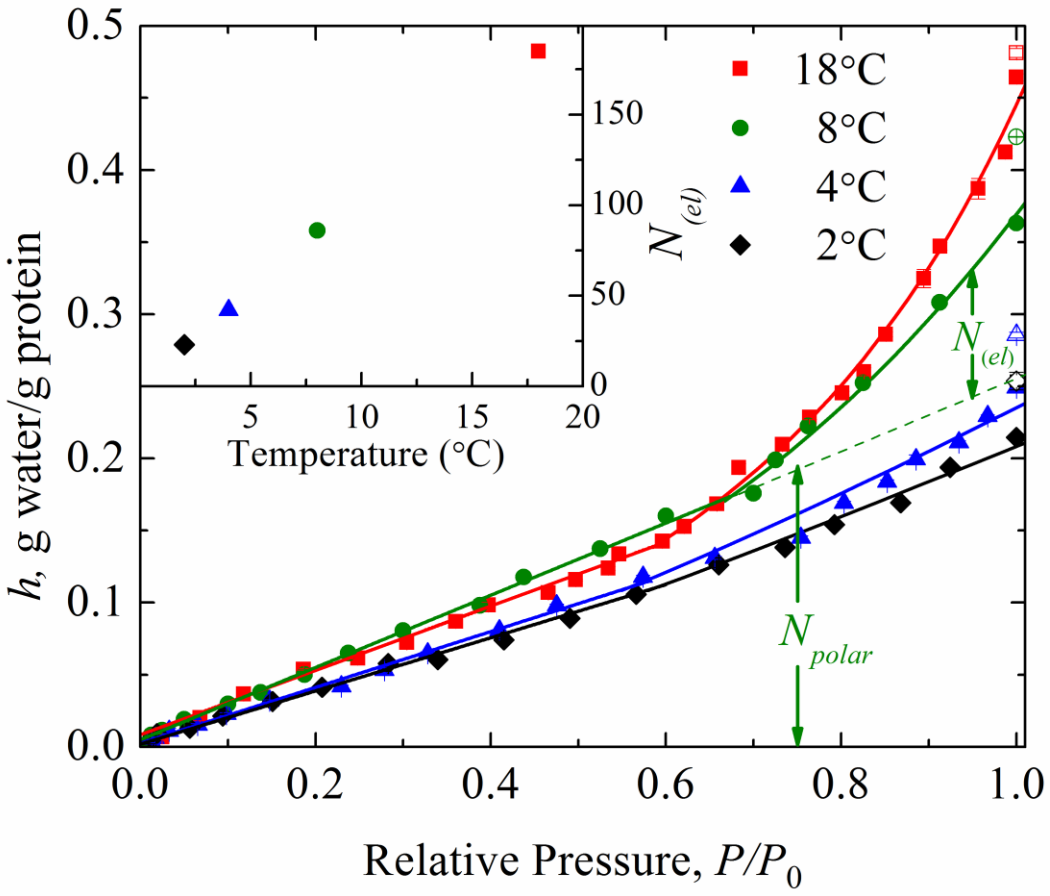

Figure 4.3 Water sorption isotherms in lysozyme powder from 18°C to 2°C. The isotherms at high relative pressure are fitted as the implicit form of Eq. (4.2) with parameters shown in Table 4.1. The inset plots $N_{(el)}^{0}$ versus temperature.

There is a seemingly dramatic change between the isotherms at 8°C and 4°C. This is caused by the difference in water uptake of the charged and polar groups at low relative pressure. The portion of the hydration water related to the upswing actually decreases smoothly from 18°C and 2°C, when the number of water molecules adsorbed on polar groups is removed. I will discuss this in Section 4.3.5. As the pressure reaches the saturated vapor pressure, further hydration will cause condensation of bulk water without any increase of pressure. The upper data points at P/P_0 =1, as shown in open symbols, correspond to such

bulk condensation, confirming that I reached saturated vapor pressure at corresponding temperatures.

4.3.1 Surface adsorption picture

The main reason for the lack of isotherm data for low temperatures near 0°C is perhaps the prevailing belief that the isotherms should be largely temperature-independent when plotted versus P/P_0 [6]. In the picture of surface adsorption the upswing in water uptake above P/P_0 ~0.7 is attributed to multilayer formation [6, 11, 23]. The best known surface adsorption theory for describing multilayer formation is the BET theory [22]. The BET isotherm is given by

$$h \propto \frac{(c-1)P/P_0}{1+(c-1)P/P_0} + \frac{P/P_0}{(1-P/P_0)} \qquad (4.1)$$

where $c = \tau / \tau_1$. τ and τ_1 are the residence times of molecules directly bound to the adsorbent surface and adsorbed on top of the first layer, respectively. Inside protein crystals, spatial restrictions would prevent bulk water condensation and adsorption is limited to finite number of layers and can be easily taken into account in the BET theory [22, 23]. Other surface adsorption models give somewhat different expressions for the isotherms but the essence for the description of the upswing in water uptake is very analogous to the standard BET theory [6, 23]. Equation (4.1) shows that the upswing in water uptake, as dominated by the second term, is expected to be temperature-independent when plotted versus the relative pressure P/P_0 [6]. Isotherm data taken above room temperature indeed confirm this expectation [21, 24]. However, this is no longer the case in lysozyme below 10°C. The upswing in water uptake above P/P_0 ~0.7 gradually disappears as the temperature approaches 0°C. Such a

temperature dependence of water sorption isotherms cannot be explained in the framework of surface adsorption [22, 23].

4.3.2 Modified Flory-Huggins theory

It was suggested that the system at the upswing could be treated as a very concentrated solution based on the Flory-Huggins theory [6, 25]. The Flory-Huggins theory describes the mixing of water with protein by a three-dimensional lattice model, where a protein molecule is represented by a chain occupying *x* lattice cells and each water molecule occupies one lattice cell [26]. This model is illustrated in Figure 4.1(b). Upon mixing of N_1 water molecules with N_2 protein molecules, the change of the free energy is given by $\Delta G = \Delta H_m - T\Delta S_m + \Delta H_{(el)}$, where $\Delta H_m = k_B T \chi N_1 N_2 / (N_1 + xN_2)$ is the enthalpy of mixing characterized by the parameter of interaction χ between water and the protein molecule and k_B is the Boltzmann constant. $\Delta S_m = -k_B [N_1 \ln v_1 + N_2 \ln v_2]$ is the entropy of mixing where $v_1 = N_1 / (N_1 + xN_2)$ and $v_2 = xN_2 / (N_1 + xN_2)$ are the volume fractions of water and proteins, respectively. $\Delta H_{(el)} = V \cdot (K/2)\left(v_2^{-1/3} - 1\right)^2$ is the elastic energy, as approximated to the first order, due to the volume expansion upon water addition as given by Rowen and Simha [25], where $V = \overline{V_1}(N_1 + xN_2)$ is the total volume of the N_2 protein molecules mixed with N_1 water molecules and $\overline{V_1}$ is the volume of each lattice cell. *K* is the macroscopic parameter of the elastic modulus of the proteins. Since globular proteins have residues that are compact, the core may not be readily available for mixing with water molecules [27]. This can be taken into account by replacing *x* with ηx in the expressions of ΔH_m and ΔS_m, where $0 \le \eta \le 1$ is the fraction of flexible segments in the protein [28, 29]. This correction is

not necessary in $\Delta H_{(el)}$ since the elastic energy depends on the volume change of the bulk. The equality of the chemical potentials of water in the vapor phase, $\mu_{vapor} = k_B T \ln(P/P_0)$, and in the water-protein mixture leads to [25, 28, 29]

$$\left[\ln(P/P_0) - \eta \ln v_1 - \eta v_2\right] v_2^{-2} = \chi + \frac{K\bar{V}_1}{2k_B T}\left(\frac{1}{v_2^{1/3}} - 1\right)\left(\frac{5}{3v_2^{1/3}} - 1\right) v_2^{-2} \qquad (4.2)$$

Here, the plot of $\left[\ln(P/P_0) - \eta \ln v_1 - \eta v_2\right] v_2^{-2}$ versus $\left(v_2^{-1/3} - 1\right)\left[(5/3)v_2^{-1/3} - 1\right] v_2^{-2}$ is linear with the intercept at χ and the slope containing the elastic modulus *K*, if both parameters are constant within a certain range of relative pressure. Using the partial specific density of water ($\rho_1 = 1.0$ g/cm^3) and lysozyme ($\rho_2 = 1.38$ g/cm^3) [30], v_1 and v_2 can be determined from the hydration level *h* via $v_1 = 1 - v_2$ and $v_2 = 1/(h\rho_2/\rho_1 + 1)$. The exact value of η is unknown. I could examine a wide range of η values and obtain the corresponding elastic modulus *K*.

As pointed out already by Rowen and Simha, $\Delta H_{(el)}$ was estimated to be too small for polymers and proteins at room temperature to have any significant effect on sorption isotherms [25]. This is consistent with the largely temperature-independent water sorption isotherms above room temperature [6]. The key idea of this work is that this situation might change at lower temperature since *K* increases strongly with decreasing temperature. For instance, the Young's modulus of lysozyme increases more than five-fold as the temperature decreases from 53°C to 22°C based on mechanical measurements [31]. The elastic modulus *K* should be similar to Young's modulus if the Poisson's ratio for lysozyme is assumed to be 0.33 [32]. This suggests that the elastic energy could have a significant effect on water sorption isotherms below room temperature. The elastic energy term also provides a unique link between the microscopic mechanism of water sorption and a macroscopic quantity *K*,

which can be compared to values obtained by mechanical measurements. This offers an independent validation of the solution picture of protein hydration.

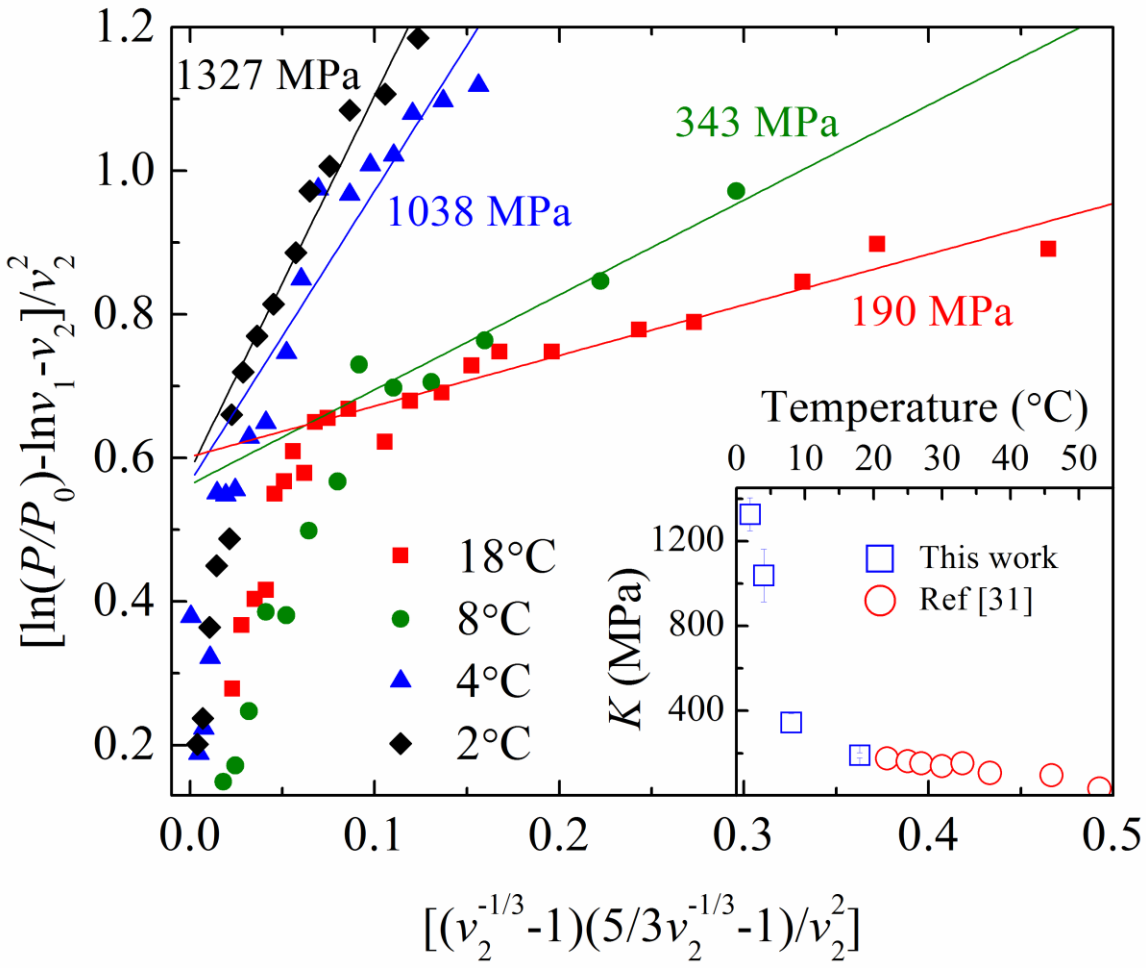

Figure 4.4 Plots of $[\ln(P/P_0)-\ln v_1-v_2]/v_2^2$ versus $[(v_2^{-1/3}-1)(5/3v_2^{-1/3}-1)/v_2^2]$ for the isotherms data following Eq. (4.2). The plots show a linear portion when $[\ln(P/P_0)-\ln v_1-v_2]/v_2^2>0.6$. The fitting parameters are shown in Table 4.1 for η=1. The inset shows the comparison of the temperature dependence of the elastic modulus (red square) derived from isotherms in this study, with the Young's modulus of hydrated lysozyme (red circle) measured in [31].

4.3.3 The elastic constant and its temperature dependence

Figure 4.4 plots the isotherm data following Eq. (2) when $\eta = 1$. All isotherms at temperatures from 18°C to 2°C have a linear portion when $\left[\ln\left(P/P_0\right)-\ln v_1-v_2\right]v_2^{-2}>0.6$,

which corresponds to $P/P_0 > 0.7$. Using 18 cm^3/mol to estimate the water molecule volume $\overline{V}_1$ in Eq. (2), χ and K can both be determined from the linear fits in Figure 4.4. These values are listed in Table I. χ is expected to be a constant at high relative pressure and depends on temperature following $\chi = \beta + \alpha/(RT)$ with α and β being constants and R is the gas constant [25, 26]. With the temperature change from 18°C to 2°C, the change of χ should be less than 4% with typical values of α (-1.1 kJ/mol) and β (1.3) as determined in serum albumin [25]. From Table I, χ values at different temperatures are all close to 0.59 within errors. This is comparable to the value of 0.87 for water-serum albumin system and 0.41 for water-salmine system [25]. The determined elastic modulus K increases from 190 MPa at 18°C to 1326 MPa at 2°C. Although the temperature is in the vicinity of the freezing point of bulk water at 0°C, such a dramatic change of elastic modulus is not due to the crystallization of hydration water. Figure 4.2(b) shows that as the temperature decreases from 4°C to -34°C, the sharp NMR peak corresponding to the nonfrozen hydration water becomes broader. Its integrated intensity, however, remains the same as shown in the inset of Figure 4.2(b). This confirms that the freezing temperature of the protein-water system is reduced well below 0°C [6, 20, 33]. It is intriguing to note that the Young's modulus of the lysozyme tetragonal crystal along the [001] direction determined by mechanical measurements increases from 34 MPa at 53°C to 175 MPa at 22°C, as shown in the inset of Figure 4.4 [31]. Such elastic moduli are shown to be identical to those of amorphous samples [34]. The values of K derived from the isotherms are consistent with those derived from the independent mechanical measurement. This provides strong evidence that water sorption above the upswing in the isotherms should be interpreted using the solution model with explicit consideration of the elastic energy and entropy.

Table 4.1 Fitting parameters (χ and K) and standard errors following Eq. (2), when η=1, 0.5 and 0.25, and the maximum number of water per protein associated with the elastic free energy $N_{(el)}^{0}$, and the total number of hydration water per protein $N_{hydration}^{0}$, at P/P_0=1.

T(°C)	χ	K (MPa)	K (MPa)		$N_{(el)}^{0}$	$N_{hydration}^{0}$
	η=1		η=0.5	η=0.25		
18	0.60±0.01	190±15	353±27	417±35	185	360
8	0.56±0.03	343±45	605±73	709±80	86	299
4	0.57±0.05	1038±137	1628±193	1923±222	42	189
2	0.58±0.03	1327±91	2206±189	2646±241	23	167

For the small globular protein lysozyme, the flexible residues that are involved in the mixing near the surface take up a large portion of the total volume. Thus, it is reasonable to assume that the parameter related to partial flexibility, η, is close to 1. Nevertheless, the elastic modulus K does not depend sensitively on η. As shown in Table I, the extrapolated K remains of the same order of magnitude with η = 1, 0.5 and 0.25. The temperature dependence of K remains similar for a wide range of η. A change of η doesn't affect the conclusion that the temperature dependence of the elastic modulus K of the protein is responsible for the observed temperature dependence of the upswing in water uptake. The purpose of this work is not to use sorption isotherms to measure the elastic modulus quantitatively. Such an agreement on the same order of magnitude is the most I can expected based on the current model. The parameter related to the water-protein interaction, χ, however, depends sensitively on the absolute value of η. The value of χ became uncertain with an unknown η. For this reason, it may be difficult to obtain an exact value for η for much larger proteins such as BSA and hemoglobin.

4.3.4 Protein properties with hydration above $h = 0.2$

In the above analysis, the elastic modulus K is assumed to be a constant above $P/P_0 = 0.7$. This is supported by previous measurements which shows that the Young's modulus decreases significantly at low hydration level but depends only weakly on hydration above $h = 0.2$, which corresponds to $P/P_0 > 0.7$ [34]. This is also consistent with studies of protein dynamics where adsorbed water per protein at charged and polar groups is shown to have a strong influence on protein flexibility, perhaps due to a charge screening effect [2, 5]. Many other protein properties become identical to those in dilute solutions with hydration above $h = 0.2$. The specific volume of dried proteins is 3~7.5% larger than the value in solutions, primarily due to the electrostriction about the charged groups [6, 35]. Such a difference disappears as the hydration level increases to $h = 0.2$ [2, 36]. The protein conformation are shown to be similar in the dry state and in solution to a resolution of ~0.1 nm [2]. A raman study showed that the conformation and flexibility changes only at low water content within $h = 0.1$~0.2 [37]. Above h~0.17, those properties become similar to those in solutions. These facts suggest that, even if there is possible partial unfolding or conformational change during the dehydration or rehydration process, it is reversible and occurs at a hydration level lower than what is needed for the upswing in water uptake [5, 6, 37].

4.3.5 The nature of the upswing in water uptake

Using the linear region in the isotherms (P/P_0<0.7), I can estimate the amount of water adsorbed on charged and polar groups N_{polar} versus P/P_0 as shown in Figure 4.3. Subtracting N_{polar} at P/P_0 from the total number of absorbed water molecules per protein, $N_{hydration}$, the excess water $N_{(el)} = N_{hydration} - N_{polar}$ is obtained as illustrated in Figure 4.3.

According to the modified Flory-Huggins theory, water molecules associated with $N_{(el)}$ are mixed with the protein structure such as side chains and depend on the elastic energy. The temperature dependence of *K* is essential in modulating the ratio of the elastic contribution to the chemical potential. The ratio could be much smaller at higher temperatures, and $\Delta H_{(el)}$ will be too small to have significant effect on hydration [25]. As a result, $N^0_{(el)}$, the maximum of $N_{(el)}$ reached at $P/P_0 = 1$, varies greatly with temperatures. As shown in Table I, it is 185 out of $N^0_{hydration} = 360$ ($N_{hydration}$ at $P/P_0 = 1$) at 18°C, but only 23 out of 167 at 2°C. The inset of Figure 4.3 plots $N^0_{(el)}$ versus temperature. $N^0_{(el)}$ decreases gradually from 18°C to 2°C. It is important to note that simulations based on the surface adsorption model require about 6 layers to produce the upswing in water uptake shown in Figure 4.3 [25]. However, the amount of absorbed water $N^0_{hydration} = 360$ at 18°C is smaller than that contains in this number of monolayers based on the lysozyme structure [2]. Therefore, water molecules associated with $N_{(el)}$ should be considered as incorporated in the protein structure with important consequences for protein structures and dynamics.

4.3.6 Molecular dynamics simulations

The elastic modulus *K* at high hydration level is an averaged macroscopic measure of the microscopically heterogeneous flexibility of the protein and is closely related to structural fluctuations [10, 38-40]. They can be affected significantly by hydration and temperature [31, 34, 41-43]. Therefore the molecular dynamics simulations on lysozyme under partially and fully hydrated proteins may provide useful insights on the mechanism of hydration.

The structure of HEWL has been solved to an exceptionally high resolution of 0.94 Å [14], exhibiting a typical globular protein fold with two main domains: a relatively more stable α-domain consisting of residues 1-39 and 89-129 forming four α-helices (helices A-D) and a 3_{10}-helix, and a relatively more mobile β-domain consisting of residues 40-88 forming three anti-parallel β-strands and another 3_{10}-helix. Figure 4.5 shows a HEWL structure from molecular dynamics simulations. The enzymatic activity site is the cleft between the two domains, where a hexasaccharide can bind with a distortional stress at the fourth sugar, accelerating the cleavage of its glycosidic bond. Residues Glu35 and Asp52 on the opposing faces of the cleft and a water molecule are critically involved in the enzymatic reaction [44].

I performed molecular dynamics (MD) simulations on lysozyme (PDB: 1IEE) [14] using Amber 10.0 [45] with Amber FF99SB force field at constant number of molecules, pressure, and temperature of T = 291 K (18°C). Two systems with different lysozyme hydration conditions were prepared for simulations. The experimentally-determined numbers of hydration water molecules $N_{hydration}$ of 124 and 360 were used for the partially and fully hydrated systems, corresponding to the water vapor pressures of 12 mbar (P/P_0 = 0.6) and 20 mbar (P/P_0 = 1), respectively. Both systems were simulated for 11 ns with a time step of 2 fs. A cut-off of 10 Å was used for the Lennard-Jones interaction. The particle-mesh Ewald method was used for electrostatic interactions. Isotropic position scaling was used to maintain the pressure with a relaxation time of 2 ps. The Langevin dynamics was used to control the temperatures using a collision frequency of 1.0 ps^{-1}. A periodic boundary condition was applied to both systems. The data were saved every 2 ps over the course of the 11-ns simulation. The simulation results were analyzed using AmberTools [45] and visualized using VMD [46].

The MD simulations suggested that an increase in $N_{(el)}$ is associated with an increase in protein fluctuations and correlated motions. The root-mean-square-fluctuation was calculated for both systems using the trajectories over the course of last 5-ns simulations. Lysozyme showed greater flexibility under the fully hydrated condition, under which $N_{(el)}$ increased substantially. In addition, the structures averaged over the last 5 ns simulations were subjected to normal mode analyses using the Gaussian network model (GNM) [47, 48]. As shown in Figure 4.6, the overall level of fluctuation is lower when $N_{hydration}$ = 124 (diagonal intensities in Figure 4.6(a)) than when $N_{hydration}$ = 360 (diagonal intensities in Figure 4.6 (b)). In addition to the elevated mean square fluctuation at individual residues, it is also interesting to note that a high level of hydration greatly increases the correlated motions (off-diagonal intensities in Figure 4.6 (b)) of the β-domain. This is most profound in residues 44-53 and residues 59-81, as shown from the diagonal intensities (in dashed squares) and off-diagonal intensities (in dashed rectangles) in Figure 4.6. Residues 44-53 correspond to the β1 and β2 along with the linker as highlighted in red in Figure 4.5, and are within the upper-left dashed squares in Figure 4.6. Residues 59-81 correspond to the large flexible loop hovering above the activity cleft as highlighted in yellow in Figure 4.5, and are within the lower-right dashed squares in Figure 4.6. A noticeable exception is the absence of long-range correlated motions in residues 54-58 with the rest of the β-domain as shown in orange in Figure 4.5. A close examination of the water distribution in the high-resolution crystal structure suggests that no water molecule can be found within the first hydration layer, which peaks at ~2.7 Å [49], near the segment of residues 54-58. In contrast, at least 23 water molecules can be found in the crystal structure covering the surface of other loops in the β-domain. For lysozyme, the ability for the contour of the long cleft to be flexible is critical for the two-step enzymatic

reaction [44]. The protein dynamics at the loop and hinge regions outside the active site has been found to be crucial to the motion of the two dynamically distinct domains and critical to enzymatic activities [39]. The presence of water molecules is essential to bringing about the modes of protein motion that would be otherwise unrealizable in the absence of water. The increase in protein fluctuations at higher hydration level suggests that hydration promotes protein fluctuations. Protein fluctuations are related to the elastic modulus at high hydration level through the equipartition theorem [10, 40]. The elastic energy could become significant as the elastic modulus increases at lower temperature.

4.4 Conclusion

The current study reveals the strong temperature dependence of the water uptake in lysozyme at high relative pressure below 10°C. Such temperature dependence could be explained by the enhanced cost in the elastic energy upon hydration at lower temperature. The temperature dependence of the elastic modulus K of the protein is responsible for the observed temperature dependence of the upswing in water uptake. Although related to the microscopic flexibility of the protein, the elastic modulus K used in our analysis of elastic energy is a parameter at the level of thermodynamics, not a model-dependent quantity at the molecular level or based on statistical mechanics. The elastic modulus K derived from water isotherms is consistent with the values of Young's modulus measured directly by mechanical measurement. This provides an independent validation of the solution picture. In the surface adsorption picture, the protein is simplified as a static surface with adsorption sites [23]. There is a clear boundary between water and proteins [27] and changes of protein structure upon hydration are not taken into account. In the solution picture, water mixes with proteins changing both the enthalpy and entropy of the protein-water system. Side chain

rearrangements and volume expansion of protein upon hydration have important effects on the enthalpy and entropy of the system [6]. Consequently, water molecules associated with the upswing in water uptake alter significantly the thermodynamic properties and could play a major role in determining the energy landscape and dynamics of the combined protein-water system [4]. The present work also shows that a decreased elastic modulus K is essential for enabling the sorption of water associated with the upswing in water uptake above P/P_0 = 0.7. Previous studies show that water adsorption on charged and polar groups reduces K [34] and enhance the protein flexibility [2]. This suggests that adsorbed water at charged and polar groups is an enabling factor for the occurrence of the upswing in water uptake at higher relative pressures. The interplay of elastic modulus and water absorption has an important role in determining the fluctuations of proteins and may be important for the functions of proteins such as enzymatic activities [39].

4.5 Acknowledgements

This work was supported by NSF, Grant No. DMR-0906547, and by NIH, Grant No. R37GM049202.

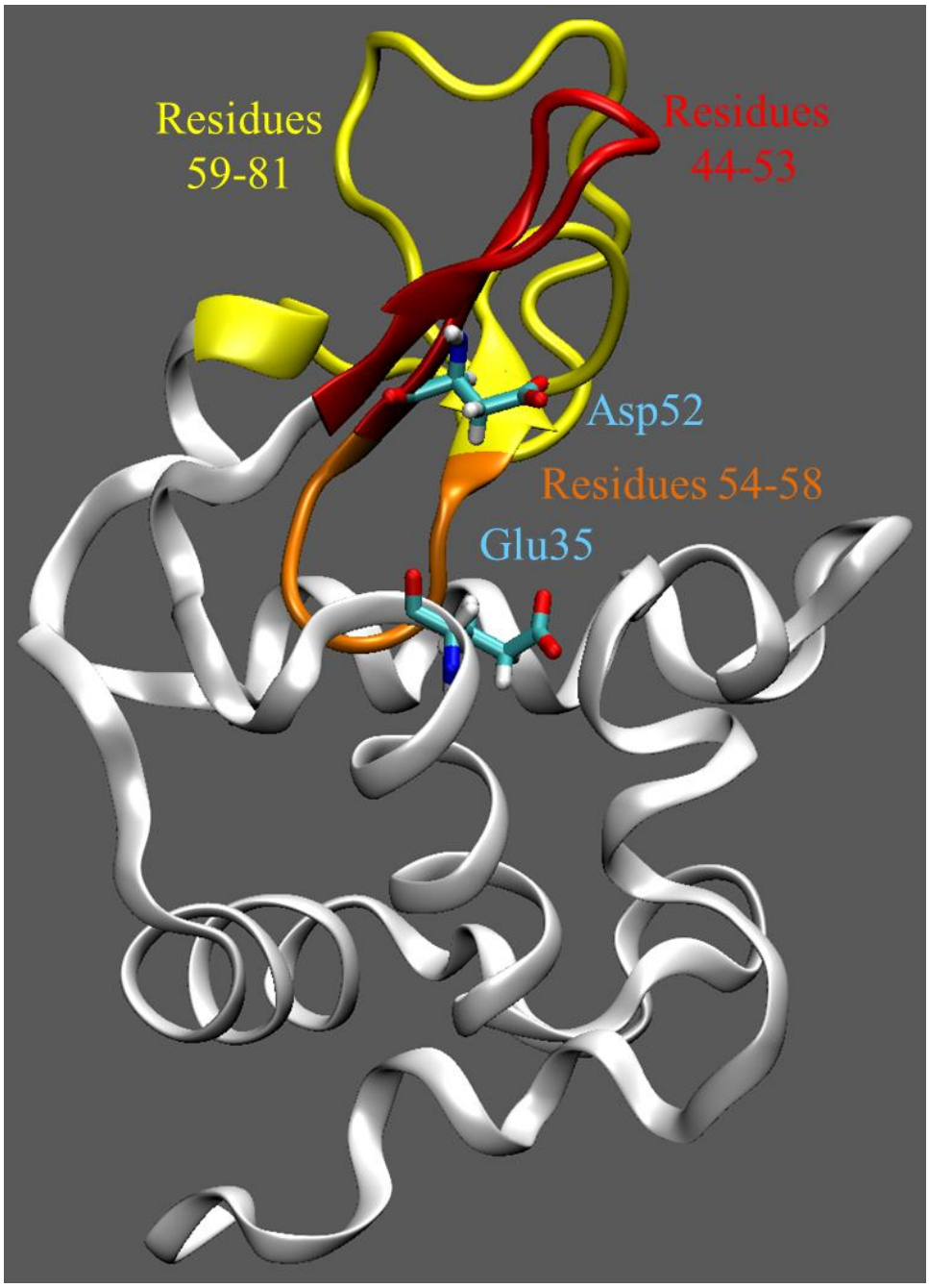

Figure 4.5 A ribbon representation of lysozyme structure from an averaged structure from the last 5 ns of 11 ns *NPT* simulations at 18°C and P/P_0 = 1. The residues with elevated fluctuations and correlated motions by hydration water are highlighted in red (dark gray, residues 44-53) and in yellow (light gray, residues 59-81). The residues with low fluctuations in the β-domain are shown in orange (gray, residues 54-58). Residues that are essential for the completion of the enzymatic reaction (Glu35 and Asp52) are shown in an atomic representation. The rest of the residues are shown in a narrow ribbon representation.

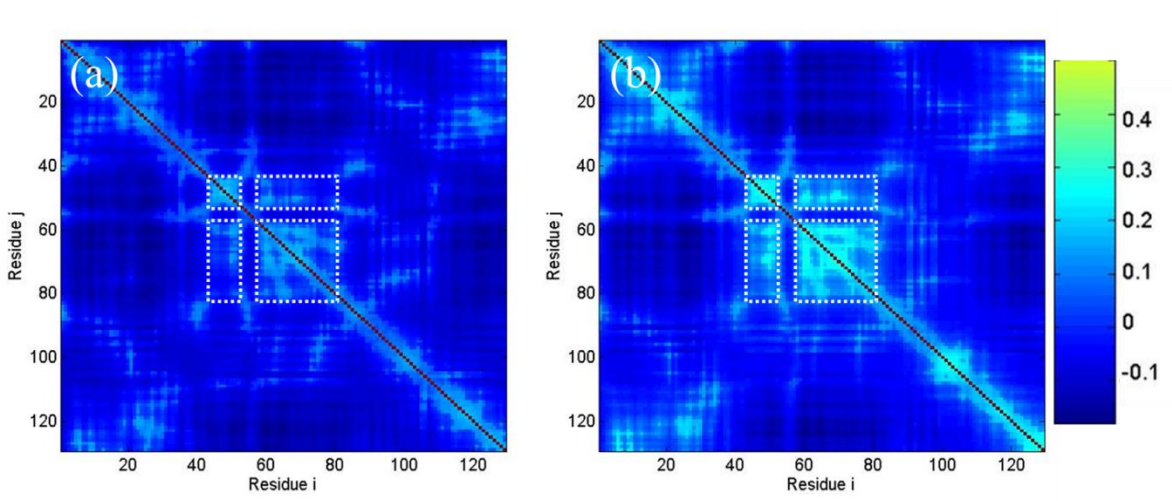

Figure 4.6 All-mode correlation plots of hen egg white lysozyme from normal mode analysis using the Gaussian network model. The *NPT* simulations are under comparable conditions to the experiments at relative vapor pressure of P/P_0=0.6 ($N_{hydration}$ =124) (a) and P/P_0=1 ($N_{hydration}$ =360) (b), and the temperature of 18°C. Averaged structures from the last 5 ns of 11-ns MD simulations were used for the GNM analyses. Cross correlation of motion is color-coded using the color (gray) scale to the right. The most profound increases in diagonal intensities are from residues 44-53 (upper-left dashed squares and the red region in Figure 4.5) and residues 59-81 (lower-right dashed squares and the yellow region in Figure 4.5). The corresponding increases in off-diagonal intensities between these two residue groups are labeled by rectangles.

4.6 References

[1] W. Kauzmann, Adv. Protein. Chem. **14**, 1 (1959).

[2] J. A. Rupley, and G. Careri, Adv. Protein. Chem. **41**, 37 (1991).

[3] Y. Levy, and J. N. Onuchic, Annu. Rev. Biophys. Biomol. Struct. **35**, 389 (2006).

[4] H. Frauenfelder *et al.*, Proc. Natl. Acad. Sci. USA **106**, 5129 (2009).

[5] R. M. Daniel *et al.*, Annu. Rev. Biophys. Biomol. Struct. **32**, 69 (2003).

[6] I. D. Kuntz, and W. Kauzmann, Adv. Protein. Chem. **28**, 239 (1974).

[7] D. M. Huang, and D. Chandler, Proc. Natl. Acad. Sci. USA **97**, 8324 (2000).

[8] B. Halle, Philos. Trans. R. Soc. Lond., B, Biol. Sci. **359**, 1207 (2004).

[9] K. Henzler-Wildman, and D. Kern, Nature **450**, 964 (2007).

[10] X. Q. Chu *et al.*, J. Phys. Chem. B **113**, 5001 (2009).

[11] G. Careri, A. Giansanti, and E. Gratton, Biopolymers **18**, 1187 (1979).

[12] G. Diakova *et al.*, J. Magn. Reson. **189**, 166 (2007).

[13] G. Careri *et al.*, Nature **284**, 572 (1980).

[14] C. Sauter *et al.*, Acta Crystallogr. D Biol. Crystallogr. **57**, 1119 (2001).

[15] S. H. Mao, A. Kleinhammes, and Y. Wu, Chem. Phys. Lett. **421**, 513 (2006).

[16] H. J. Wang *et al.*, Science **322**, 80 (2008).

[17] R. R. Sotelo-Mundo *et al.*, Protein Peptide Lett. **14**, 774 (2007).

[18] S. W. Benson, D. A. Ellis, and R. W. Zwanzig, J. Am. Chem. Soc. **72**, 2102 (1950).

[19] R. Diamond, J. Mol. Biol. **82**, 371 (1974).

[20] A. Abragam, *The Principles of Nuclear Magnetism* (Clarendon Press, Oxford, 1961).

[21] H. B. Bull, J. Am. Chem. Soc. **66**, 1499 (1944).

[22] J. H. de Boer, *The dynamical character of adsorption* (Clarendon, Oxford, 1968).

[23] R. L. D'Arcy, and I. C. Watt, Trans. Faraday Soc. **66**, 1236 (1970).

[24] W. S. Hnojewyj, and L. H. Reyerson, J. Phys. Chem. **65**, 1694 (1961).

[25] J. W. Rowen, and R. Simha, J. Phys. Chem. **53**, 921 (1949).

[26] P. J. Flory, *Principles of Polymer Chemistry* (Cornell Univ, Ithaca, NY, 1953).

[27] F. M. Richards, Annu. Rev. Biophys. Bioeng. **6**, 151 (1977).

[28] P. J. Flory, J. Chem. Phys. **10**, 51 (1942).

[29] W. Doster *et al.*, Biophys. J. **50**, 213 (1986).

[30] F. J. Millero, G. K. Ward, and P. Chetirkin, J. Biol. Chem. **251**, 4001 (1976).

[31] A. V. Gorelov, and V. N. Morozov, Biophys. Chem. **28**, 199 (1987).

[32] M. Tachibana *et al.*, Chem. Phys. Lett. **332**, 259 (2000).

[33] I. D. Kuntz, J. Am. Chem. Soc. **93**, 514 (1971).

[34] V. N. Morozov *et al.*, Int. J. Biol. Macromol. **10**, 329 (1988).

[35] N. J. Hipp, M. L. Groves, and T. L. McMeekin, J. Am. Chem. Soc. **74**, 4822 (1952).

[36] H. B. Bull, and K. Breese, Arch. Biochem. Biophys. **128**, 497 (1968).

[37] P. L. Poole, and J. L. Finney, Int. J. Biol. Macromol. **5**, 308 (1983).

[38] D. R. Squire, A. C. Holt, and W. G. Hoover, Physica **42**, 388 (1969).

[39] T. Imoto *et al.*, Protein Eng. **7**, 743 (1994).

[40] T. W. Allen, O. S. Andersen, and B. Roux, J. Gen. Physiol. **124**, 679 (2004).

[41] J. Fitter *et al.*, Proc. Natl. Acad. Sci. USA **93**, 7600 (1996).

[42] J. Partridge *et al.*, Biochim. Biophys. Acta-Protein Struct. Molec. Enzym. **1386**, 79 (1998).

[43] J. Smith *et al.*, J. Biomol. Struct. Dyn. **4**, 583 (1987).

[44] D. J. Vocadlo *et al.*, Nature **412**, 835 (2001).

[45] D. A. Case *et al.*, Amber 10, University of California, San Francisco (2008).

[46] W. Humphrey, A. Dalke, and K. Schulten, J. Mol. Graphics **14**, 33 (1996).

[47] M. M. Tirion, Phys. Rev. Lett. **77**, 1905 (1996).

[48] L. W. Yang *et al.*, Nucleic Acids Res. **34**, W24 (2006).

[49] X. Chen, I. Weber, and R. W. Harrison, J. Phys. Chem. B **112**, 12073 (2008).

CHAPTER 5

TEMPERATURE DEPENDENCE OF HEMOGLOBIN HYDRATION AND THE DYNAMICS OF HYDRATION WATER

5.1 Introduction

In CHAPTER 4, I established an *in situ* NMR method to measure the water sorption isotherm in proteins [1]. I studied the role of water in lysozyme, a small globular protein. The observed temperature dependence was well-explained by the solution model based on the Flory-Huggins theory with the addition of an elastic energy term. Based on these finding I now set out to determine if this temperature dependence also exist in other larger or non-globular proteins. In lysozyme I also found a relationship between the hydration water and protein dynamics. However, I was not able to provide direct evidence on the role of water in protein function. The biological function of lysozyme requires it to bind to a peptidoglycan molecule. This is difficult to implement with the current *in situ* water and gas loading system. It would be much easier to study the protein function if the biological function involves the binding to a gas ligand.

To examine the role of hydration on protein function I now examine the protein hemoglobin. Water may play a pivotal role in the dynamics and gas binding of hemoglobin, including the well-known allosteric effect [2-4]. Gases, including oxygen, carbon monoxide, and nitric oxide, can bind to the heme group, residing in the interior of hemoglobin resulting in either normal biological functioning or disease [5, 6]. Water can affect such a process as it

migrates within protein cavities and through the physical pathway that transports the gas. Furthermore, the presence of water modulates protein dynamics such as gates and portals [7]. It is therefore important to understand the dynamical property of hydration water. Protein hydration, as measured by nuclear magnetic resonance, shows a similar temperature dependence to that observed in lysozyme [1]. NMR relaxation due to the paramagnetic centers that are present in hemoglobin can reveal the dynamics of hydration water within the protein.

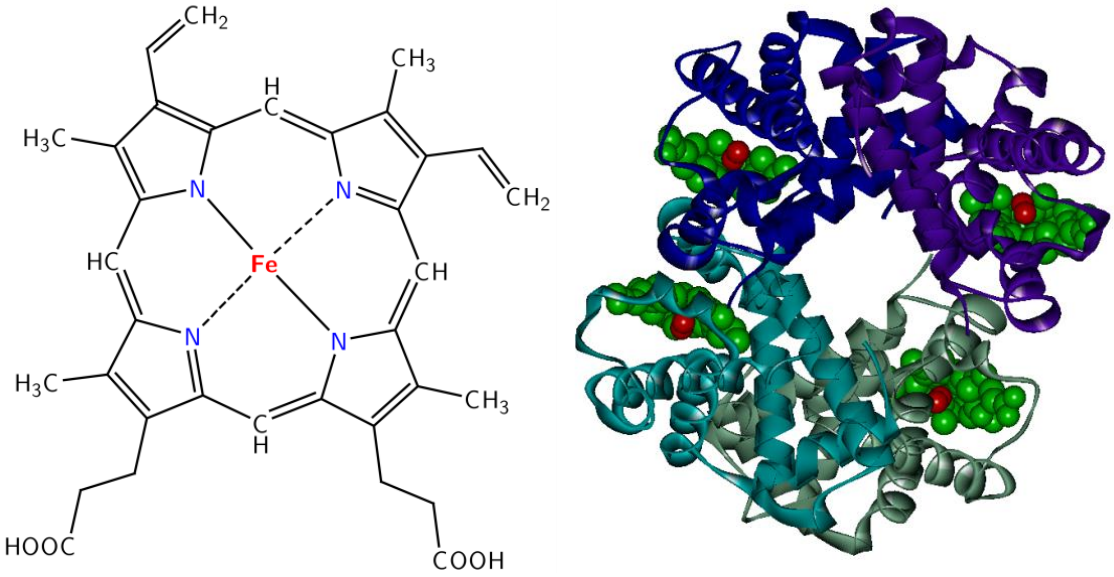

Figure 5.1 (a) Structure of the heme group with an iron in the center. (b) Secondary structures and oxygen binding sites of hemoglobin (PDB: 1GZX) in a ribbon representation. The heme groups are highlighted with a CPK representation.

Hemoglobin is the major oxygen transporter in blood. Its secondary structure is shown in Figure 5.1. Its oxygen binding ability comes from the heme groups, each of which contains an iron (Fe) ion. The Fe ion may be either in the Fe^{2+} or in the Fe^{3+} state. In a reversible process, oxygen temporarily oxidizes Fe^{2+} to Fe^{3+}, resulting in a superoxide ion [8].

Accordingly, the protein changes from the deoxy- to the oxy- state. Only the ferrous form (Fe^{2+}) of the protein can bind to oxygen. Another oxidation process leads to the ferri form (Fe^{3+}) of the protein, methemoglobin, which oxygen is unable to bind to. In the human body, the enzyme methemoglobin reductase reduces the iron center and is able to reactivate methemoglobin. Malfunctions in this reduction process lead to the methemoglobinemia.

$$HbFe(II) + O_2 \underset{\longleftarrow}{\xrightarrow{\text{Physilogical condition}}} HbFe(III)\bullet O_2^-$$

Deoxy-hemoglobin	Oxy-hemoglobin
High Spin Fe(II)	Low Spin Fe(III)+Superoxide Ion
Paramagnetic	Diamagnetic

$$HbFe(III)\bullet O_2^- \xrightarrow[0.5\sim3\%/\text{day}]{\text{autoxidation}} HbFe(III) + O_2^-$$

Oxy-hemoglobin	Methemoglobin
Diamagnetic	Paramagnetic

Figure 5.2 Different oxidization states of hemoglobin.

The oxygen binding process also changes the magnetic properties of the protein. In the ferrous form, the high spin Fe^{2+} contains an unpaired electron. This leads to the paramagnetic property of deoxy-hemoglobin. During the oxygen binding process, the unpaired electron move towards the paramagnetic oxygen molecule to form a superoxide, resulting in the diamagnetic oxy-hemoglobin with low spin Fe^{3+}. On the other hand, when oxidized to methemoglobin, Fe^{3+} stays in the high spin states and the protein remains paramagnetic. Figure 5.2 shows the different oxidization states of hemoglobin and their magnetic properties. Changes in the magnetism properties can be monitored by electron paramagnetic resonance [9]. In nuclear magnetic resonance, the existence of a paramagnetic center broadens the resonance line by increase the local field inhomogeneity and enhances

the spin-lattice relaxation through nuclear-electron coupling and spin diffusion [9, 10]. In this chapter, I am able to use the spin-lattice relaxation to interpret the dynamics of hydration water in the proximity of hemoglobin.

5.2 Experiments

Hemoglobin from bovine blood (catalog no. H7379, lyophilized powder) was purchased from Sigma Aldrich and used without further modification. Since native hemoglobin is readily oxidized in air, these samples are predominantly in paramagnetic form of hemoglobin, methemoglobin. The protein powder was loaded into the quartz NMR sample tube connected to an *in situ* water loading system with controlled vapor pressure and temperature [11]. A single RF pulse (~5 μs) was used to excite the ^{1}H NMR signals at 0.8 T (34 MHz ^{1}H NMR frequency). The resulting spectrum contains two major components: a sharp peak on top of a broad peak. The broad peak was assigned to proton background solely from protein molecules [12]. The sharp peak was assigned to water sorption in the protein [12]. Since the protons account for about 6.8% weight of a protein molecule [13], the hydration level *h* can be calculated from the intensity ratio of the sharp to the broad peaks of NMR spectra at equilibrium. Here, the effect of the detection delay (~8 μs) on the intensity of the free-induction-decay (FID) of the broad peak was taken into account based on a Gaussian decay [9]. The isotherms measured by ^{1}H NMR were shown to be consistent with those obtained by traditional gravimetric technique [12]. NMR relaxation measurements were made using the standard saturation recovery and Hahn echo sequences [14].

5.3 Results and Discussion

5.3.1 Water sorption isotherms and elastic modulus

Water sorption isotherms in hemoglobin at 18°C and 4° are show in Figure 5.3. At high relative pressures ($P/P_0 > 0.7$), the isotherms demonstrate a clear temperature dependence. Furthermore they show that there is less hydration water at the lower temperature. Such a temperature dependence was previously observed in lysozyme, as described in CHAPTER 4 [1]. The sorption isotherms provide further support that this temperature dependence exists not only in small globular proteins such as lysozyme, but also in large proteins such as hemoglobin. The surface adsorption model does not sufficiently describe such temperature dependence. The decrease in water uptake could be explained by the increased elastic energy cost for hydration at decreased temperature. It follows that the temperature dependence of the elastic modulus, *K*, of the protein is responsible for the observed temperature dependence of the upswing in water uptake.

The quantitative analysis of such elastic energy is based on the lattice model of Flory-Huggins theory with an addition of an elastic term [1, 15, 16]. Equating the chemical potentials of water in the vapor phase and in the water-protein mixture leads to [16-18]:

$$\left[\ln\left(P/P_0\right) - \eta \ln v_1 - \eta v_2\right] v_2^{-2} = \chi + \frac{K\bar{V}_1}{2k_B T}\left(\frac{1}{v_2^{1/3}} - 1\right)\left(\frac{5}{3v_2^{1/3}} - 1\right) v_2^{-2} \qquad (4.3)$$

Here, the plot of $\left[\ln\left(P/P_0\right) - \eta \ln v_1 - \eta v_2\right] v_2^{-2}$ versus $\left(v_2^{-1/3} - 1\right)\left[(5/3)v_2^{-1/3} - 1\right] v_2^{-2}$ is linear with the intercept at χ and the slope containing the elastic modulus *K*. This is true so long as both parameters are constant within a certain range of relative pressures. Using the partial specific density of water ($\rho_1 = 1.0$ g/cm^3) and hemoglobin ($\rho_2 = 1.38$ g/cm^3), v_1 and v_2 can

be determined from the hydration level h via $v_1 = 1 - v_2$ and $v_2 = 1/(h\rho_2/\rho_1 + 1)$. Since hemoglobin has residues that are compact, the core may not be readily available to mix with water molecules [19]. This can be taken into account by considering the fraction of flexible segments in the protein, η, where $0 \le \eta \le 1$ [17, 18]. Given hemoglobin's large size, $\eta = 0.5$ is a good estimation for the fraction of flexible segments.

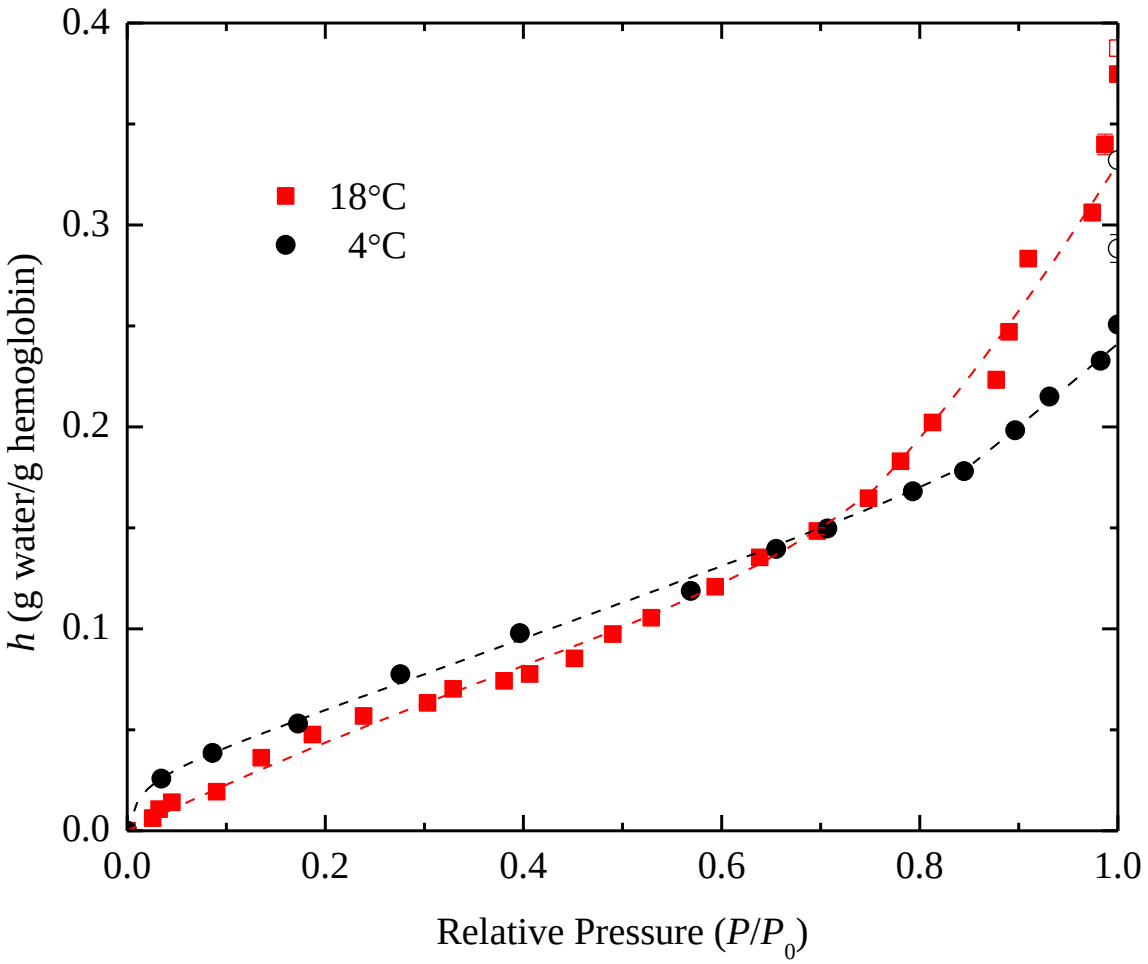

Figure 5.3 Temperature-dependent water sorption isotherms in hemoglobin. The dashed lines are fitted to D'Arcy-Watt isotherms at low relative pressure region. At high relative pressure, the isotherm is fitted into the implicit form of Rowen-Simha equation [16].

Figure 5.4 plots the same isotherm data in the scale of $\left[\ln\left(P/P_0\right)-\eta\ln v_1-\eta v_2\right]v_2^{-2}$ versus $\left(v_2^{-1/3}-1\right)\left[\left(5/3\right)v_2^{-1/3}-1\right]v_2^{-2}$ based on the Rowen-Simha equation and $\eta=0.5$ [1, 16]. There are linear portions to the right of the horizontal axis, corresponding to the isotherm data at high relative pressure. The linear fittings lead to $K=0.80\pm0.16$ GPa and $\chi=0.35\pm0.03$ at 18°C, and $K=1.64\pm0.13$ GPa and $\chi=0.33\pm0.03$ at 4°C. Both the absolute values and their temperature dependence are reasonable compared to those obtained for lysozyme [1]. These results provide further support for the solution model of protein hydration in hemoglobin. Mechanical measurements of the elastic modulus of hemoglobin crystals are needed for comparison.

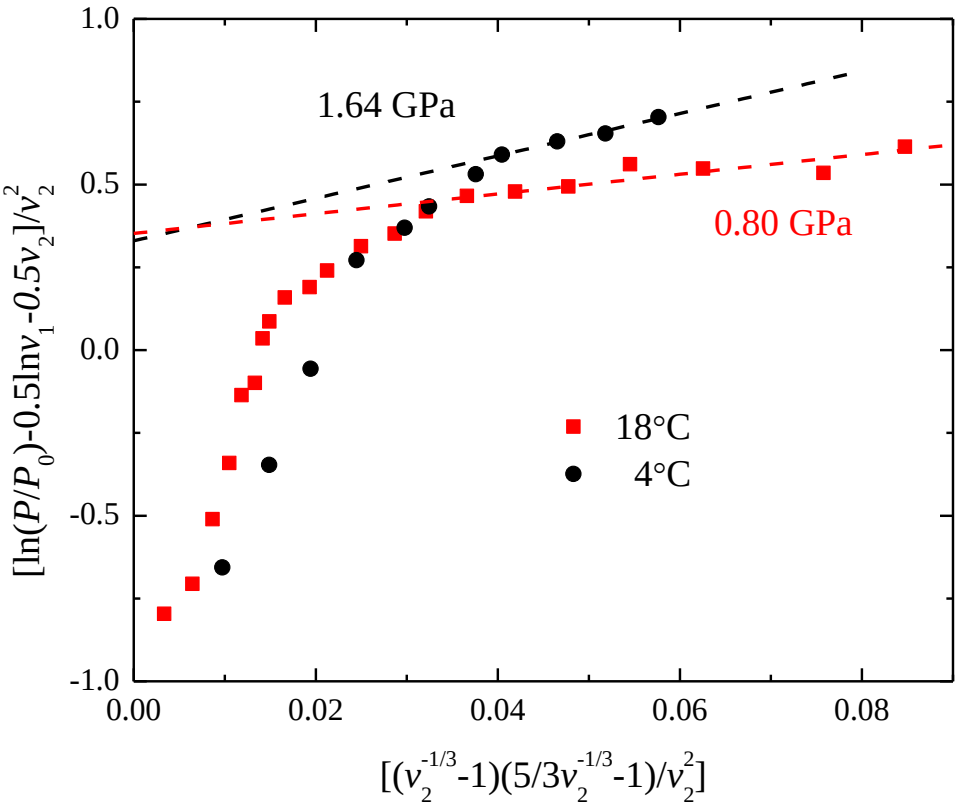

Figure 5.4 Plots of $[\ln(P/P_0)-0.5\ln v_1-0.5v_2]/v_2^2$ versus $[(v_2^{-1/3}-1)(5/3v_2^{-1/3}-1)/v_2^2]$ for the isotherms data following the Rowen-Simha equation [16].

5.3.2 Line broadening and the diffusion barrier

What makes the methemoglobin more interesting is the paramagnetic property, which is absent in lysozyme. In the ferri- or met- form of hemoglobin, the unpaired electrons have a magnetic moment $\mu_S = g\mu_B\sqrt{S(S+1)}$, where g is a proportionality constant relating the angular and magnetic moments, S is the total spin of the unpaired electrons, and μ_B is the electron Bohr magnetron [10]. The presence of paramagnetic centers leads to line broadening in NMR spectra and an enhancement in relaxation [10]. Protons in close proximity to the paramagnetic center experience a large magnetic field shift from the external static field. This leads to line broadening of the NMR spectra. Depending on the distance from the paramagnetic center, the proton resonance line may be too broad to be observed by NMR. Commonly the diffusion barrier is used as the radius from the paramagnetic center within which the proton remains NMR-silent due to the line broadening. Assuming the dipolar interaction is responsible for the coupling between the nuclear and electron spin, the diffusion barrier is the distance at which the magnetic field due to the paramagnetic center is equal to the local nuclear dipolar field:

$$H_S = \frac{\mu_0}{4\pi}\cdot\frac{\mu_S^{eff}}{b^3} = H_I = \frac{1}{\gamma_H T_2} \qquad (4.4)$$

where μ_S^{eff} is the effective electron dipole moment, T_2 is the spin-spin relaxation time of protons, and γ_H is the gyromagnetic ratio of proton. The effective electron dipole moment μ_S^{eff} depends on the spin-lattice relaxation time of the paramagnetic ions (T_{1e}), compared to T_2 ($T_2 \approx 17\ \mu s$) of nuclear spin-spin relaxation time. If the paramagnetic ions are dilute and

any interactions between them can be neglected, the T_{1e} of electron spin can be replaced by the correlation time (τ) of the z component of the spin *S*.

$$\mu_S^{eff} = \begin{cases} \mu_S & \tau \gg T_2 \\ \mu_S \cdot \dfrac{\mu_S H_0}{kT} & \tau \ll T_2 \end{cases} \tag{4.5}$$

At low field and fast electron correlation time, which is usually on the order of 10^{-8} to 10^{-13} s, the proton feels only the time average of the electron spin, or the Curie spin.

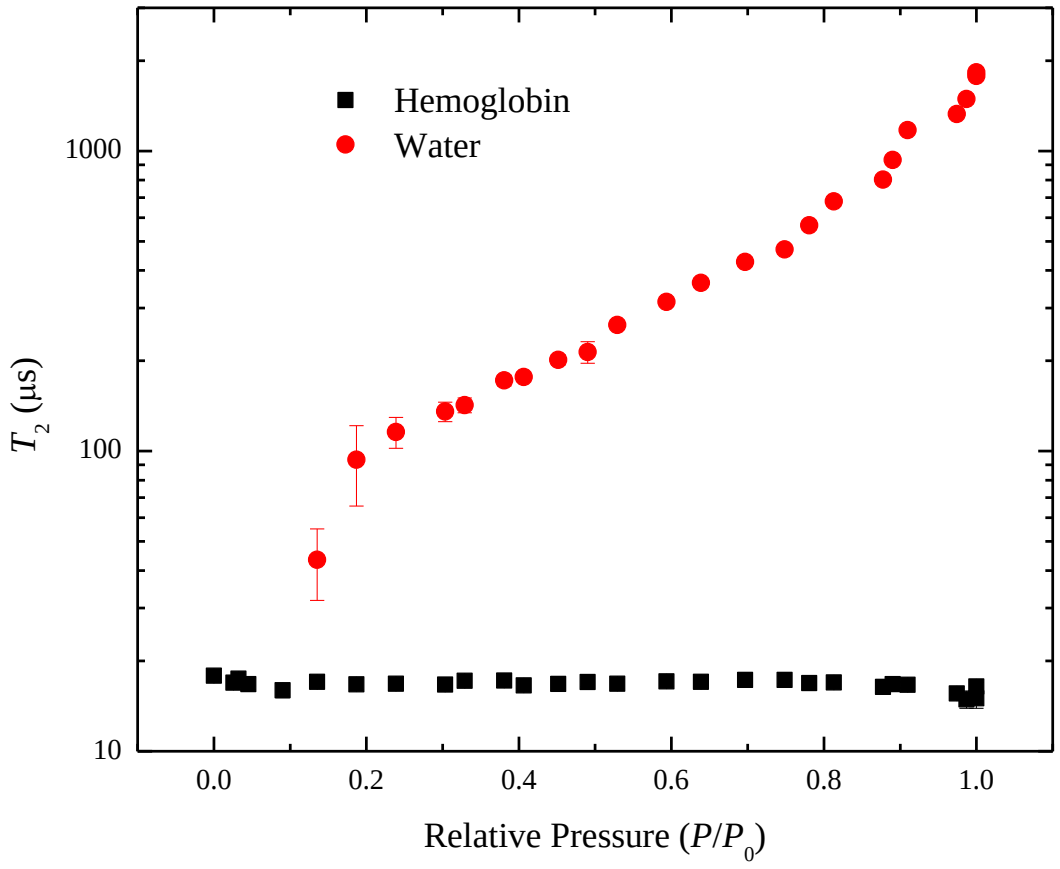

Figure 5.5 The spin-spin relaxation time for hemoglobin and its hydration water.

Figure 5.5 shows the measured T_2 of hemoglobin and its hydration water. The spectra were measured using a Hahn echo sequence. In each of the resulting spectra there are two

distinct peaks: a broader peak corresponding to the protons in the proteins, and a narrower peak corresponding to the protons from hydration water. These unique spectral features allow the T_2 values of the protein and hydration water to be obtained by examining the intensities of the two distinct peaks. The T_2 of the protein, $\sim 17\ \mu s$, remains constant throughout the hydration process. On the other hand as the partial pressure is increased, the hydration water T_2 increases from $\sim 40\ \mu s$ to $2\ ms$. This is consistent with the picture of protein hydration in which at the beginning of hydration, water is present as structural water, and at the final stage of hydration, water demonstrates the properties of bulk water.

Using the hemoglobin $T_2 \sim 17\ \mu s$, the diffusion barrier can be estimated as,

$$b = \left[\gamma_H T_2 \cdot \frac{\mu_0}{4\pi} \cdot \mu_S \cdot \frac{\mu_S H_0}{kT} \right]^{1/3} = 4.84 \times 10^{-18}\ \text{m} \qquad (4.6)$$

The extremely small value of the diffusion barrier suggests that all protons are observable through NMR under the current conditions, low external static field and strong nuclear dipolar field.

Figure 5.6 shows the distribution of protons versus their distance from the closest methyl group and from the paramagnetic center (Fe^{3+}). Since only a small number of protons reside within 3Å of the paramagnetic center, the majority of protons contribute to the NMR signals. This confirms that the calibration method I used is valid and the separation of signals from water and protein can be achieved by their dramatic difference in T_2.

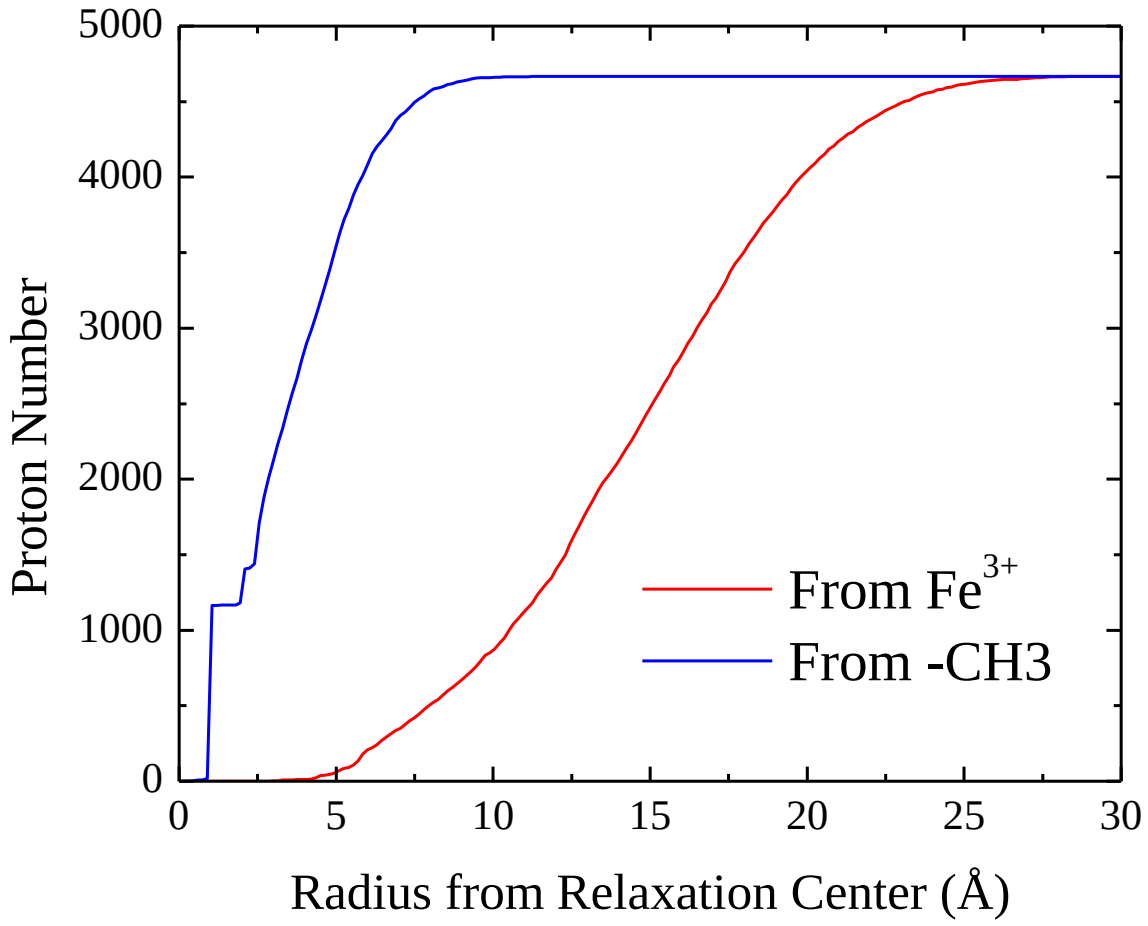

Figure 5.6 The number of protons within a radius from the relaxation centers based on the structure of hemoglobin (1GZX).

5.3.3 Spin-lattice relaxation of proteins

In diamagnetic hydrated proteins, the proton spin-lattice relaxation time is dominated by cross relaxation and spin diffusion [20]. Due to fast spin diffusion in proteins and more rapid chemical exchange in water, the protons in the protein phase and in the water phase are in a uniform spin temperature in their respective phases. In the protein phase, the fast-rotating methyl groups are widely presented in proteins. The spin-lattice relaxation of the surrounding protons is made more efficient by transferring their spin energy to the methyl groups through the spin diffusion. The hydration water near proteins can exchange spin energy through

dipolar coupling between the two proton phases. This leads to cross relaxation between the two phases and spin diffusion towards methyl groups.

The influence of the paramagnetic centers on the proton spin-lattice relaxation can be evaluated based on Bloembergen's model of relaxation [21]. The proton spin energy can relax either through its direct interaction with the unpaired electrons or through spin diffusion. For the direct dipolar interaction between a proton and an unpaired electron, the paramagnetic contribution to the spin lattice relaxation of the proton is [9, 22]:

$$\frac{1}{T_1} = \frac{2}{15} \cdot \frac{\gamma_H^2 \cdot g^2 \cdot \beta^2}{r^6} \cdot S \cdot (S+1) \cdot \left(\frac{3\tau_p}{1+\omega_H^2 \tau_p^2} + \frac{7\tau_p}{1+\omega_S^2 \tau_p^2} \right) \tag{4.7}$$

where γ_H is the proton gyromagnetic ratio, ω_S is the electron Larmor frequency, S is the total electronic spin of an iron atom ($S = 5/2$ for methemoglobin [23]), r is the distance between the proton and the iron atom, β is the Bohr magnetron, and g is the electronic Lande factor (taken here as that of a free electron). In the slow motion limit, the correlation time is equal to the longitudinal relaxation time of the unpaired electron, $\tau_p = \tau_s = 6.1 \times 10^{-12}$ s. The large difference between the nuclear and electron Larmor frequency allows us to express the spin lattice relaxation in the form of

$$1/T_1 = C \cdot r^{-6} \tag{4.8}$$

where $C = 2/5 \cdot \gamma_H^2 \cdot g^2 \cdot \beta^2 \cdot S \cdot (S+1) \cdot \tau_p = 5.25 \times 10^{-42}$ cm^6/s.

The spatial distribution of the magnetization and its diffusion was analyzed by de Gennes [24] and Blumberg [25] using Bloembergen's model. The most important parameter is the spin diffusion constant, which can be approximated by [9, 21, 25]:

$$D \approx \frac{a^2}{50T_2} = \frac{(2.5\ \text{Å})^2}{50 \times 17\ \mu\text{s}} = 7.353 \times 10^{-17}\ \text{m}^2/\text{s} = 7.353 \times 10^{-13}\ \text{cm}^2/\text{s} \qquad (4.9)$$

where I have used $a = 2.5$ Å, the typical distance between proton groups [22, 26], and the measured $T_2 \approx 17\ \mu$s. This spin diffusion constant is several orders of magnitude larger than that in protein solution, where the dipolar interaction is averaged by the molecular motion [9, 22]. This suggests the spin diffusion mechanism is more effective than the relaxation due to the direct dipolar interaction.

The spatial and temporal distributions of nuclear spin magnetization are essential components of the spin diffusion mechanism. After a very short time given by de Gennes, $t \approx 0.5\left(C/D^3\right)^{1/2} = 1.817$ ms in the case of hemoglobin, the nuclear spins within the pseudopotential radius of paramagnetic center,

$$\rho = \frac{\pi}{2^{5/2}\left[\Gamma(5/4)\right]^2}\left(C/D\right)^{1/4} = 3.515\ \text{Å} \qquad (4.10)$$

have relaxed to equilibrium. As shown in Figure 5.6, most of the protons reside outside this radius and their spin-lattice relaxation rate is determined by the spin diffusion mechanism. Such a relaxation rate is estimated by

$$1/T_1 = 4\pi N \rho D = 8.5 N C^{1/4} D^{3/4} = 10.46\ \text{s}^{-1} = 1/(96\ \text{ms}) \qquad (4.11)$$

This estimation is very close to the longer component of proton spin-relaxation in proteins ~ 120 ms. The shorter component comes from the exchange with hydration water and cross relaxation.

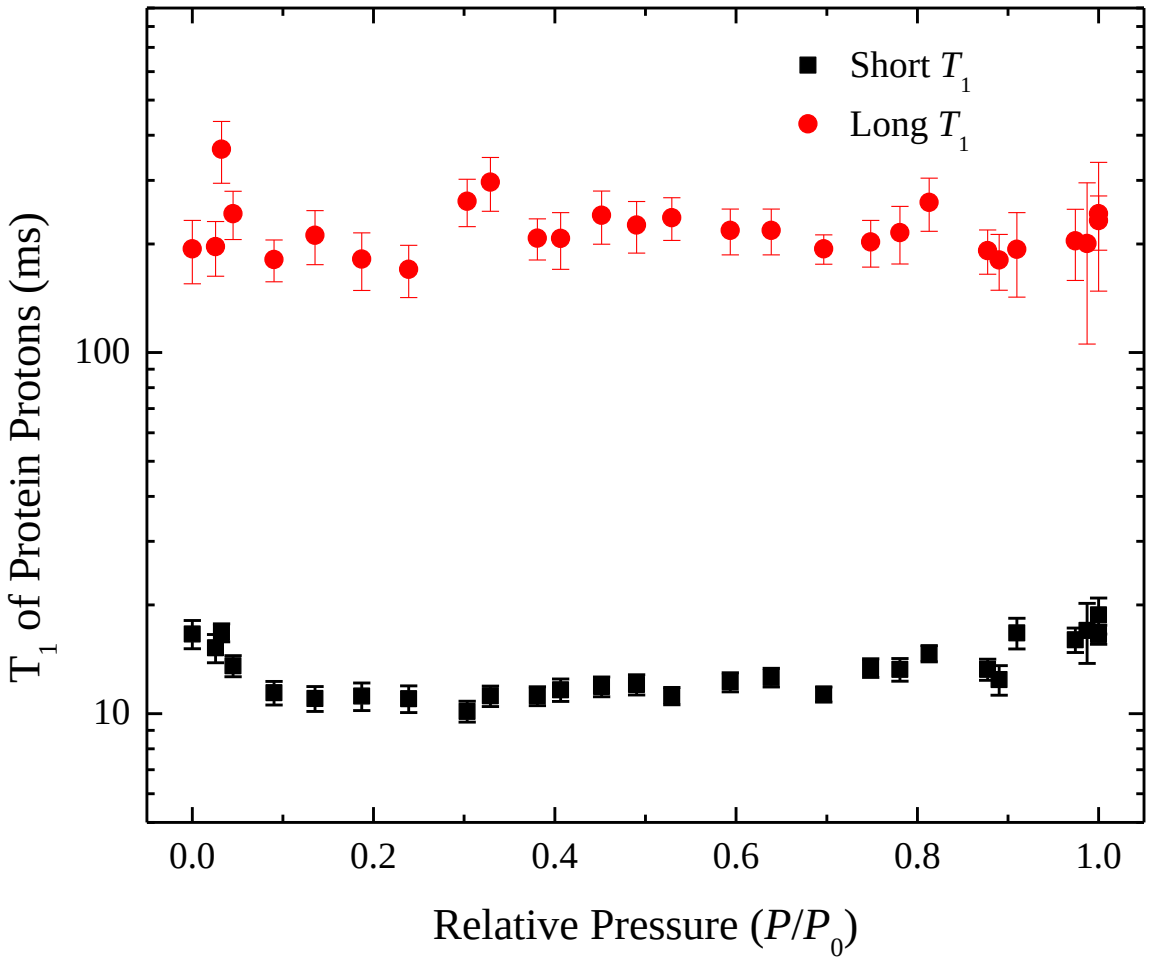

Figure 5.7 The value of long and short components of the spin-lattice relaxation time of proteins.

5.3.4 Spin-lattice relaxation of hydration water

Figure 5.8 shows the measured T_1 of water. There are two components, a longer component on the order of magnitude of $10\ \text{ms}$ and shorter component of $1\ \text{ms}$. The longer T_1 of water is similar in magnitude to the shorter T_1 found in proteins. This suggests that there is an exchange mechanism between protein and hydration water. The exchange rate determines the value of the common T_1 in proteins and water. Without such exchange, the spin lattice relaxation of protein will lead to a single exponential with a characteristic time of

~ 120 ms, and ~ 1 ms for hydration water. The exchange between protein and hydration water bring out a common relaxation time of ~ 10 ms.

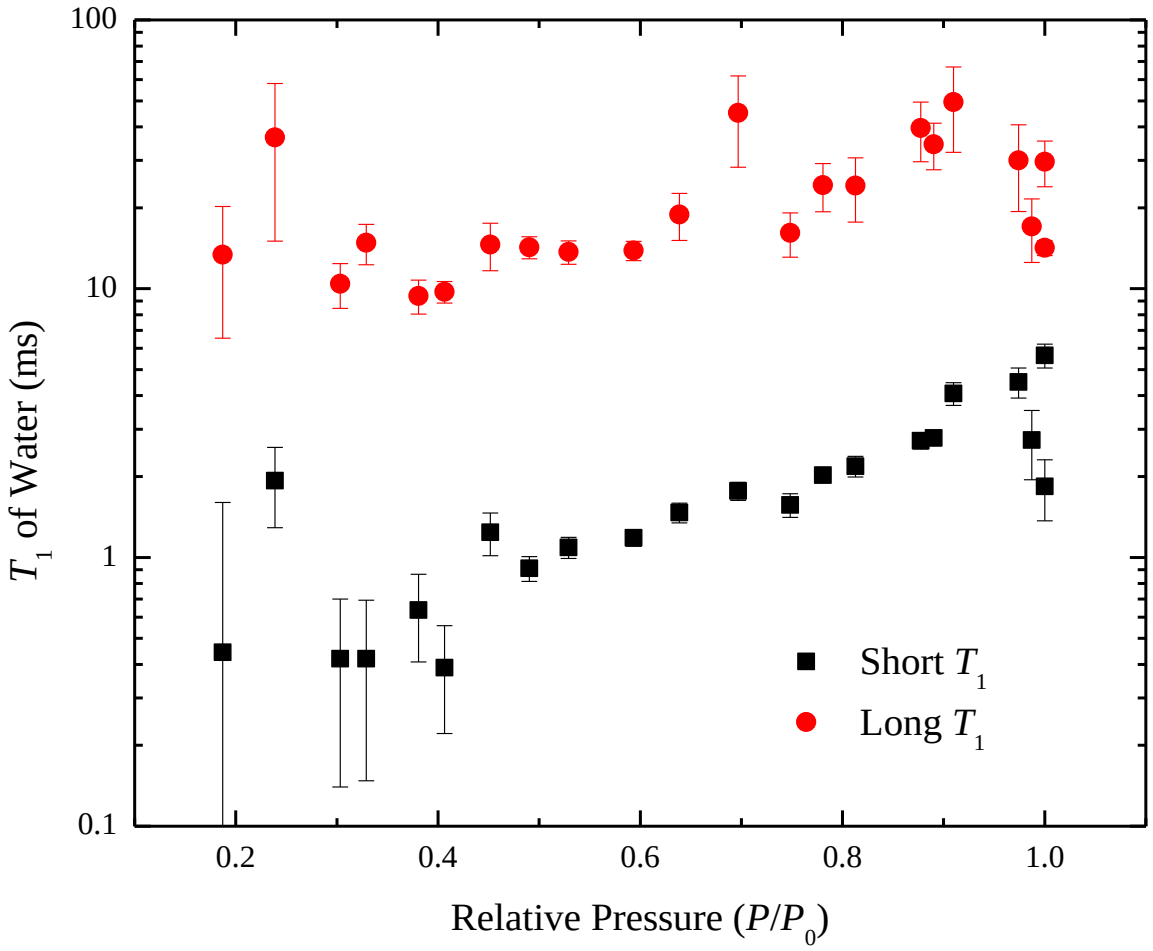

Figure 5.8 The value of long and short components of the spin-lattice relaxation time of water.

The shorter component is due to the paramagnetic centers. Since the atomic diffusion is much faster than the spin diffusion, the spin energy in water protons relaxes more efficiently through the atomic diffusion of protons towards the paramagnetic center. Using the same spin diffusion mechanism of $T_1 \propto D^{-3/4}$ and the spin diffusion constant in protein, $D_{spin}=7.353\times10^{-13}$ cm^2/s , I can estimate the proton diffusion constant,

$D_H = 4.352 \times 10^{-10}$ cm^2/s. This is much slower than the proton diffusion constant in pure water, $D_H = 1.85 \times 10^{-5}$ cm^2/s [27], and in the immediate vicinity of a phospholipid membrane, $D_H = 0.65 \times 10^{-5}$ cm^2/s [28]. The significant reduction of the diffusion constant is probably due to the confinement effect of the protein channel on the diffusion of water.

5.4 Conclusion

In conclusion, *in situ* measurements of water sorption isotherms in hemoglobin show temperature dependence in the water uptake at high relative pressure. Such temperature dependence is similar to what was observed in lysozyme as discussed in CHAPTER 4. This provides further support of the role of elastic energy in protein hydration. NMR relaxation in hemoglobin shows a cross relaxation between fast-relaxing water and slow-relaxing proteins due to different spin diffusion mechanisms. The spin-lattice relaxation can be used to estimate the diffusion constant of protons towards the paramagnetic center, which is several orders of magnitude slower than that in pure water.

5.5 References

[1] H. J. Wang *et al.*, Phys. Rev. E **83**, 031924 (2011).

[2] M. F. Colombo, D. C. Rau, and V. A. Parsegian, Science **256**, 655 (1992).

[3] H. Frauenfelder *et al.*, Proc. Natl. Acad. Sci. USA **106**, 5129 (2009).

[4] H. Frauenfelder, *Physics of proteins: an introduction to biological physics and molecular biophysics* (Springer, New York ;London, 2010).

[5] Q. H. Gibson, Proc. Natl. Acad. Sci. USA **70**, 1 (1973).

[6] D. B. Kim-Shapiro, Free Radical Biol. Med. **36**, 402 (2004).

[7] M. A. Scorciapino *et al.*, J. Am. Chem. Soc. **132**, 5156 (2010).

[8] T. Kanias, and J. P. Acker, FEBS J. **277**, 343 (2010).

[9] A. Abragam, *The Principles of Nuclear Magnetism* (Clarendon Press, Oxford, 1961).

[10] I. Bertini, P. Turano, and A. J. Vila, Chem. Rev. **93**, 2833 (1993).

[11] H. J. Wang *et al.*, Science **322**, 80 (2008).

[12] G. Diakova *et al.*, J. Magn. Reson. **189**, 166 (2007).

[13] R. Diamond, J. Mol. Biol. **82**, 371 (1974).

[14] C. P. Slichter, *Principles of magnetic resonance* (Springer-Verlag, Berlin ;New York, 1990).

[15] P. J. Flory, *Principles of Polymer Chemistry* (Cornell Univ, Ithaca, NY, 1953).

[16] J. W. Rowen, and R. Simha, J. Phys. Chem. **53**, 921 (1949).

[17] P. J. Flory, J. Chem. Phys. **10**, 51 (1942).

[18] W. Doster *et al.*, Biophys. J. **50**, 213 (1986).

[19] F. M. Richards, Annu. Rev. Biophys. Bioeng. **6**, 151 (1977).

[20] H. T. Edzes, and E. T. Samulski, Nature **265**, 521 (1977).

[21] N. Bloembergen, Physica **15**, 386 (1949).

[22] I. M. Russu, and C. Ho, Biophys. J. **39**, 203 (1982).

[23] C. Ho, Adv. Protein. Chem. **43**, 153 (1992).

[24] P. G. Degennes, J. Phys. Chem. Solids **7**, 345 (1958).

[25] W. E. Blumberg, Phys. Rev. **119**, 79 (1960).

[26] M. Eisenstadt, Biophys. J. **33**, 469 (1981).

[27] J. H. Simpson, and H. Y. Carr, Phys. Rev. **111**, 1201 (1958).

[28] M. Gutman, E. Nachliel, and S. Moshiach, Biochemistry **28**, 2936 (1989).

CHAPTER 6

ROLE OF INTERFACIAL WATER IN MEDIATING THE INTERACTION BETWEEN HALOTHANE AND PROTEINS

6.1 Introduction

In CHAPTER 4 and CHAPTER 5, I discussed the role of hydration water in lysozyme and hemoglobin, respectively. From water sorption isotherms of the proteins, I provided support for the solution description of protein hydration based on the Flory-Huggins theory with the addition of elastic energy term. Unlike lysozyme, hemoglobin's hose biological function involves binding to gas molecules. Such gas binding process could potentially be observed by NMR. A prime example of the coupling between gas-biomolecule binding and the modulation of biological activity is general anesthesia. The binding between general anesthetics and biomolecule leads to the inhibition of biological activity, a function which is still not fully understood.

The role of water in the action of general anesthesia remains a topic of controversy[1]. The first and well-established theory of general anesthesia was proposed by Meyer and Overton, who independently noticed that the anesthetic potency is related to its lipid solubility, as shown in Figure 6.1(a) [2, 3]. This leads to the hypothesis that solubilization of lipophilic general anesthetic in lipid bilayer of the neuron causes its malfunction and anesthetic effect when critical concentration of anesthetic is reached. Based on the anesthetic

effect on the activity of lipid-free proteins, Franks and Lieb demonstrated that protein targets are also compatible with the Meyer-Overton rule, as shown in Figure 6.1(b) [4-6].

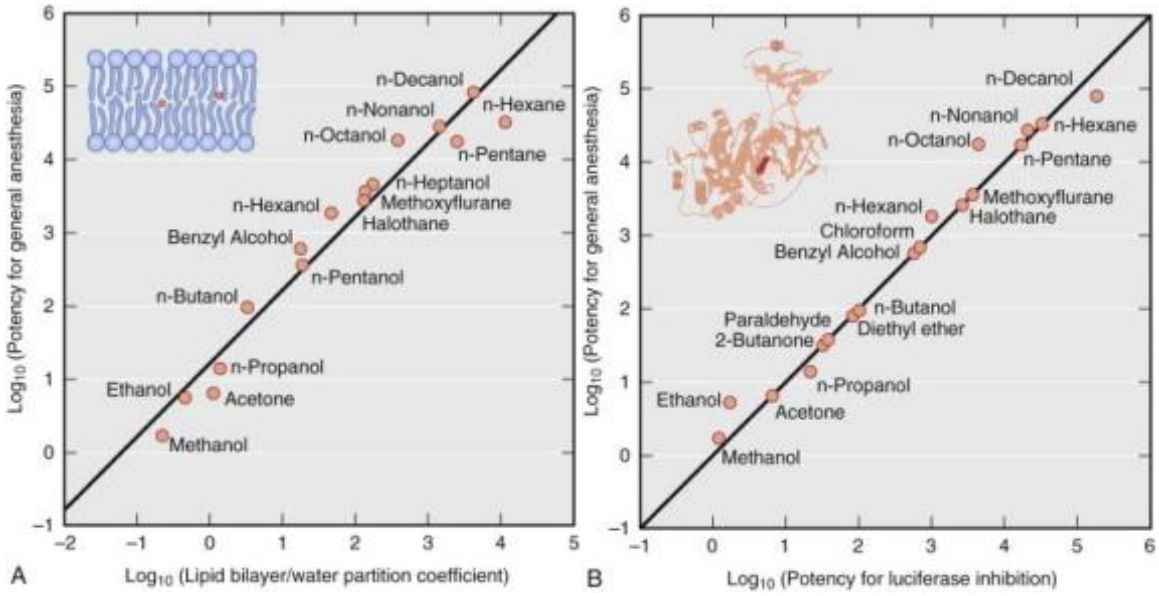

Figure 6.1 The Meyer-Overton correlation for anesthetics.

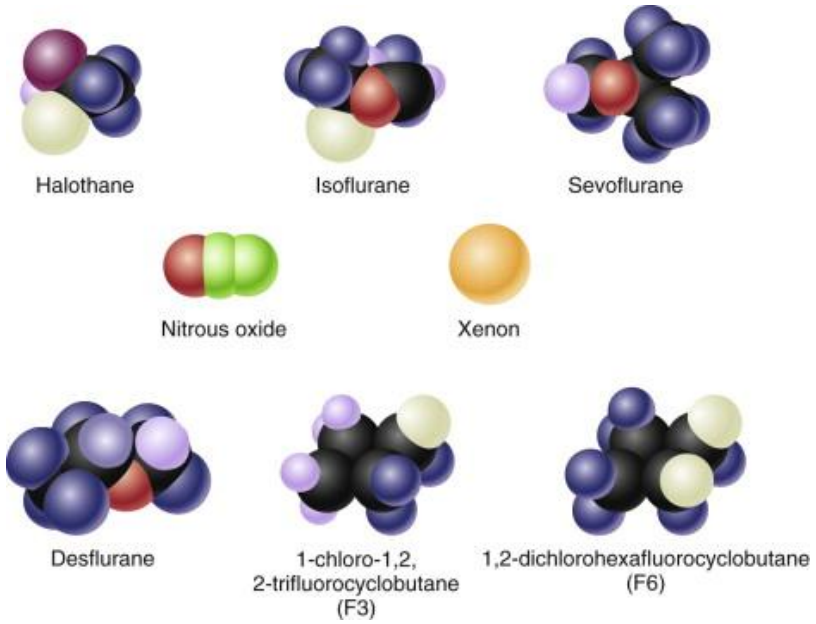

Figure 6.2 Structure of general anesthetics widely used in medicine [7].

The general anesthetics are substances that can bring reversible loss of consciousness. They are able to cross the blood-brain barrier to produce general anesthesia [8]. Hundreds of substances are known to cause general anesthesia, including chloroform ($CHCl_3$), halothane ($CF_3CClBrH$), nitrous oxide (N_2O), carbon dioxide (CO_2), ethylene (C_2H_4), cyclopropane (C_3H_6), sulfur hexafluoride (SF_6), nitrogen (N_2), argon (Ar), and xenon (Xe). Figure 6.2 shows the structure of several widely used general anesthetics [7]. They are apolar molecules that lack the ability to form covalent bonds as other drugs do. They interact with the anesthetic targets, either at the lipid portion of neuronal membranes or in the hydrophobic pocket of the target proteins, through weak polarization forces, such as the hydrophobic interaction [9]. Therefore there could be many correlations between the potency of an anesthetic and its physical properties that are affected by the same type of weak interaction, such as the Meyer-Overton rule [2]. The quantity used to compare the strengths or the potency of anesthetic vapors is the minimum alveolar concentration (MAC) [7]. It is defined as the concentration of the vapor in the lungs that is needed to prevent movement (motor response) in 50% of subjects in response to pain stimulus. A lower MAC value represents a more potent volatile anesthetic.

Deviations from Meyer-Overton rule were also found [7]. Stereoselectivity was observed in several anesthetics such as isoflurane and pentobarbital with different potencies in different optical isomers [10-13]. The cutoff effect exists in a series of alkanols and alkanes with favorable lipid solubility, whose potency increases with molecular weight until a point where potency is suddenly lost [14]. Both stereoselectivity and the cutoff effect could be related to the molecular shape and size of protein targets. Nonanesthetics show no anesthetic effect even with similar lipid solubility and molecular structure as known

anesthetics. The only noticeable difference is their low water solubility [15]. Evidence has been accumulated that anesthetics bind to amphiphilic sites with the presence of water [16, 17]. The existence of similar nonanesthetics and the amphiphilic nature of target binding sites lead to the hypothesis that water may also play a role in the binding of anesthetics and proteins.

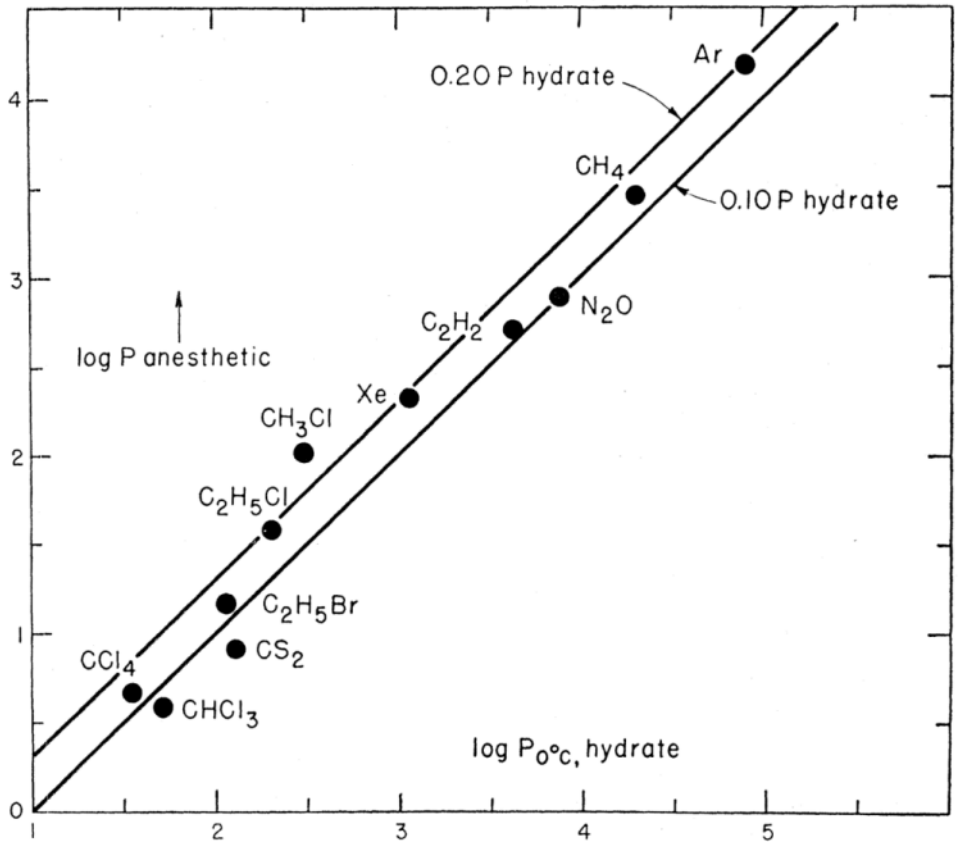

Figure 6.3 A diagram showing the logarithm of the anesthetizing partial pressure of non-hydrogen-bonding anesthetic agents plotted against the equilibrium partial pressure of their hydrate crystals [18].

The first molecular mechanism of anesthesia that emphasizes the role of water was proposed by Pauling and Miller [18, 19]. From the relation between the anesthetizing potency with the equilibrium partial pressure of their corresponding hydrates at 0°C (as

shown in Figure 6.3), the anesthetics could induce a structural change of interfacial water to form minute hydrate (as shown in Figure 6.4) or ice cover, leading to a reduction of electrical activity of the brain and anesthesia [18]. Although there is no evidence that hydrates or ice cover exist in a physiological condition, the interfacial water could still play an important role in modulating the interaction between anesthetics and their biological targets [17]. In this work, I provide direct experimental evidence that interfacial water in the proximity of proteins is essential for the molecular interaction between anesthetics and proteins.

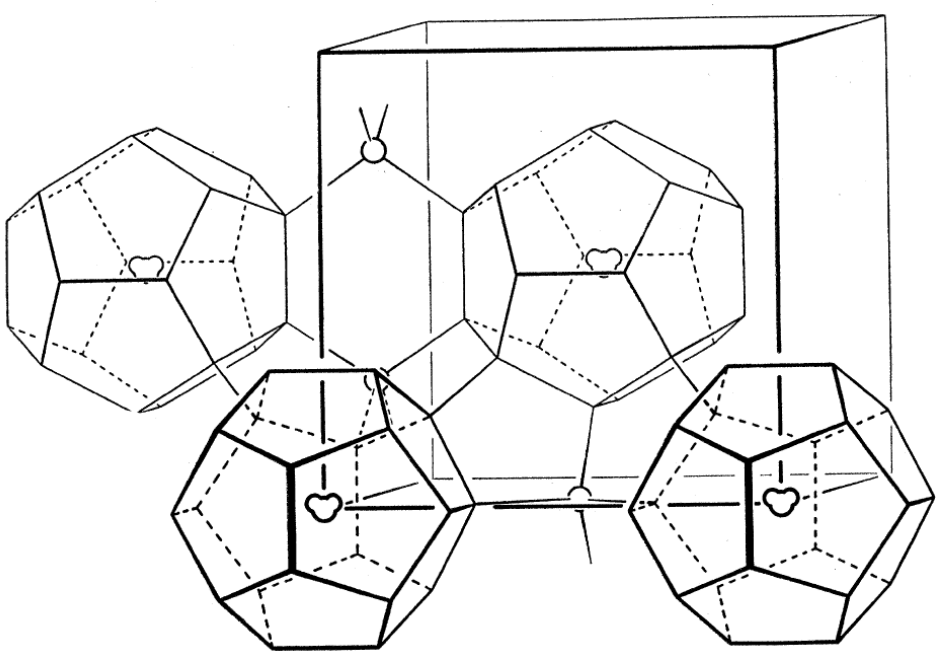

Figure 6.4 The structure of the hydrate crystals of small molecules, such as xenon.

The direct way to test the role of interfacial water in general anesthesia is to compare the anesthetic-protein interaction at a relative low protein hydration levels. The aqueous environment severely obscured the role of interfacial water in the anesthetic-protein interaction. Different from these experiments in protein and anesthetic solutions, the current

work requires that the hydration water is in direct proximity to the protein surface, the protein remains in the solid state, and the anesthetic is in the gas/vapor phase. A typical low hydration level for protein is 0.2 g water/g protein (h=0.2). Higher hydration levels contain excess amount of bulk water and obscure the role of interfacial water. ^{1}H NMR has been used to monitor the protein hydration level *in situ* [20]. The interaction between gaseous anesthetics and solid proteins is identical to that in solutions at the molecular level. The only difference is the influence of interfacial water that I am interested in.

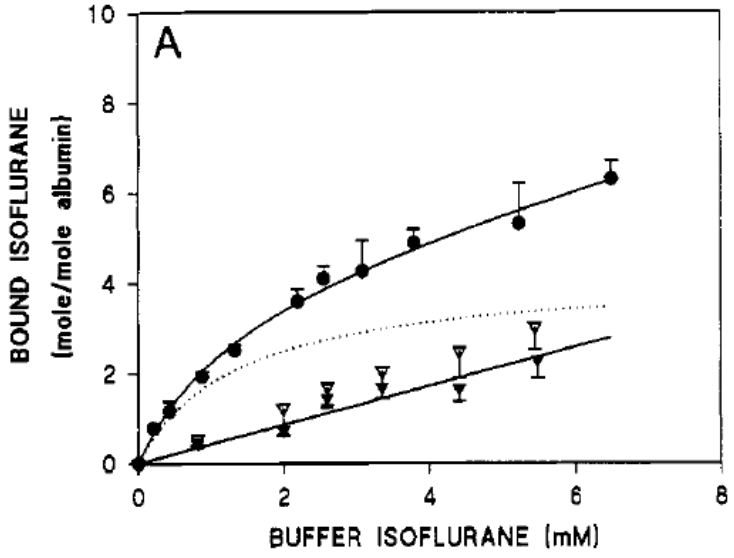

Figure 6.5 Gas chromatographic partition analysis of isoflurane equilibrium binding to BSA at 22°C, pH 7.2, and a concentration of 28 mg/mL.

Another goal of this work is to explore the nature of protein-anesthetic interaction using adsorption isotherms measured by NMR [20, 21]. ^{19}F NMR is a powerful tool for the study of anesthesia because ^{19}F is abundant in most of modern anesthetics while absent in natural biomolecules. Earlier ^{19}F NMR studies on anesthesia used anesthetics and proteins in solution form [22]. The fast exchange between anesthetic phases leads to only a resonance

line in the spectra [23]. The identification of bound anesthetics relies on the two-phase fast-exchange model of the spin-spin relaxation mechanism. This method has a very low sensitivity and lacks the ability to identify the direct NMR signature of bound anesthetics. It is also unable to measure the adsorption isotherm of anesthetics on proteins as a function of concentration. For instance, the amount of isoflurane bound to BSA is determined indirectly through the gas chromatographic partition analysis as shown in Figure 6.5. Bound isoflurane was calculated by subtracting aqueous concentrations, as measured using buffer samples, from total solution isoflurane concentrations. The dashed line is similar to a Langmuir type of adsorption isotherm. This method again is an indirect measurement of amount of bound anesthetics.

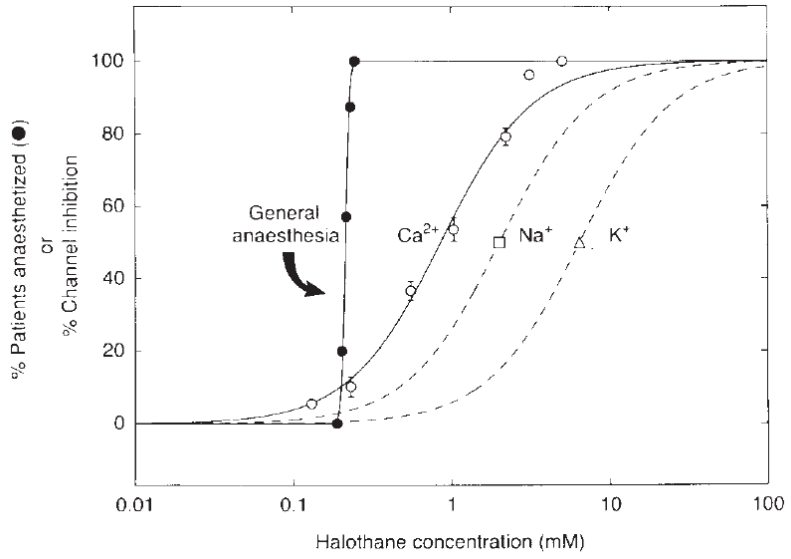

Figure 6.6 Most voltage-gated ion channels are relatively insensitive to general anesthetics. general anesthesia in humans (●), as measured by the lack of a purposeful response to a surgical incision, occurs at concentrations of halothane 4 to 30 times lower than the EC_{50} concentrations needed to half-inhibit peak currents through L-type Ca^{2+} channels (○) from clonal pituitary cells, Na^+ channels (□) from the squid giant axon, or delayed rectifier K^+ channels (Δ) from the squid giant axon [5].

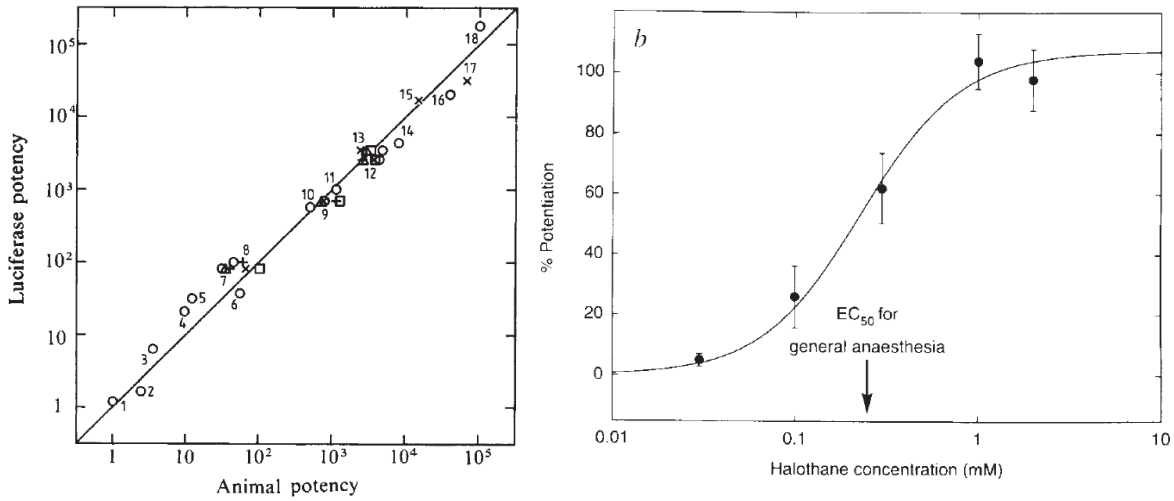

Figure 6.7 (a) Identity of general anesthetic concentrations needed to anesthetize whole animals and to inhibit luciferase activity by 50%, for a diverse range of simple anesthetics over a 100,000-fold range of potencies. The line is the line of identity [24]. (b) Clinically relevant concentrations of halothane potentiate responses to low levels of GABA (3 μM) in dissociated rat brain neurons, with 50% potentiation occurring at 0.23 mM halothane, close to the EC_{50} for general anesthesia (arrow) [5].

It is essential to determine the amount of bound anesthetics on proteins at a certain concentration precisely as required by isotherms measurement. A common signature in the curve representing the fraction of patients anesthetized versus the concentration of anesthetics, as shown in Figure 6.6, is the existence of a steep increase within a very narrow range of anesthetic concentration. The molecular mechanism of such steep increase has not been explained. The major criterion for identifying the anesthetic target is that the target functionality is inhibited at an anesthetic concentration similar to the concentration needed for general anesthesia in clinics as shown in Figure 6.7. The criterion itself suggests the lack of physical understanding of the nature of anesthetic-protein interaction.

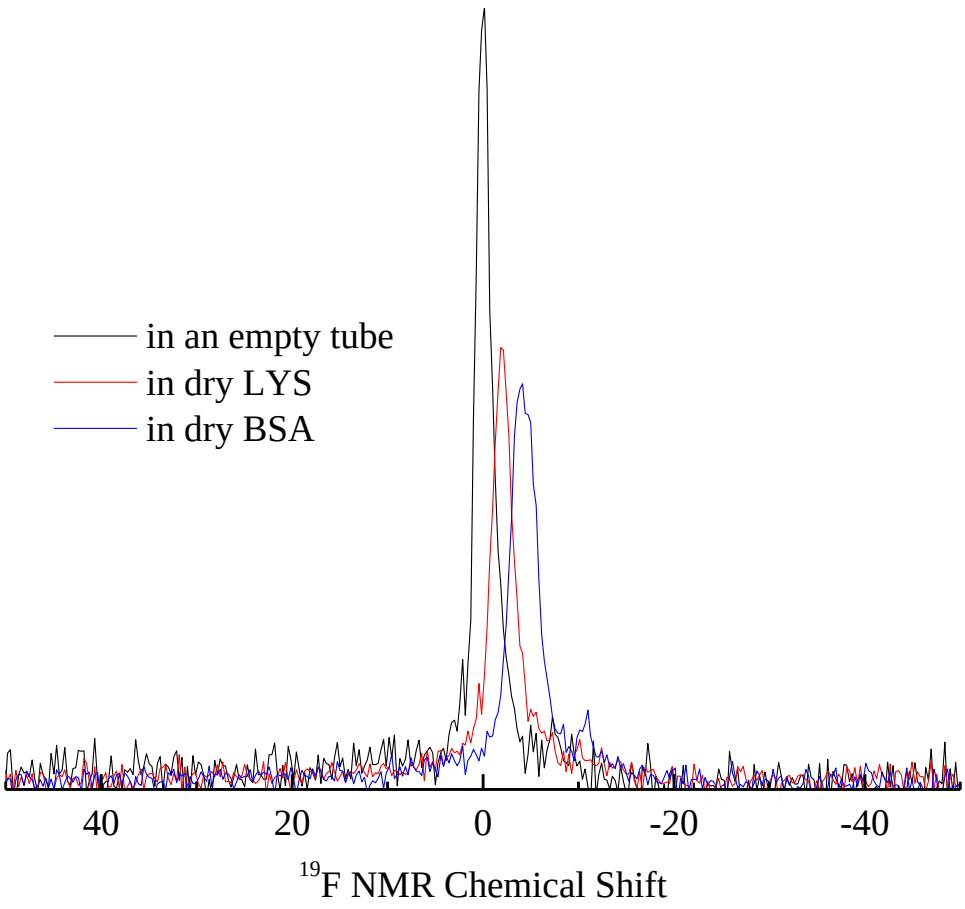

Figure 6.8 ^{19}F NMR spectra of halothane in an empty NMR tube, in dry lysozyme and BSA.

6.2 Experiments

Halothane (2-bromo-2-chloro-1,1,1-triflurorehtane, catalog no. B4388, ≥99%), hen egg white lysozyme (catalog no. L-7561, 3× crystallized, dialyzed, and lyophilized), and bovine serum albumin (catalog no. A9418, lyophilized powder, >96%), were purchased from Sigma Aldrich and used without further purification. The proteins were loaded into the quartz NMR sample tube connected to an *in situ* water and halothane loading system with controlled vapor pressure and temperature [21]. A single pulse (3~4 μs) was used to excite the ^{1}H and ^{19}F NMR signals at 7 T (300 MHz ^{1}H and 285 MHz ^{19}F NMR frequency) to monitor the amount of water and halothane, respectively. The protein was dynamically pumped for more

than 12 hours to remove the hydration water contained in the as-received sample. The dry protein was then exposed to a certain vapor pressure of halothane at a constant temperature for adsorption study. For the adsorption in wet protein, the protein was first exposed to water vapor to reach a hydration level of h~0.2 g water/g protein, before exposing it to halothane vapor.

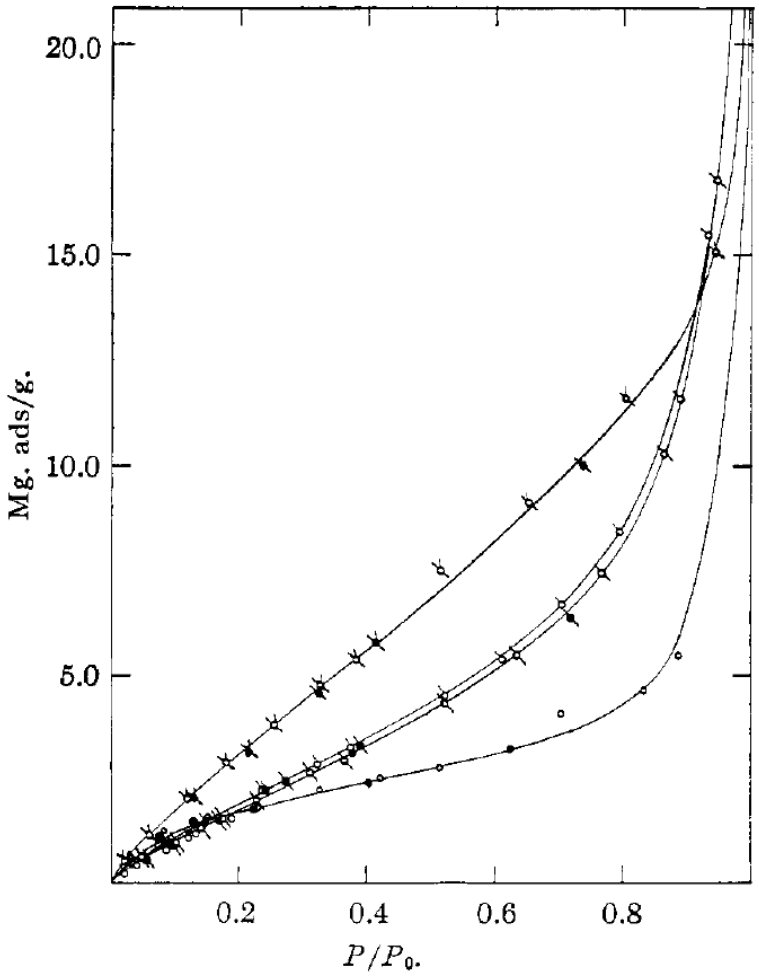

Figure 6.9 Adsorption isotherms of methane (117.2 K), n-butane (0.0°C), neopentane (10.0°C) and SF_6 (-64°C) in egg albumin (2% spray frozen) shown in order of low to high curve [25].

6.3 Results and discussion

Figure 6.8 shows ^{19}F NMR spectra of halothane in dry lysozyme and BSA, and in an empty NMR tube. The FWHM of the halothane spectra is as narrow as ~3 ppm, close to the resolution limit as observed from the spectrum of free halothane vapor in an empty NMR tube. This suggests that halothane behaves like free gas and doesn't bind to dry proteins.

It has been suggested that there might be a certain degree of rearrangement of protein side chains to compensate the large surface energy created by removing the hydration water of proteins [26]. This side chain rearrangement is unlikely to block the diffusion pathway of gas molecules within the matrix of protein powders. As shown in Figure 6.9, neopentane has enough accessibility to the molecular surface of dry proteins. This confirms that halothane, with smaller size than that of neopentane, is able to reach the molecular surface of BSA.

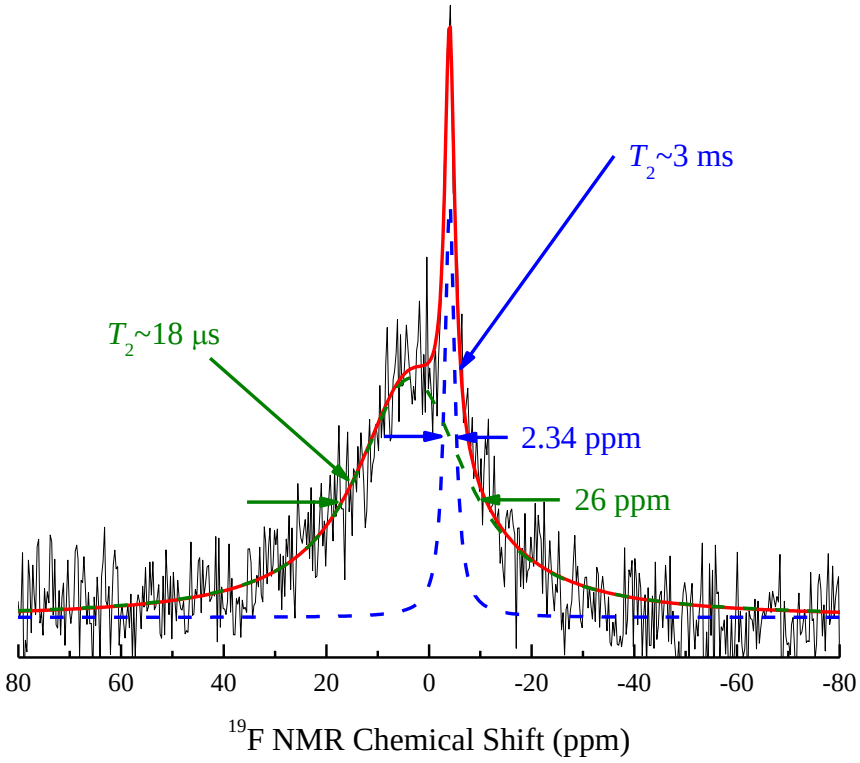

Figure 6.10 ^{19}F NMR spectra of halothane in wet lysozyme.

Figure 6.10 and Figure 6.11 show the ^{19}F NMR spectra of halothane in wet lysozyme and wet BSA, respectively. Both of the spectra show a signature of two peaks. The narrow peak corresponds to the free halothane in the empty space of the NMR tube that is in-between the lysozyme or BSA protein granules. The broad peak with a width of ~25 ppm corresponds to the strongly-adsorbed and motion-immobilized halothane molecules on wet proteins. This is the first model-free and direct evidence of halothane adsorbed on wet proteins. The separation of free and adsorbed halothane is directly shown in the spectra. The difference of adsorption in dry and wet proteins demonstrates the important role of interfacial water in the interaction of anesthetics and proteins.

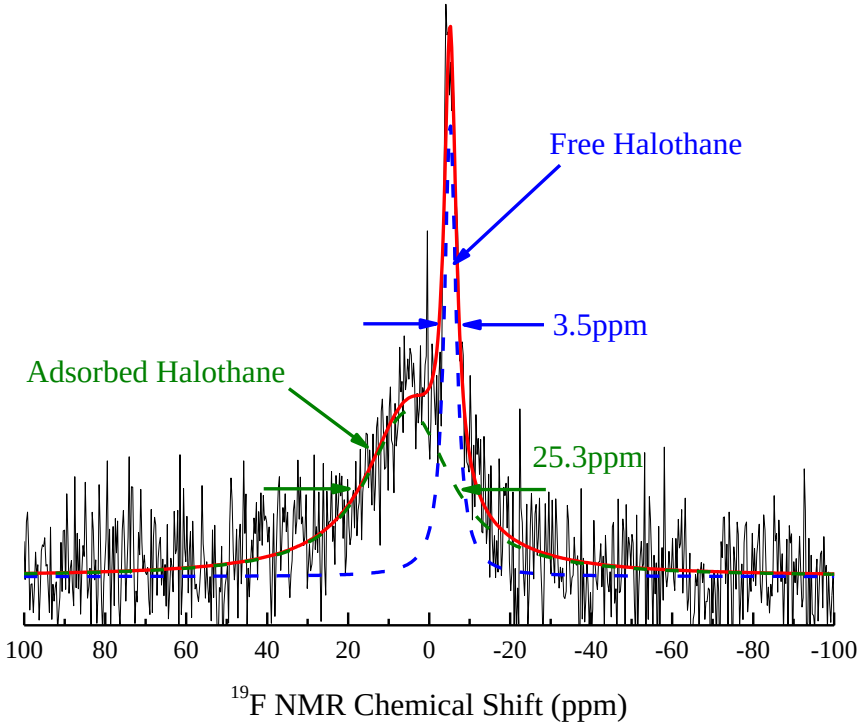

Figure 6.11 ^{19}F NMR spectra of halothane in wet BSA.

6.4 Conclusion

In this chapter, I provide preliminary results on the role of interfacial water in mediating the anesthetic-protein interaction. I identified direct ^{19}F NMR signatures of adsorbed halothane in wet proteins, including lysozyme and BSA, from spectra. This method does not depend on the model-dependent interpretation of spin-spin relaxation that was used in solution. The high sensitivity and accuracy of this method allow us to determine the halothane binding to small proteins such as lysozyme, which was not observed before. The direct separation of free and adsorbed halothane in spectra allows us to measure the adsorption isotherm with precise measurements of halothane vapor pressure and its amount within the NMR coil through ^{19}F NMR signal intensity.

6.5 References

[1] W. Kauzmann, Adv. Protein. Chem. **14**, 1 (1959).

[2] H. Meyer, Naunyn-Schmiedeberg's Arch. Pharmacol. **42**, 109 (1899).

[3] C. E. Overton, *Studien uber Narkose* (Fisher, Jena, 1901).

[4] N. P. Franks, and W. R. Lieb, Nature **300**, 487 (1982).

[5] N. P. Franks, and W. R. Lieb, Nature **367**, 607 (1994).

[6] N. P. Franks, and W. R. Lieb, Anesthesiology **101**, 235 (2004).

[7] R. D. Miller, *Miller's anesthesia* (Churchill Livingstone/Elsevier, Philadelphia, PA, 2010).

[8] N. P. Franks, Nat. Rev. Neurosci. **9**, 370 (2008).

[9] R. G. Eckenhoff, and J. S. Johansson, Pharmacol. Rev. **49**, 343 (1997).

[10] B. Harris, E. Moody, and P. Skolnick, Eur. J. Pharmacol. **217**, 215 (1992).

[11] P. R. Andrews, and L. C. Mark, Anesthesiology **57**, 314 (1982).

[12] J. A. Richter, and J. R. Holtman, Prog. Neurobiol. **18**, 275 (1982).

[13] S. Ryder, W. L. Way, and A. J. Trevor, Eur. J. Pharmacol. **49**, 15 (1978).

[14] J. S. Chiou *et al.*, Science **248**, 583 (1990).

[15] D. D. Koblin *et al.*, Anesth. Analg. **79**, 1043 (1994).

[16] Y. Xu, and P. Tang, Biochim. Biophys. Acta-Biomembr. **1323**, 154 (1997).

[17] D. Willenbring, Y. Xu, and P. Tang, Phys. Chem. Chem. Phys. **12**, 10263 (2010).

[18] L. Pauling, Science **134**, 15 (1961).

[19] S. L. Miller, Proc. Natl. Acad. Sci. USA **47**, 1515 (1961).

[20] H. J. Wang *et al.*, Phys. Rev. E **83**, 031924 (2011).

[21] H. J. Wang *et al.*, Science **322**, 80 (2008).

[22] Y. Xu *et al.*, Biophys. J. **70**, 532 (1996).

[23] B. W. Dubois, and A. S. Evers, Biochemistry **31**, 7069 (1992).

[24] N. P. Franks, and W. R. Lieb, Nature **310**, 599 (1984).

[25] S. W. Benson, and D. A. Ellis, J. Am. Chem. Soc. **72**, 2095 (1950).

[26] I. D. Kuntz, and W. Kauzmann, Adv. Protein. Chem. **28**, 239 (1974).

CHAPTER 7

CONCLUSION

This dissertation discussed several studies on the nanoconfined and interfacial water using NMR. Water exhibits dramatically different behaviors in different circumstances as a result of its intrinsic properties and local environment. In the tubular structure at the nanometer scale in SWNTs, the hydrophobicity should not be considered as an absolute property of a surface without considering the structure of interfacial water. The correlation time of water reorientation is reduced to be on the order of 10 to 100 ns compared to ~3 ps of bulk water. Confined and interfacial water are prevalent in biological systems, such as the water in ion channels and in the proximity to proteins. The affinity change due to the temperature-induced structural change of water could be relevant to various phenomena including in biological systems. On the other hand, in the wettable nanoscopic pores of microporous activated carbons, water show properties that are similar to those of water in its bulk phase, including molecular reorientation and capillary condensation. The dynamics of water changes dramatically upon capillary condensation and reach a value that is close to that of bulk water. The capillary condensation occurs at a vapor pressure that can be estimated by the Kelvin equation. This result suggests that water starts to exhibit bulk properties with thickness as thin as three molecular layers in size of 1.2 nm. Therefore, water adsorption measurement could be effectively used as a tool for characterizing pore size distribution on the nanometer scale.

Water at the interface of biomolecules has a much broader and direct impact on our understanding of biology. I observe a strong temperature dependence of the water uptake in lysozyme at high relative pressure below 10°C. Such a temperature dependence could be explained by the enhanced cost in the elastic energy for accommodating the hydration water at lower temperature. The temperature dependence of the elastic modulus *K* of the protein is responsible for the observed temperature dependence of the upswing in water uptake. Although related to the microscopic flexibility of the protein, the elastic modulus *K* used in our analysis of the elastic energy is a parameter at the level of thermodynamics, not a model-dependent quantity at the molecular level or based on statistical mechanics. The elastic modulus *K* derived from water isotherms is consistent with the values of Young's modulus measured directly by mechanical measurement. This provides an independent validation of the solution picture. The interplay of elastic modulus and water absorption has an important role in determining the fluctuations of proteins and may be important for the functions of proteins such as enzymatic activities.

A similar temperature dependence of the sorption isotherm was also observed in hemoglobin. NMR relaxation in hemoglobin shows a cross relaxation between fast-relaxing water and slow-relaxing proteins due to their different spin diffusion mechanisms. The spin-lattice relaxation can be used to estimate the diffusion constant of protons towards the paramagnetic center, which is several orders of magnitude slower than that in pure water.

We also provide preliminary results on the role of interfacial water in mediating the anesthetic-protein interaction. We identified direct ^{19}F NMR signatures of adsorbed halothane in wet proteins, including lysozyme and BSA, from NMR spectra. This method does not depend on the model-dependent interpretation of spin-spin relaxation that was used

in solution. The high sensitivity and accuracy of this method allow us to determine the halothane binding to small proteins such as lysozyme, which was not observed before. With a precise control of hydration level, we are able to provide evidence that the halothane binds to proteins only with the presence of interfacial water.